# Evolution of and deposition from an evaporating sessile thin annular droplet

Laura M. Mills

Department of Mathematics and Statistics

University of Strathclyde

Glasgow, UK

December 2022

# Acknowledgements

I am deeply indebted to my family and friends for their incredible support: my parents for always being there; my brother, Paul, for always being 5 minutes late; and my best friend, Shelley, without whom the past decade (and a half) would have contained no joy whatsoever. Thank you for everything.

Finally, to Agnes, Bill, and Marie; the most courageous and kind-hearted people I will ever have the pleasure of knowing. The world is a darker place without you in it. Love you always, and miss you endlessly.

# Abstract

The evaporation of a spherical-cap shaped sessile droplet has been extensively studied. However, there is a growing interest in the evaporation of sessile droplets with more complicated geometries, such as an annular droplet. Not only is the evaporation of annular droplets of intrinsic scientific interest in its own right, but it also arises in several practical and industrial contexts, such as the evaporation of a droplet in a well, which occurs in the manufacturing of organic light-emitting diode (OLED) displays, and in the context of a droplet evaporating on a patterned substrate. In the present work, we formulate and analyse a mathematical model for the evaporation of a thin, axisymmetric annular droplet with two circular contact lines. A numerical solution for the concentration of vapour in the atmosphere is discussed, as well as numerical, asymptotic and approximate solutions for the local and total evaporative flux in the diffusion-limited regime. The evolution, and therefore the lifetime, of the droplet in various modes of evaporation, as well as the nature of the deposit left behind on the substrate after the droplet has entirely evaporated, are described both for a spatially-uniform and a diffusion-limited evaporative flux.

# Contents

# Chapter 1

# Introduction

## 1.1 Evaporation of sessile droplets

The evaporation of a sessile droplet (i.e. a droplet lying on a substrate) has been extensively studied (see, for example, the review articles by Routh [67], Larson [44], Giorgiutti-Dauphiné & Pauchard [35], Lohse [48], and Wilson & D'Ambrosio [79]). When a sessile droplet evaporates vapour escapes from the free surface of the droplet and into the surrounding atmosphere. The evaporation of a sessile droplet is a fundamental problem which occurs in a wide variety of natural and industrial contexts such as the spraying of plants with pesticides [86], blood stain pattern analysis [7], spray cooling [50], and ink-jet printing [77]. Some examples of sessile droplets are shown in Figure 1.1.

Various theoretical models have been proposed for the evaporation of a sessile droplet, however the model that is the most widely studied (and is perhaps the most widely applicable) is the diffusion-limited model. The diffusion-limited model describes the situation in which the limiting factor in the evaporation process is the
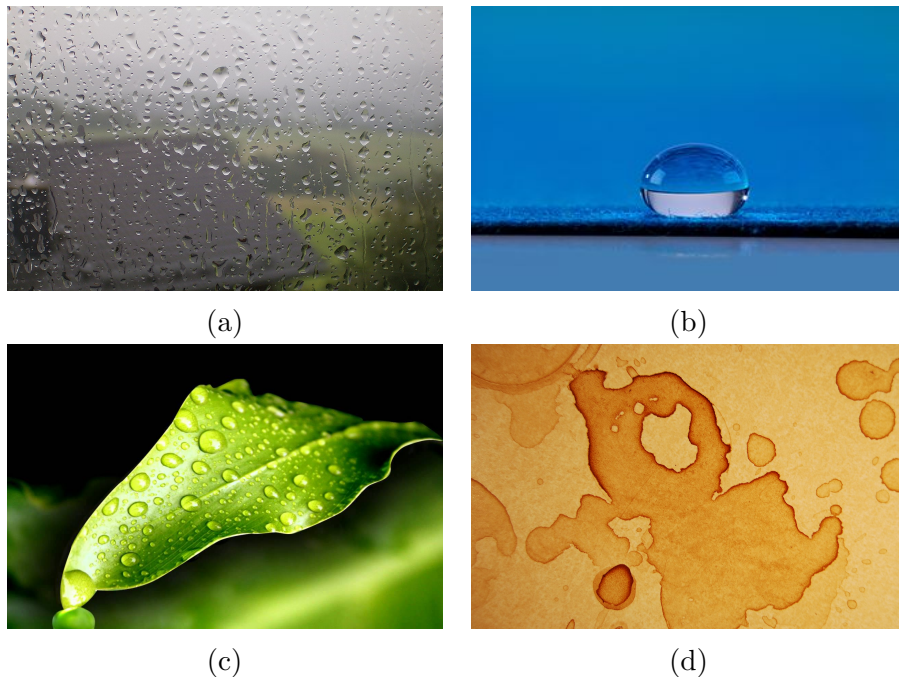
Figure 1.1: Examples of sessile droplets: (a) water droplets on a window [33], (b) a droplet on a hydrophobic substrate [39], (c) droplets on a leaf [1], and (d) coffee stains resulting from an evaporating coffee spill [37].

diffusion of vapour away from the surface of the droplet and into the atmosphere (see, for example, the recent review article by Wilson & D'Ambrosio [79]). An underlying assumption in the diffusion-limited model is that the diffusion of vapour is quasi-static, meaning that the timescale for the diffusion of vapour is much shorter than the lifetime of the droplet (i.e. the time it takes for the droplet to evaporate fully). Under this assumption, the concentration of vapour in the atmosphere, denoted by $\hat{c}$, satisfies Laplace's equation

$$\nabla^2 \hat{c} = 0, \tag{1.1}$$

alongside boundary conditions describing the behaviour of the concentration of vapour on the surface of the droplet, in the far-field, and on the substrate. Throughout, hats will denote dimensional variables.

Figure 1.2 shows a sketch of a spherical-cap shaped droplet. In particular, it
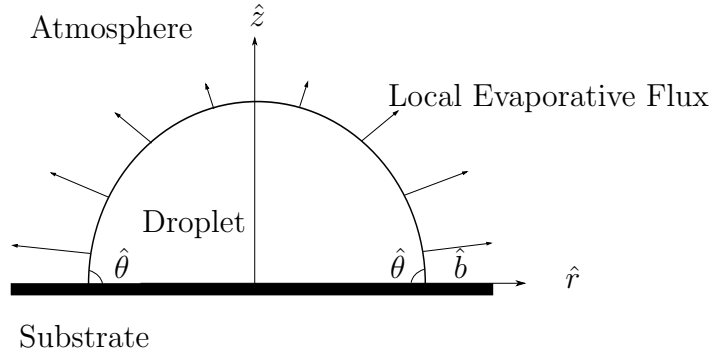
Figure 1.2: Sketch of a spherical-cap droplet

shows the contact angle, i.e. the angle that the droplet makes with the substrate, denoted by $\hat{\theta}$, the radius of the contact line of the droplet at $\hat{r} = \hat{b}$, and the profile of the droplet $\hat{z} = \hat{h}$.

The simplest case of the diffusion-limited model involves a spherical-cap shaped droplet, which was first studied by Picknett & Bexon [62]. Assuming that the droplet has a spherical-cap shape simplifies the problem by ensuring that the problem for $\hat{c}$ is axisymmetric (around the central axis of the droplet) and has a known domain.

Figure 1.2 shows a sketch of a spherical-cap shaped droplet. In particular, it shows the contact angle, i.e. the angle that the droplet makes with the substrate, denoted by $\hat{\theta}$, the radius of the contact line of the droplet at $\hat{r} = \hat{b}$, and the profile of the droplet on $\hat{z} = \hat{h}$.

In practice, spherical-cap shaped droplets occur for small values of the Bond and capillary numbers. The Bond number, $Bo$, characterises the ratio of the magnitude of the force of gravity and the surface tension forces acting on the droplet, and ensures that gravity does not play a role in the profile of the droplet. The capillary number, $Ca$, characterises the ratio of the magnitude of viscous and surface tension forces acting at the free surface of the droplet, and ensures that the shape of the droplet is determined by surface tension. Picknett & Bexon [62] utilised a series

solution for the evolution of the droplet to obtain an approximate expression for the lifetime an evaporating droplet. When their approximate expression was compared to the results of their own experiments Picknett & Bexon [62] found errors ranging from 0.8% to 19.7%. They did, however, note that the droplets in some of the experiments were not a perfect spherical-cap shape due to the Bond number being too large to ensure that gravity did not play a role in the droplets' shapes.

Lebedev [45] first gave the exact solution to the concentration of vapour in the atmosphere, in the context of a mathematically equivalent problem in electrostatics. Deegan *et al.* [26, 27] then used the exact solution for $\hat{c}$ from Lebedev [45] to derive analytical expressions for the local and total evaporative fluxes, denoted by $\hat{J}$ and $\hat{F}$ respectively.

The case of a thin droplet for which the contact angle is small (i.e. when $\hat{\theta} \ll 1$) is of particular interest, since more analytical progress can be made in this case (see, for example, Hu & Larson [38], Dunn *et al.* [29, 28], and Wilson & Duffy [80]). Taking $\hat{D}$ to be the diffusion coefficient, $\hat{c}_{\text{sat}}$ to be the constant saturation concentration of vapour in the atmosphere, $\hat{c}_{\infty}$ to be the constant far-field concentration, and $\hat{b}_0$ it be the initial radius of the droplet, $\hat{J}$ can be nondimensionalised according to $\hat{D}(\hat{c}_{\text{sat}} - \hat{c}_{\infty})/\hat{b}_0$. The non-dimensional expression for $J$ for a thin droplet is given by

$$J = \frac{2}{\pi\sqrt{b^2 - r^2}} \quad \text{for} \quad 0 \le r \le b, \tag{1.2}$$

which has an (integrable) square root singularity at the contact line $r = b$. A local analysis near the contact line (see, for example, Jackson [40]) shows that

$$J \propto (b - r)^{\lambda - 1}, \tag{1.3}$$

where $\lambda$ ($> 1/2$) is a function of the contact angle of the droplet $\theta$,

$$\lambda = \frac{\pi}{2(\pi - \theta)}. \tag{1.4}$$

In the limit of a thin droplet (i.e. in the limit $\theta \to 0$) then $\lambda \to 1/2$, recovering the square root singularity at the contact line seen in (1.2).

If $\hat{F}$ is nondimensionalised according to $\hat{b}_0 \hat{D}(\hat{c}_{\text{sat}} - \hat{c}_\infty)$, the non-dimensional expression for $\hat{F}$ for a thin droplet is given by

$$F = 2\pi \int_0^b Jr \, \mathrm{d}r = 4b. \tag{1.5}$$

Hu & Larson [38] used the Finite Element Method (FEM) to numerically solve Laplace's equation (1.1) subject to the associated boundary conditions for the concentration of vapour, for a droplet with a contact angle within $0 < \hat{\theta} \leq \pi/2$ and hence determined the local and total evaporative fluxes. Their numerical solution for the lifetime of the droplet was in good agreement with the approximate theoretical solution of Picknett & Bexon [62], with a maximum relative error of 1.3% when considering the same range of contact angles. Their approximate solution for $\hat{J}$ was in very good agreement with the exact solution from Lebedev [45] with a maximum relative error of 1.5%.

Dunn *et al.* [29, 28] provided further theoretical analysis of the diffusion-limited evaporation of a spherical-cap droplet with a pinned contact line, generalising the work of Deegan *et al.* [26, 27] to include the effects of evaporative cooling. Evaporative cooling describes the effect in which latent heat of vaporisation (the energy that is required for phase change) is obtained from the droplet and its surroundings. They found that the total evaporative flux $\hat{F}$ depends on the thermal conductiv-

ity of the substrate. Their results were found to be in good agreement with the experimental results of David *et al.* [24].

There has been substantial subsequent work on the diffusion-limited model, expanding on topics such as: the effects of heat loss (Ait Saada *et al.* [3]), evolution and lifetime (Murisic and Kondic [59] and Armstrong *et al.* [5]), the shielding effect (Schofield *et al.* [68] and Wray *et al.* [81, 84]), droplet geometry (Sáenz *et al.* [75], D'Ambrosio *et al.* [22] and Wray & Moore [82]), the effects of various substrate properties (Stauber *et al.* [74] and Armstrong *et al.* [6]), and deposition patterns (Siregar *et al.* [72], Sefiane [70], Pradhan & Panigrahi [66], Moore *et al.* [57, 58]).

A spatially-uniform evaporative flux is sometimes used as a simple approximation to the spatially non-uniform evaporative flux (1.2) predicted by the diffusion-limited model (see, for example, Okuzono *et al.* [61]). There are also some physical situations in which the local evaporative flux $\hat{J}$ is approximately spatially uniform. For example, a spatially-uniform evaporative flux has also been observed experimentally in cases in which a droplet evaporates on a hydrogel (see, for example, Boulogne [12]). Moreover, note that in the special case of a hemispherical droplet with contact angle $\hat{\theta} = \pi/2$, the diffusion limited flux $\hat{J}$ is spatially uniform and proportional to $1/\hat{b}$ (see, for example, Stauber *et al.* [74]).

## 1.2 Modes of evaporation and the evolution of evaporating droplets

The manner in which a droplet evaporates has a considerable effect on its lifetime. There has been a great amount of research into the evolution, and hence the lifetime, of droplets in various modes of evaporation, which describe the dynamics of the

contact line and contact angles during the evaporation (see, for example, Stauber *et al.* [74], Armstrong *et al.* [5, 6], and Schofield *et al.* [68]).

In the special case of a thin droplet, time is non-dimensionalised according to $\hat{\rho}\hat{b}_0^2\hat{\theta}_0/(\hat{D}(\hat{c}_{\text{sat}} - \hat{c}_\infty))$, where $\hat{\rho}$ is the constant density of fluid in the droplet, and $\hat{\theta}_0$ is the initial contact angle of the droplet. The "extreme" modes of evaporation, identified by Picknett & Bexon [62], are the Constant Contact Radius (CR) mode and the Constant Contact Angle (CA) mode. In the CR mode, shown in Figure 1.3(a), the contact line remains pinned (i.e. $\hat{b} = \hat{b}_0$ throughout the evaporation), and the contact angle decreases from the initial contact angle $\hat{\theta} = \hat{\theta}_0$ to $\hat{\theta} = 0$. In this mode, the non-dimensional lifetime of the droplet is $\pi/16$ (see, for example, Stauber *et al.* [74]). In the CA mode, shown in Figure 1.3 (b), the contact angle of the droplet remains fixed throughout the evaporation and the radius of the contact line decreases from the initial radius $\hat{r} = \hat{b}_0$ to $\hat{r} = 0$. In this mode, the non-dimensional lifetime of the droplet is $3\pi/32$ (see, for example, Stauber *et al.* [74]). A great deal of research has focused on these extreme modes of evaporation, including Aboubakri *et al.* [2], Armstrong *et al.* [5, 6], Barmi & Meinhart [8], Birdi & Vu [11], Birdi *et al.* [10], Dash & Garimella [23], Erbil *et al.* [31, 32], McHale *et al.* [52, 53], Picknett & Bexon [62], Pittoni *et al.* [63], Shanahan *et al.* [71], Sobac & Brutin [73], Stauber *et al.* [74], and Wray *et al.* [81].

In practice, however, when a droplet evaporates, it will often do so in a "mixed mode". Experimental studies of droplet evaporation (including Picknett & Bexon [62], Hu & Larson [38], McHale *et al.* [53], Bhardwaj *et al.* [9], Dash & Garimella [23], and Vlasko-Vlasov [76]) report that a droplet that initially evaporates in a CR phase will typically have a critical contact angle, denoted by $\hat{\theta}^*$, at which the contact line becomes unpinned and thereafter the droplet evaporates in a CA phase. This particular mixed mode of evaporation is known as the stick-slide (SS) (or, more

(a)                                          (b)
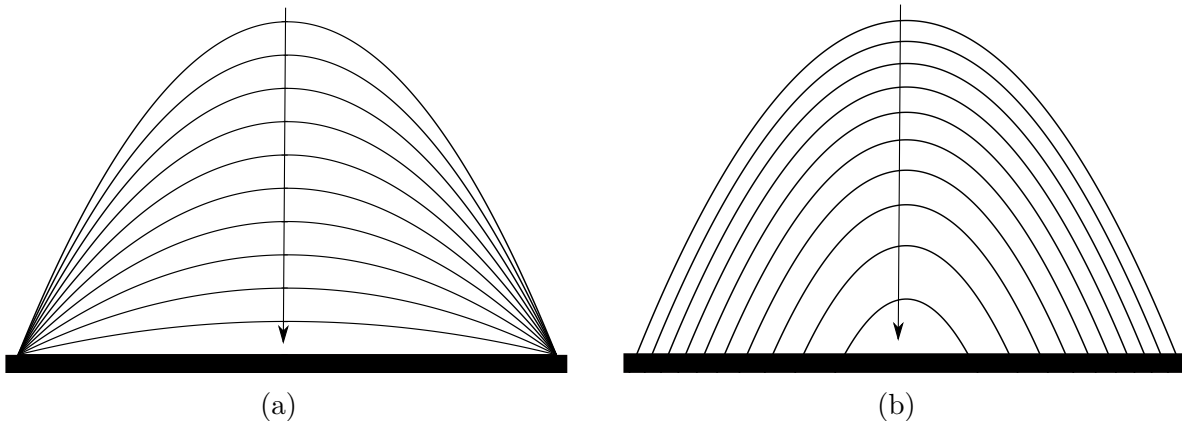
Figure 1.3: Sketches of the evolution of a droplet evaporating in (a) Constant Contact Angle (CA) mode and (b) Contant Contact Radius (CR) mode. The arrows represent the direction of increasing time.

loosely, as the stick-slip) mode (see, for example, Stauber *et al.* [74]).

The lifetime of a thin droplet evaporating in the SS mode is constrained by the lifetimes of an initially identical droplet evaporating in the CA and CR modes, and depends on the critical contact angle of the droplet. More generally, however, for a droplet evaporating with an initial contact angle satisfying $\pi/2 < \hat{\theta}_0 < \pi$, the lifetime of the droplet can be longer than that of an initially identical droplet evaporating in either the CA or the CR mode and depends on the critical contact angle and the initial contact angle, as described by Stauber *et al.* [74].

Other mixed modes such as the stick–jump (SJ) mode can also occur in practice. The stick–jump is the name of the mode of evaporation in which the droplet has several "stick" phases in which the droplet evaporates in a CR mode, separated by several short "jump" phases in which the radius of the contact line rapidly jumps to a new (smaller) value.
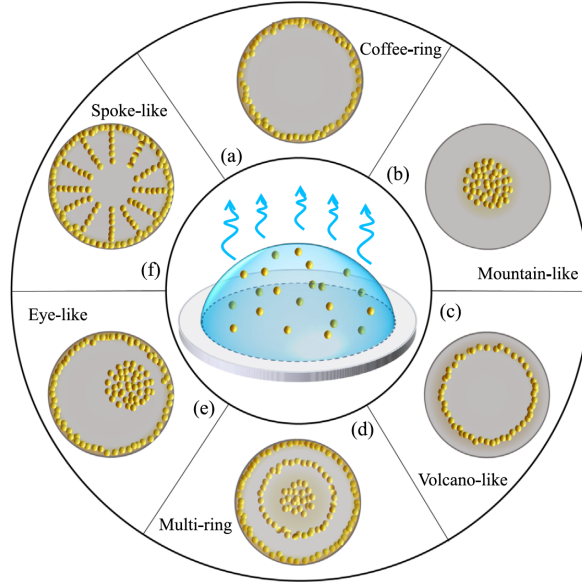
Figure 1.4: Examples of various possible deposition patterns, reproduced from Yang *et al.* [85].

## 1.3 The deposition patterns resulting from the evaporation of particle-laden droplets

The evaporation process induces a flow within the droplet which, when the droplet contains suspended particles, leaves behind a deposition pattern on the substrate after the droplet has fully evaporated. These deposition patterns are of significant interest (see, for example, Deegan [25], Deegan *et al.* [26, 27], Popov [65], Wray *et al.* [83], Boulogne *et al.* [12], and Moore *et al.* [57, 58]) with the widely studied "coffee-ring" being the most well-known deposition pattern, though there are many different possible deposition patterns that can occur (see, for example, the review by Wilson & D'Ambrosio [79]). Figure 1.4 shows examples of the various deposition patterns that can be observed.

Yang *et al.* [85] described some of the various possible deposition patterns that can be observed such as: a "coffee-ring" formed at the contact line of the droplet;

multi-ring deposits, where multiple coffee-rings are formed on the substrate; and a mountain-like pattern, where all of the deposit gathers near the centre of the droplet.

Popov [65] analytically and numerically studied the evaporation of a particle-laden droplet. In particular, he derived expressions for the concentration of suspended particles in bulk of the droplet, and described the coffee-ring left behind after the droplet had fully evaporated. In his work, he assumed that presence of the suspended particles within the droplet did not affect the local evaporative flux $\hat{J}$, and that the suspended particles were advected by the flow within the droplet. Popov found there was a good agreement between his results and the experimental results of Deegan *et al.* [27].

Boulogne *et al.* [12] theoretically and experimentally studied the deposition patterns left behind after a particle-laden droplet had evaporated with either a spatially-uniform flux and diffusion-limited evaporative flux. They found that, while the timescale of evaporation varied between the two cases, both fluxes produced a deposit at the contact line of the droplet

## 1.4 The effect of droplet geometry on droplet lifetimes and deposition patterns

In recent years, the evaporation of one or more droplets with more complicated geometries than a spherical cap have been the subject of increasing interest, specifically in regards to the evaporation of droplets with a non-circular contact line and of multiple droplets.

Sáenz *et al.* [75] studied the evaporation of, and deposition patterns resulting from, droplets with non-circular contact lines, specifically triangular, square, and

kidney-shaped droplets. The study found that the local and total evaporative fluxes, and the density of the resulting deposition patterns, depend on the shape of the droplet. In particular, they found that there is a denser deposit at the contact line in regions in which the curvature of the contact line is the greatest.

Wray *et al.* [81] provided an analysis, based on previous work by Fabrikant [34], of the evaporation of an arbitrary arrangement of multiple thin droplets with circular contact lines. The theoretical analysis of Wray *et al.* [81] was shown to give predictions for the evolution of the shape of the droplets which are in good agreement with the experimental results of Khilifi *et al.* [42] for an array of seven droplets in an I-shaped configuration. These results illustrate that droplets within an array experience a "shielding" effect due to the presence of nearby droplets, causing them to experience a lower rate of evaporation, and hence a droplet in proximity to other droplets has a longer lifetime than it would do in isolation.

Wray *et al.* [84] built upon the work of Wray *et al.* [81] to study the deposition patterns from an arbitrary arrangement of thin, circular, particle-laden droplets. By solving the hydrodynamic problem within the droplets, they showed that the density of the deposits at the contact lines of the droplets is reduced in the regions of the contact lines that are closest to the other droplets. The theoretical predictions of Wray *et al.* [84] were found to be in good agreement with the experimental results of Pradhan & Panigrahi [66] for the density of the deposit at the contact lines of a pair of identical droplets in close proximity.

Masoud *et al.* [51] generalised the work of Wray *et al.* [81] to include droplets that are not thin, utilising Green's Second Identity and the Method of Reflections to obtain a general approximate solution for the total evaporative flux of a droplet within an array of evaporating droplets.
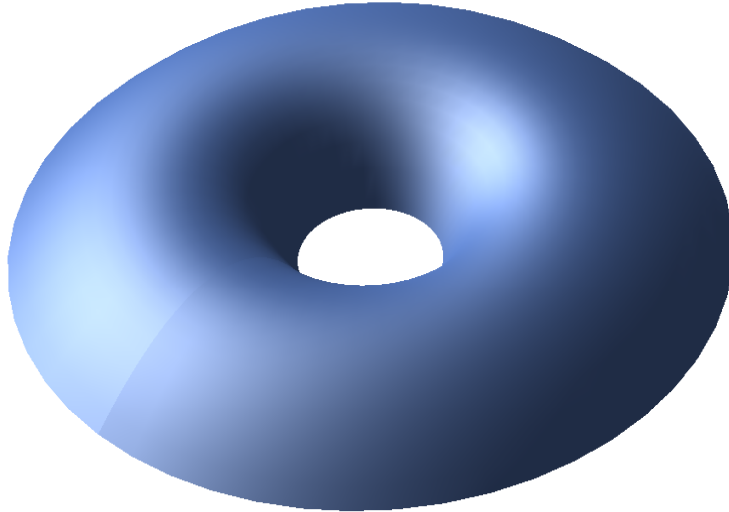
Figure 1.5: An annular droplet

## 1.5 Annular droplets

The present work is concerned with the evaporation of a sessile annular droplet (i.e. an axisymmetric droplet with two concentric circular contact lines, henceforth referred to as the inner and the outer contact lines) as shown in Figure 1.5. The radii of the inner and the outer contact lines are denoted by $\hat{a}$ and $\hat{b}(> \hat{a})$, respectively. Sessile annular droplets are found in real life scenarios such as: a result of applying a jet of air or rotating the substrate (McKinley *et al.* [54, 55, 56]), on patterned surfaces (Lenz *et al.* [46], Jokinen *et al.* [41], and Schäfle *et al.* [69]), in the presence of an electric fields (Edwards *et al.* [30]), as well as during the evaporation of a droplet in a cylindrical well (Vlasko-Vlasov *et al.* [76] and D'Ambrosio *et al.* [22]).

McKinley *et al.* [54, 55, 56] analysed the effects of an air-jet blowing down onto a thin droplet and of the rotation of a thin droplet, and found that an annular droplet can form for a sufficiently strong air flow or sufficiently rapid rotation. By conducting a linear stability analysis, they found that an annular droplet created

in these ways is unconditionally unstable for small perturbations of the inner and outer contact lines.

While the results of McKinley *et al.* [54, 55, 56] conclude that an annular droplet is not stable on a planar substrate, stable annular droplets have created experimentally on textured substrates. Specifically, an annular droplet can be created by depositing a droplet onto substrate that has been patterned with a lyophobic and lyophillic coating (or hydrophobic and hydrophillic if the droplet is specifically a droplet of water). Lenz *et al.* [46] studied the changes in the shape of an annular droplet on a patterned lyophobic and lyophilic substrate as the volume of the droplet was increased. Their theoretical and experimental results showed that a single, non-axisymmetric bulge in the droplet can form for sufficiently large volumes.

Jokinen *et al.* [41] also studied the changes in the shape of an annular droplet on a substrate patterned with a hydrophobic and hydrophilic coating as the volume was increased. They reported that annular droplets could: form a single, non-axisymmetric bulge on the annular droplet; collapse into a spherical-cap shaped droplet; or form a "lens" shape in which an air bubble is trapped within a spherical-cap shaped droplet. They gave the ranges of volume and aspect ratios that correspond to each of the three outcomes.

Schäfle *et al.* [69] experimentally created annular droplets on a substrate patterned with a lyophobic coating. Building upon the work of Lenz *et al.* [46] and Jokinen *et al.* [41], they studied the differences in the evaporation of annular droplets for various values of $k = \hat{a}/\hat{b}$ (where, by definition, $0 \leq k \leq 1$), i.e. for various values of the ratio of the radii of the two contact lines. They found that for values of $k$ close to unity, annular droplets collapse into a spherical-cap shaped droplet, while for sufficiently small values of $k$, they found that a single, non-axisymmetric bulge

forms.

Chen *et al.* [15] experimentally studied the deposition of various droplets with two contact lines (including an annular droplet) created using inkjet printing. While they observed irregular bulges in the droplets as a result of the inkjet printing process, their results showed that the particles are advected to both the inner and outer contact lines for all shapes of droplet they studied.

Edwards *et al.* [30] used non-uniform electric fields to create annular droplets. They found that these initial annular droplet broke up into a ring of droplets when the electric field is turned off. The number of resulting droplets depends on the volume of the initial droplet. They found that larger numbers of small droplets would form for lower volumes of the initial droplet.

More recently, Vlasko-Vlasov *et al.* [76] and D'Ambrosio *et al.* [22] studied the evaporation of a droplet in a well, during which the droplet can become annular with an inner contact line after the free surface makes contact with the bottom of the well (referred to as touchdown). Vlasko-Vlasov *et al.* [76] studied the evaporation of a droplet evaporating in a cylindrical well. They found that the inner contact line moves radially outwards after touchdown and undergoes a stick-slide motion during the evaporation, and examined the resulting deposition patterns. D'Ambrosio *et al.* [22] undertook a theoretical and experimental study of the evaporation of a thin droplet in a well. D'Ambrosio *et al.* [22] obtained a numerical solution for the concentration of vapour, and hence the local and total evaporative flux of the system, and calculated the evolution and hence the lifetime of the droplet. They determined the conditions for touchdown to occur (dependent on the shape of the well), and described the evolution before and after either depinning (for "shallow" wells) or touchdown (for "steep" wells). If touchdown occurred, the inner contact line moved

towards the outer wall of the well and the contact angle at the inner contact line is zero throughout the evaporation, while the outer contact line was pinned at the outer wall of the well and the outer contact angle varies throughout the subsequent evaporation.

## 1.6 Analogous problems to droplet evaporation

While there has not been any previous work on the evaporation of a sessile annular droplet, there has been work on problems that are mathematically equivalent to the corresponding evaporative problem. Specifically, the potential around an electrified disc and the force on an annular punch satisfy the same governing equations and boundary conditions as the concentration of vapour in the atmosphere.

Cooke [20], generalising the work of Noble [60], expressed the electrostatic problem as three coupled integral equations for equivalent of the concentration of vapour $\hat{c}$. Which he then reduced to a single integral equation that could be solved for the equivalent to the total evaporative flux $\hat{F}$ using Chebyshev-Gauss quadrature.

Collins [18] expressed the electrostatic problem in terms of a Fredholm equation. He then derived the asymptotic solution of the equivalent to $\hat{F}$ in the limit $k \to 0^+$.

Leppington & Levine [47] used Green's Theorem to obtain an integral equation that is accurate in the limit $k \to 1^-$ which could be solved for the first-order asymptotic solution for $\hat{J}$, and hence for $\hat{F}$, in that limit. However, as we shall describe in Chapter 4.3 of the present work, they made an error when calculating the leading order term in the solution for $\hat{J}$. However, their error is antisymmetric about the midpoint of the annulus, and so their asymptotic solution for $\hat{F}$ is still correct.

Clements & Love [17], using a similar method to Cooke [20] and Noble [60],

expressed $\hat{J}$ as a single integral equation. While both Noble [60] and Cooke [20] utilised Bessel functions to approximate the integral equations, Clements and Love used a Laurent series. As a result of this, Clements and Love's approximate solution is only accurate for values of $k$ satisfying $0 < k \leq 0.6$.

Gladwell & Gupta [36] obtained accurate approximate solutions for $\hat{J}$ and $\hat{F}$ in the limit $k \to 0^+$. The asymptotic expansion of their approximate solution for $\hat{F}$ agrees with the asymptotic solution for $\hat{F}$ up to order $k^4$. Since an asymptotic solution for $\hat{J}$ has not yet been found in the limit $k \to 0^+$, they did not discuss the accuracy of $\hat{J}$. However we will discuss the accuracy of this approximate solution compared to a numerical solution for $\hat{J}$ in Chapter 4.4.

Antipov [4] reduced the electrostatic problem to a Riemann problem (an initial value problem with piecewise constant initial data [14]), which was then solved to obtain the exact solution for $\hat{J}$. However, to obtain this solution Antipov [4] took the total evaporative flux to be a prescribed constant, which contradicts the results of other authors, such as Cooke [20], who have shown $\hat{F}$ to be a function of $k$.

Laraqi [43], working in the context of electrostatics, combined the behaviour of $\hat{F}$ for a spherical-cap droplet (for which $F = 4b$) and the behaviour of $\hat{F}$ for an annular droplet in the limit $k \to 1^-$ (for which $F = 0$) and used a correlation method, described by Churchill & Usagi [16], to obtain an approximate solution for $\hat{F}$. The accuracy of this approximate solution will be discussed in Chapter 4.4.

Willert *et al.* [78], working in the context of an annular punch, obtained an approximate solution for $F$ by posing a simple form of $F$, namely $F = 4(1 - k^n)^m$. They used Boundary Element Method (BEM) simulations to determine best possible values of $n$ and $m$, which were found to be $n = 2.915$, and $m = 0.147$. The accuracy of this approximate solution will be discussed in Chapter 4.4.

Popov *et al.* [64, Chapter 10] give a very useful review of numerical, asymptotic and approximate solutions for the local and total evaporative flux, including the work of Cooke [20], Collins [18], Clements & Love [17], Gladwell & Gupta [36], and Willert *et al.* [78] discussed previously.

## 1.7    Presentation of work

Aspects of the following work have appeared in oral presentations by the author at the following scientific meetings: Droplets 2021 in August 2021, presented virtually from Darmstadt, Germany; British Applied Mathematics Colloquium in April 2022, presented virtually at the hybrid event in Loughborough; 35th Scottish Fluid Mechanics Meeting in May 2022, held in person in Oban; and UK Fluids Conference 2022 in September 2022, held in person in Sheffield.

## 1.8    Thesis Overview

The aim of this thesis is to consider the evaporation of a sessile annular droplet in different modes of evaporation, and to determine the resulting deposition patterns that occur for both spatially-uniform and diffusion-limited evaporative fluxes.

In Chapter 2, we formulate the mathematical problem of an evaporating annular droplet, namely the governing equations, associated boundary conditions and the local and total evaporative fluxes.

In Chapter 3, we determine geometry of an annular droplet, deriving the expression for the profile, volume and inner contact angle of a thin annular droplet.

In Chapter 4, we derive expressions for the concentration of vapour in the atmosphere and the local and total evaporative fluxes. We obtain numerical solutions,

utilising COMSOL Multiphysics® [19] for $\hat{c}$ and hence obtain numerical solutions for $\hat{J}$ and $\hat{F}$. We also make use of the method described by Cooke [18] to solve for $\hat{F}$ without having to first solve for either $\hat{c}$ or $\hat{J}$. We also discuss the asymptotic solution for $\hat{F}$ in the limit $k \to 0^+$ obtained by Collins [18], and the asymptotic solutions for $\hat{J}$ and $\hat{F}$ in the limit $k \to 1^-$ obtained by Leppington & Levine [47]. Finally, we discuss several formulations of approximate solutions of $\hat{F}$, including those obtained by Gladwell & Gupta [36], Laraqi [43], and Willert *et al.* [78].

In Chapter 5, we consider four modes of evaporation for an evaporating annular droplet, and derive expressions for the evolution and lifetime of the droplet in each of these modes for both spatially-uniform and diffusion-limited evaporative fluxes. We also compare the lifetimes of the droplet in the different modes with those of a spherical-cap shaped droplet.

In Chapter 6, we consider the evaporation of a particle-laden annular droplet. We solve the hydrodynamic problem within the droplet to determine the depth-averaged velocity and derive expressions for the concentration, and therefore the mass, of suspended particles in the bulk of the droplet. We then derive the expressions for the mass of suspended particles at both of the contact lines. We then compare the theoretical predictions for the spatially-uniform and the diffusion-limited evaporative fluxes.

Finally, in Chapter 7, we summarise the results obtained, draw conclusions and suggest possible directions for future work.

# Chapter 2

# Problem Formulation

Consider the evaporation of a thin, axisymmetric, annular droplet on a planar substrate. We work relative to cylindrical coordinates $(\hat{r}, \hat{z})$ with the substrate located at $\hat{z} = 0$ and the axis of symmetry aligned with the axis of the droplet, perpendicular to the substrate, as sketched in Figure 2.1. The annular droplet has an inner contact line located at $\hat{r} = \hat{a}(\hat{t})$, an outer contact line at $\hat{r} = \hat{b}(\hat{t})$, a profile $\hat{h}(\hat{r}, \hat{t})$, and a volume $\hat{V}(\hat{t})$, where $\hat{t}$ denotes time. At $\hat{t} = 0$, $\hat{a}$ and $\hat{b}$ take the initial values $\hat{a}(0) = \hat{a}_0$ and $\hat{b}(0) = \hat{b}_0$. The droplet occupies the region $\hat{a} \leq \hat{r} \leq \hat{b}$ and $0 \leq \hat{z} \leq \hat{h}(\hat{r}, \hat{t})$, as shown in Figure 2.1.

The inner contact angle that the free surface of the droplet makes with the substrate at the inner contact line is denoted by $\hat{\theta}_a = \hat{\theta}_a\left(\hat{t}\right)$, and the outer contact angle that the droplet makes with the substrate at the outer contact line is denoted by $\hat{\theta}_b = \hat{\theta}_b(\hat{t})$. The droplet is assumed to be thin, and so, in particular, the inner and outer contact angles are small (i.e. $\hat{\theta}_a \ll 1$ and $\hat{\theta}_b \ll 1$). At $\hat{t} = 0$, $\hat{\theta}_b$ takes the initial value $\hat{\theta}_b(0) = \hat{\theta}_{b0}$ and $\hat{\theta}_a(0)$ takes the initial value $\hat{\theta}_{a0}$. Note that $\hat{\theta}_a$ and $\hat{\theta}_b$ will, in general, not be equal. Throughout, variables with hats will denote dimensional

19
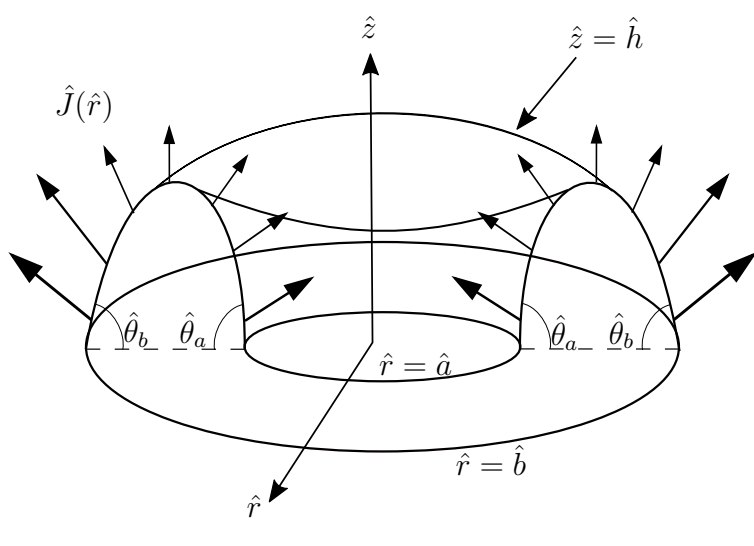
Figure 2.1: A sketch of the geometry of an annular droplet.

variables.

Working in the diffusion-limited regime (see, for example, the recent review by Wilson & D'Ambrosio [79]), and assuming that the diffusion coefficient of vapour in the atmosphere $\hat{D}$ is constant, the concentration of vapour $\hat{c}(\hat{r}, \hat{z}, \hat{t})$ in the atmosphere satisfies Laplace's equation,

$$\nabla^2 \hat{c} = \frac{1}{\hat{r}} \frac{\partial}{\partial \hat{r}} \left( \hat{r} \frac{\partial \hat{c}}{\partial \hat{r}} \right) + \frac{\partial^2 \hat{c}}{\partial \hat{z}^2} = 0, \tag{2.1}$$

subject to the mixed boundary conditions

$$\hat{c} = \hat{c}_{\text{sat}} \quad \text{on} \quad \hat{z} = 0 \quad \text{for} \quad \hat{a} \leq \hat{r} \leq \hat{b}, \tag{2.2}$$

$$\hat{c} \to \hat{c}_\infty \quad \text{as} \quad \hat{r}^2 + \hat{z}^2 \to \infty, \tag{2.3}$$

$$\frac{\partial \hat{c}}{\partial \hat{z}} = 0 \quad \text{on} \quad \hat{z} = 0 \quad \text{for} \quad 0 \leq \hat{r} < \hat{a}, \quad \hat{b} < \hat{r}, \tag{2.4}$$

where the boundary condition (2.2) imposes that $\hat{c}$ takes the constant saturation

concentration $\hat{c}_{\mathrm{sat}}$ ($> \hat{c}_\infty$) on the free surface of the droplet, (2.3) imposes the constant far-field vapour concentration $\hat{c}_\infty$, and (2.4) corresponds to zero flux of vapour through the substrate. Note that since the droplet is thin, the boundary condition (2.2) imposed on $\hat{z} = 0$ is asymptotically equivalent to imposing it on $\hat{z} = \hat{h}$.

The local evaporative flux $\hat{J} = \hat{J}(\hat{r}, \hat{t})$ from the free surface of the droplet is given by

$$\hat{J} = -\hat{D}\frac{\partial \hat{c}}{\partial \hat{z}} \quad \text{on} \quad \hat{z} = 0 \quad \text{for} \quad \hat{a} \leq \hat{r} \leq \hat{b}. \tag{2.5}$$

The total evaporative flux $\hat{F} = \hat{F}(\hat{t})$ of vapour from the droplet is given by the integral of the local evaporative flux (2.5) over the free surface of the droplet, namely

$$\hat{F} = 2\pi \int_{\hat{a}}^{\hat{b}} \hat{J}(\hat{r}, \hat{t})\hat{r}\, \mathrm{d}\hat{r}. \tag{2.6}$$

Note that $\hat{c}$, $\hat{J}$ and $\hat{F}$ depend on time parametrically via $\hat{a}$, $\hat{b}$, $\hat{\theta}_a$ and $\hat{\theta}_b$. We scale and non-dimensionalise the problem as follows. In the atmosphere we write

$$\hat{c} = \hat{c}_\infty + (\hat{c}_{\mathrm{sat}} - \hat{c}_\infty)\, c, \quad \hat{J} = \frac{\hat{D}\, (\hat{c}_{\mathrm{sat}} - \hat{c}_\infty)}{\hat{b}_0} J, \quad \hat{F} = \hat{b}_0 \hat{D}\, (\hat{c}_{\mathrm{sat}} - \hat{c}_\infty)\, F,$$

$$\hat{t} = \frac{\hat{\rho}\hat{b}_0^2\hat{\theta}_{b0}}{\hat{D}\, (\hat{c}_{\mathrm{sat}} - \hat{c}_\infty)} t, \quad \hat{r} = \hat{b}_0 r, \quad \hat{z} = \hat{b}_0 z, \quad \hat{a} = \hat{b}_0 a, \quad \hat{b} = \hat{b}_0 b, \tag{2.7}$$

where $\hat{\rho}$ is the constant density of the fluid within the droplet. Within the droplet, the non-dimensionalisation of the variables are the same except that $\hat{z} = \hat{b}_0\hat{\theta}_{b0}z$ and with the additions

$$\hat{p} = \hat{p}^a + \frac{\hat{\sigma}\hat{\theta}_{b0}}{\hat{b}_0}p, \quad \hat{\mathbf{u}} = (\hat{u}, \hat{w}) = \left(\frac{\hat{D}(\hat{c}_{\mathrm{sat}} - \hat{c}_\infty)}{\hat{\rho}\hat{b}_0\hat{\theta}_{b0}}u, \frac{\hat{D}(\hat{c}_{\mathrm{sat}} - \hat{c}_\infty)}{\hat{\rho}\hat{b}_0}w\right), \tag{2.8}$$

$$\hat{h} = \hat{b}_0\hat{\theta}_{b0}h, \quad \hat{\theta}_a = \hat{\theta}_{b0}\theta_a, \quad \hat{\theta}_b = \hat{\theta}_{b0}\theta_b, \quad \hat{V} = \hat{b}_0^3\hat{\theta}_{b0}V,$$

where $\hat{p}(\hat{r}, \hat{z}, \hat{t})$ is the pressure in the bulk of the droplet, $\hat{\sigma}$ is the constant surface tension, and $\hat{\mathbf{u}}(\hat{r}, \hat{z}, \hat{t})$ is the velocity of the fluid in the bulk of the droplet.

As a consequence of the scalings used $b_0 = 1$ and $\theta_{b0} = 1$. We define the ratio of the radii of the contact lines as

$$k(t) = \frac{a(t)}{b(t)}. \tag{2.9}$$

The initial value of $k$ is $k(0) = k_0 = a_0/b_0 = a_0$, and $0 \leq k \leq 1$. Using (2.7), Laplace's equation (2.1) remains unchanged and the boundary conditions (2.2)–(2.4) become

$$c = 1 \quad \text{on} \quad z = 0 \quad \text{for} \quad a \leq r \leq b, \tag{2.10}$$

$$c \to 0 \quad \text{as} \quad r^2 + z^2 \to \infty, \tag{2.11}$$

$$\frac{\partial c}{\partial z} = 0 \quad \text{on} \quad z = 0 \quad \text{for} \quad 0 \leq r < a, \quad b < r, \tag{2.12}$$

and the local evaporative flux from the free surface of the droplet is

$$J = -\frac{\partial c}{\partial z} \quad \text{on} \quad z = 0 \quad \text{for} \quad a \leq r \leq b. \tag{2.13}$$

In the diffusion-limited case the local evaporative flux can be expressed in the form

$$J_{\mathrm{DL}} = \frac{1}{b}\mathcal{J}_{\mathrm{DL}}\left(\frac{r}{b}, k\right) \tag{2.14}$$

and the total evaporative flux can be expressed in the form

$$F_{\mathrm{DL}} = b\mathcal{F}_{\mathrm{DL}}(k), \tag{2.15}$$

22

where $\mathcal{J}_{\mathrm{DL}}$ will be obtained numerically, asymptotically, and approximately, and $\mathcal{F}_{\mathrm{DL}}$ will be obtained numerically and asymptotically in the asymptotic limits $k \to 0^+$ and $k \to 1^-$ in Section 4.

In addition to diffusion-limited evaporation, we also consider the case of a spatially-uniform evaporative flux in which $J_{\mathrm{U}} \equiv J_0$ is a constant. In order to compare the evolution and lifetimes between a spatially-uniform evaporative flux and a diffusion-limited evaporative flux, we chose a spatially-uniform evaporative flux that has the same total evaporative flux, $F_{\mathrm{DL}}$, as the diffusion-limited flux in the limits $k \to 0^+$ and $k \to 1^-$. We therefore choose

$$J_{\mathrm{U}} = J_0 = \frac{4}{\pi b}, \tag{2.16}$$

then, using (2.6), $F_{\mathrm{U}}$ is

$$F_{\mathrm{U}} = b\mathcal{F}_{\mathrm{U}}(k), \tag{2.17}$$

where

$$\mathcal{F}_{\mathrm{U}}(k) = 4(1 - k^2). \tag{2.18}$$

The volume of the droplet is given by

$$V(t) = 2\pi \int_a^b h(r) r \, \mathrm{d}r, \tag{2.19}$$

and $V$ evolves according to the global mass balance condition,

$$\frac{\mathrm{d}V}{\mathrm{d}t} = -F = -2\pi \int_a^b J(r) r \, \mathrm{d}r. \tag{2.20}$$

The droplet begins evaporating at $t = 0$ with initial volume $V_0$ and the lifetime of the droplet, i.e. the time at which the droplet has fully evaporated, denoted by

23

$t = t_{\text{lifetime}}$, is determined by

$$V = 0 \qquad \text{at} \qquad t = t_{\text{lifetime}}. \tag{2.21}$$

# Chapter 3

# Droplet Geometry

In situations in which the droplet is sufficiently small, and surface tension is sufficiently strong (i.e. in situations where the droplet is smaller than the capillary number $l = \sigma/(\rho g)^{1/2}$, where $g$ denotes the magnitude of the acceleration due to gravity), the Stokes equations reduce to the statement that the leading order pressure $p = p(r, z, t)$ within the droplet satisfies

$$\nabla p = 0, \tag{3.1}$$

subject to the Young–Laplace equation at the free surface of the droplet, namely

$$p = \kappa \quad \text{on} \quad z = h, \tag{3.2}$$

in which the dimensional pressure $\hat{p}$ has been scaled according to (2.8) and where $\kappa = \nabla \cdot \mathbf{n}$ denotes the mean curvature of the gas-liquid interface of the droplet, and $\mathbf{n}$ denotes the outward unit normal vector to the free surface.

Equation (3.1) shows that the pressure is independent of $r$ and $z$, and so $p$ is a

function of time only. At leading order in the limit $\hat{\theta}_{b0} \to 0$, (3.2) reduces to

$$p = -\frac{1}{r}\frac{\partial}{\partial r}\left(r\frac{\partial h}{\partial r}\right) \quad \text{on} \quad z = h, \tag{3.3}$$

which by using the fact that $\partial p / \partial r = 0$ and differentiating with respect to $r$ yields the following equation for the profile of the droplet,

$$\frac{\partial}{\partial r}\left(\frac{1}{r}\frac{\partial}{\partial r}\left(r\frac{\partial h}{\partial r}\right)\right) = 0. \tag{3.4}$$

The general solution to (3.4) is of the form

$$h(r) = c_1 r^2 + c_2 + c_3 \log r, \tag{3.5}$$

where $c_i$ for $i = 1, 2, 3$ are coefficients to be determined by the boundary conditions.

The boundary conditions at the inner and outer contact lines are

$$h = 0 \quad \text{at} \quad r = a, \tag{3.6}$$

$$\frac{\partial h}{\partial r} = \theta_a \quad \text{at} \quad r = a, \tag{3.7}$$

$$h = 0 \quad \text{at} \quad r = b, \tag{3.8}$$

$$\frac{\partial h}{\partial r} = -\theta_b \quad \text{at} \quad r = b. \tag{3.9}$$

Here (3.6) and (3.8) represent the free surface of the droplet touching the substrate at the contact lines, while (3.7) and (3.9) represent the contact angles that the droplet makes with the substrate at the contact lines.

Note that there are four boundary conditions on the profile of the droplet and only three unknown coefficients $c_i$, and so $a$, $b$, $\theta_a$ and $\theta_b$ are not independent of each other. In practice, we therefore use (3.6), (3.8) and (3.9) to find an expression for
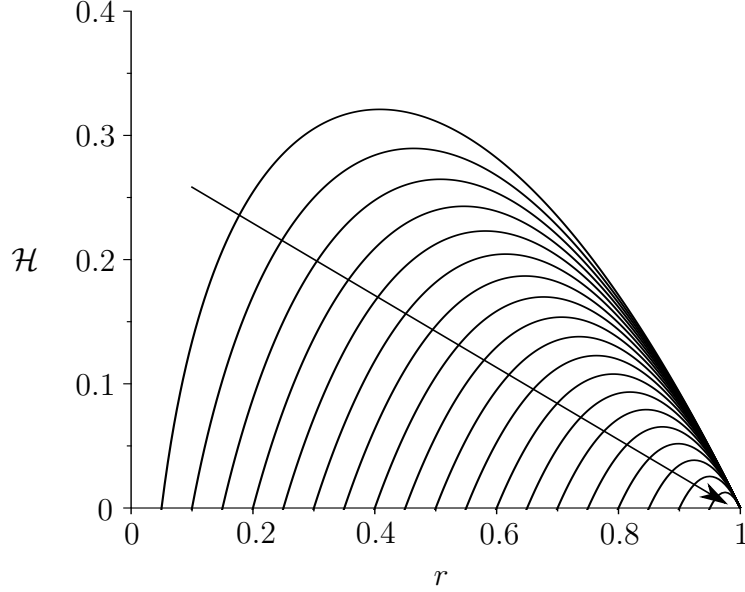
Figure 3.1: $\mathcal{H}$ given by equation (3.11) as a function of $r$, with $b = 1$ and for $k = 0.05, 0.10, \ldots, 0.95$. The arrow the direction of increasing $k$.

the profile of the droplet, and use (3.7) to find an expression for the inner contact angle of the droplet in terms of $k$ and $\theta_b$.

Imposing the boundary conditions (3.6), (3.8) and (3.9) on the general solution for $h(r, t)$ (3.5) yields

$$h(r,t) = b\theta_b \mathcal{H}\left(\frac{r}{b}, k\right), \tag{3.10}$$

where $\mathcal{H}$ is given by

$$\mathcal{H}\left(\frac{r}{b}, k\right) = \frac{\left(1 - \frac{r^2}{b^2}\right)\log k - (1 - k^2)\log\left(\frac{r}{b}\right)}{2\log k + 1 - k^2}. \tag{3.11}$$

Figure 3.1 shows $\mathcal{H}$ given by (3.11) for various values of $k$ for $b = 1$. This figure shows that in the limit $k \to 0^+$, the profile of the droplet is skewed to the right (i.e. the maximum value of the profile corresponds to a value of $r$ lower than the midpoint between the contact lines), and in the limit $k \to 1^-$ the profile of the

27

droplet becomes symmetric. This figure clearly illustrates that the inner and the outer contact angles are never equal. In particular, Figure 3.1 shows that the outer contact angle is the same for all values of $k$, but that the inner contact angle is a decreasing function of $k$. This difference in the contact angles is a consequence of the quasi-static shape of the droplet; a quasi-static shape with equal contact angles is impossible. By examining the behaviour of (3.11) in the limits $k \to 0^+$ and $k \to 1^-$, we can see that $\mathcal{H}(r)$ tends to

$$\mathcal{H} = \frac{(1-r^2)\log k - \log r}{1 + 2\log k} + \frac{k^2 \log k(1 - r^2 + 2\log r)}{(1 + 2\log k)^2} + O\left(\frac{k^4 \log k}{(1 + 2\log k)^3}\right) \to \left(\frac{1 - r^2}{2}\right)^- \tag{3.12}$$

in the limit $k \to 0^+$, showing that at leading order $\mathcal{H}$ reduces to the expression for the profile of a spherical-cap droplet, and

$$\mathcal{H} = R(1 - R)(1 - k) + \frac{R(1 - R)^2}{3}(1 - k)^2 + O\left((1 - k)^3\right) \to 0^+ \tag{3.13}$$

in the limit $k \to 1^-$, where $r = k + (1 - k)R$.

Using the boundary condition (3.7) on (3.10) yields the expression for the inner contact angle $\theta_a(t)$,

$$\theta_a = \theta_b \mathcal{T}(k), \tag{3.14}$$

where $\mathcal{T}(k)$ is given by
$$\mathcal{T} = \frac{2k^2 \log k + 1 - k^2}{k\left(k^2 - 1 - 2\log k\right)}. \tag{3.15}$$

Figure 3.2 shows $\mathcal{T} = \theta_a/\theta_b$ given by (3.14) plotted as a function of $k$. In particular, Figure 3.2 shows that the inner and outer contact angles are not equal and, in particular, that their ratio, $\theta_a/\theta_b$ satisfies $\theta_a/\theta_b > 1$ for all $0 \le k < 1$. In the
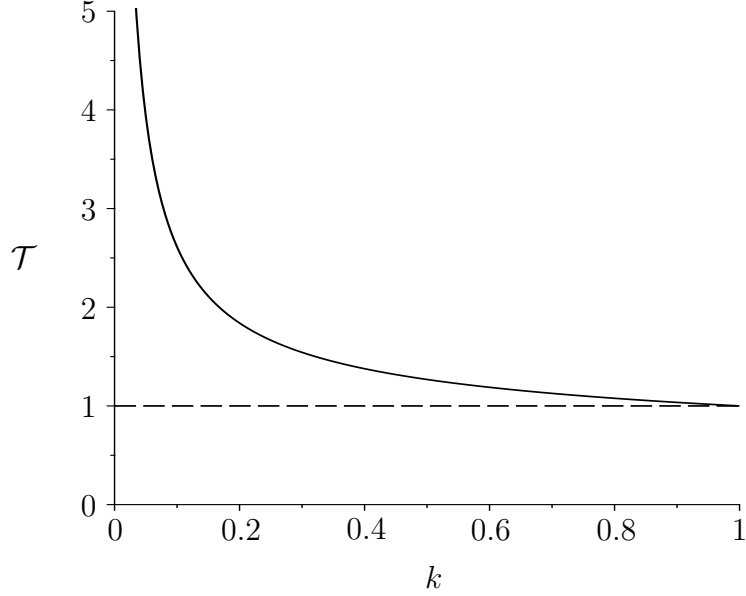
Figure 3.2: $\mathcal{T} = \theta_a/\theta_b$ given by equation (3.14) as a function of $k$. The dashed line represents $\mathcal{T} = 1$.

limit $k \to 1^-$, Figure 3.2 shows that $\mathcal{T} \to 1^+$, i.e. that the contact angles tend to the same value. Figure 3.2 also shows that $\mathcal{T}$ is a monotonically decreasing function of $k$. Specifically, $\mathcal{T}$ satisfies

$$\mathcal{T} = \frac{-1}{k(1 + 2\log k)} - \left(\frac{2\log k}{2\log k + 1}\right)^2 k + O\left(\frac{k^3(\log k)^2}{(1 + 2\log k)^3}\right) \to \infty \qquad (3.16)$$

in the limit $k \to 0^+$, and

$$\mathcal{T} = 1 + \frac{1 - k}{3} + \frac{2(1 - k)^2}{9} + O\left((1 - k)^3\right) \to 1^+ \qquad (3.17)$$

in the limit $k \to 1^-$.

Evaluating the volume of the droplet (2.19) using the expression for the $h(r, t)$ (3.10) gives the volume of the droplet to be

$$V = b^3 \theta_b \mathcal{V}(k), \qquad (3.18)$$

29
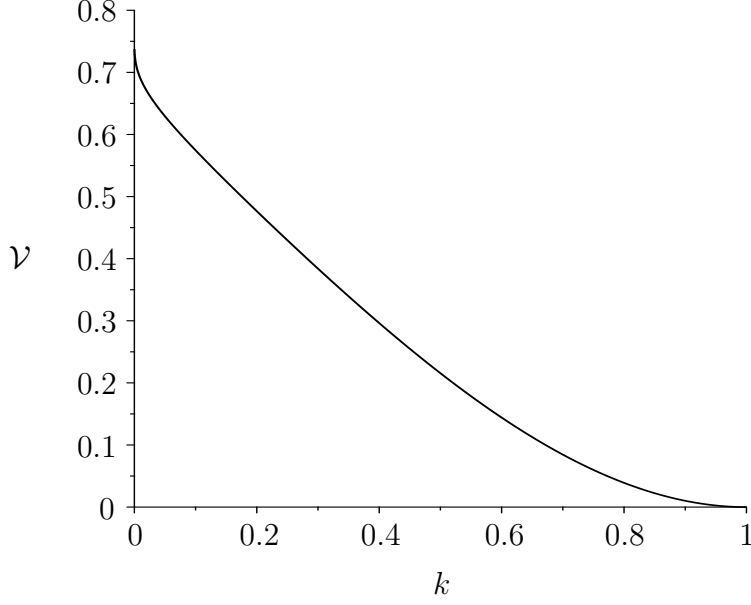
Figure 3.3: $\mathcal{V}$ given by equation (3.19) as a function of $k$.

where $\mathcal{V}$ is given by

$$\mathcal{V} = \frac{\pi \left(1 - k^2\right) \left[\left(1 + k^2\right) \log k + 1 - k^2\right]}{2 \left[2 \log k + 1 - k^2\right]}. \tag{3.19}$$

Figure 3.3 shows $\mathcal{V}$ plotted as a function of $k$. Analysing the behaviour of (3.18) in the limits $k \to 0^+$ and $k \to 1^-$ shows that $\mathcal{V}(t)$ reduces to the corresponding value for $\mathcal{V}$ for a spherical-cap droplet (namely $\mathcal{V} = \pi/4$), satisfying

$$\mathcal{V} = \frac{\pi}{2} \frac{1 + \log k}{1 + 2 \log k} - \frac{\pi \left(3 \log k + 1\right)}{2 \left(2 \log k + 1\right)^2} k^2 + O \left(k^4 \frac{\log k^3}{\left(1 + 2 \log k\right)^3}\right) \to \frac{\pi}{4}^- \tag{3.20}$$

in the limit $k \to 0^+$, and

$$\mathcal{V} = \frac{\pi}{3} \left(1 - k\right)^2 - \frac{1}{9} \pi \left(1 - k\right)^3 + O \left(\left(1 - k\right)^4\right) \to 0^+ \tag{3.21}$$

in the limit $k \to 1^-$.

30

# Chapter 4

# Solutions for $c$, $J$ and $F$

In order to determine the evolution of an annular droplet, we first need to determine the local evaporative flux $J$ and hence the total evaporative flux $F$. While no simple, closed-form solution for $c$ (i.e. a solution to the problem (2.1), (2.11)–(2.12)) is available, numerical, asymptotic and approximate solutions for $J$ and $F$ can all be determined. In Chapter 4.1, we discuss numerical solutions for $c$, $J$ and $F$. In Chapter 4.1.1 we discuss how to obtain numerical solutions for $c$, $J$ and $F$ using Finite Element Methods (FEM) implemented within COMSOL Multiphysics®  [19]. In Chapter 4.1.2, we discuss how to obtain a numerical solution for $F$ using Chebyshev–Gauss quadrature based on the approach of Cooke [20]. In Chapter 4.2 we describe the asymptotic solutions for $F$ in the limit $k \to 0^+$. In Chapter 4.3 we describe the asymptotic solutions for $J$ and $F$ in the limit $k \to 1^-$, and in Chapter 4.4 we describe several approximate solutions for $F$.

## 4.1 Numerical solutions for $c$, $J$ and $F$

### 4.1.1 Solutions for $c$, $J$ and $F$ using COMSOL Multiphysics

COMSOL Multiphysics [19] was used to directly solve Laplace's equation (2.1) numerically subject to the boundary conditions (2.11)–(2.12) for $c(r, z, t)$ using the Finite Element Method (FEM), and hence calculate the numerical solutions for $\mathcal{J}$, denoted by $\mathcal{J}_{\text{COMSOL}}$, and $\mathcal{F}$, denoted by $\mathcal{F}_{\text{COMSOL}}$. In order to create the plots of the numerical results, the numerical data from COMSOL was imported into Maple™ [49], which was used to create a series of cubic spline fits to the data. These splines were then plotted to generate Figures 4.1 and 4.2.

Figure 4.1 shows a contour plot of the concentration of vapour $c$ obtained using COMSOL for $k = 0.2$. In particular, this figure shows that in the far-field the contours become circular, as they would be for a spherical-cap droplet.

Figure 4.2 shows plots of $J_{\text{COMSOL}}$ as a function of $r$ for $k = 0, 0.2, 0.4, 0.6, 0.8$. In the case of a thin droplet there is a square root singularity in $J$ at the contact line. In the case of an annular droplet, a singularity exists at both the inner and outer contact lines. A local analysis of the contact lines shows that these singularities are also square-root singularities, as in the case of a spherical-cap droplet. Figure 4.2 shows that $\mathcal{J}$ is smaller close to the inner contact line than it is close to the outer contact line. This is due to a "self-shielding" effect, in which the proximity of the rest of the droplet inhibits evaporation at the inner contact line relative to that the outer contact line. A corresponding "shielding" phenomenon is well known in the context of multiple spherical-cap droplets (see, for example, Wray *et al.* [81] and Masoud *et al.* [51]).
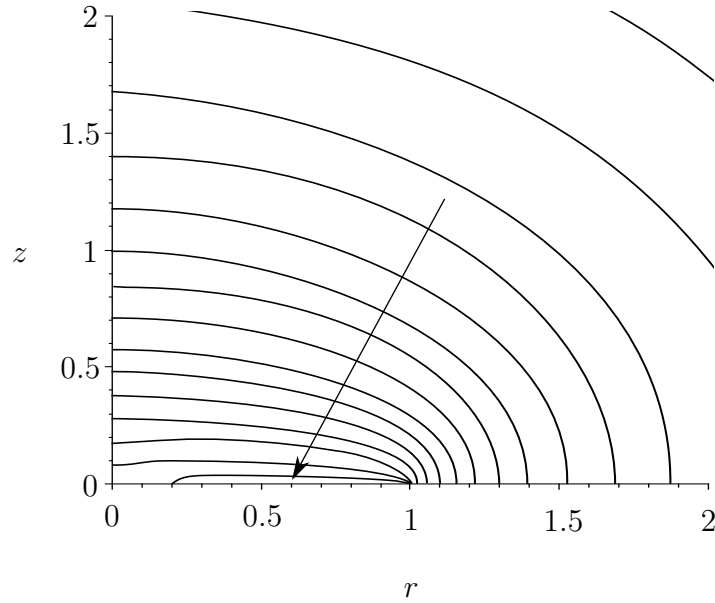
Figure 4.1: Contour plot of $c(r, z)$ obtained by solving (2.1), (2.11)–(2.12) using COMSOL for $k = 0.2$. Contours are plotted at $c = 0.25, 0.30, 0.35, \ldots, 0.95$, where the arrow indicates the direction of decreasing $c$.
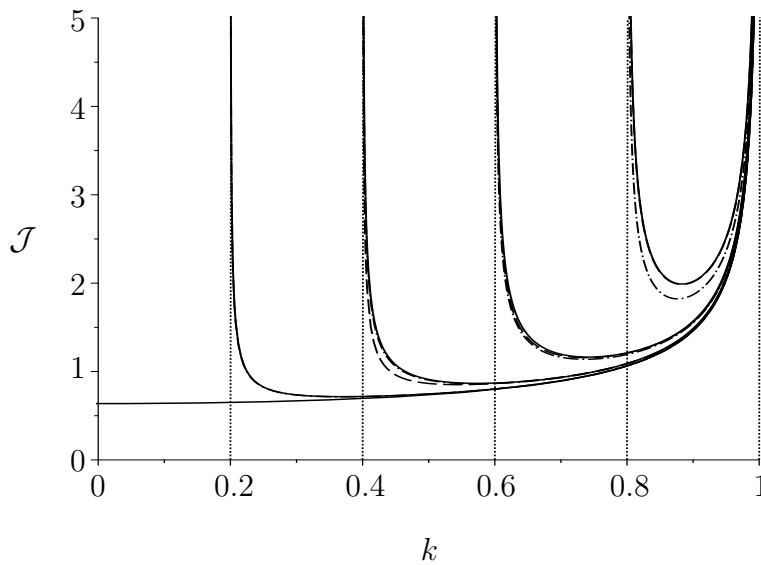


Figure 4.2: Numerical solutions $\mathcal{J}_{\text{COMSOL}}(r)$ for $k = 0, 0.2, 0.4, 0.6, 0.8$ obtained using COMSOL plotted as a function of $r$. The dash-dot lines show the approximate solution of Gladwell & Gupta [36] given by (4.18) for $k = 0.2, 0.4, 0.6, 0.8$ and the dashed lines show the asymptotic solution for $\mathcal{J}$ in the limit $k \to 1^-$ given by (4.16) for $k = 0.6, 0.8$.

33

## 4.1.2 Numerical solution for $F$ using Chebyshev–Gauss quadrature

To confirm the results from COMSOL we use a second numerical method to solve for $F$ without first having to solve for $c$, as described by Cooke [20]. By taking a Hankel transform of Laplace's equation (2.1) and imposing the far-field condition (2.11), $c$ can be expressed as

$$c(r, z) = \int_0^\infty A(\xi) e^{-\xi z} J_0(\xi r) \, \mathrm{d}\xi, \tag{4.1}$$

where $A(\xi)$ is an unknown function of $\xi$, and $J_0(\cdot)$ is a Bessel function of the first kind of order zero. Substituting the expression of $c$ given in (4.1) into the boundary conditions (2.10) and (2.12) yields

$$\int_0^\infty A(\xi) J_0(\xi r) \, \mathrm{d}\xi = 0 \quad \text{for} \quad 0 \le r < a, \tag{4.2}$$

$$\int_0^\infty \xi^{-1} A(\xi) J_0(\xi r) \, \mathrm{d}\xi = 1 \quad \text{for} \quad a \le r \le b, \tag{4.3}$$

$$\int_0^\infty A(\xi) J_0(\xi r) \, \mathrm{d}\xi = 0 \quad \text{for} \quad b < r < \infty. \tag{4.4}$$

Cooke [20], extending to approach of Noble [60] to a system of three (rather than two) integral equations, reduced the integral equations (4.2)–(4.4) to a single Fredholm integral equation of the first kind, and expressed the total evaporative flux $\mathcal{F}$ as

$$\mathcal{F} = 4 \int_a^b \frac{s G(s)}{(s^2 - a^2)^{1/2}} \, \mathrm{d}s, \tag{4.5}$$

where $G(s)$ satisfies the integral equation

$$G(s) = \frac{s}{\sqrt{s^2 - a^2}} - \frac{4}{\pi^2} \frac{s}{\sqrt{s^2 - a^2}} \int_a^b \frac{q \, G(q)}{\sqrt{q^2 - a^2}} K(s, q) \, \mathrm{d}q, \tag{4.6}$$

in which we have defined

$$K(s,q) = \frac{1}{2(s^2 - q^2)}\left[\frac{s^2 - a^2}{s}\log\left(\frac{s+a}{s-a}\right) - \frac{q^2 - a^2}{q}\log\left(\frac{q+a}{q-a}\right)\right]. \qquad (4.7)$$

Cooke [20] showed that the integrals in equations (4.5) and (4.6) can be solved using quadrature. To do this, we introduce the substitutions

$$s(x) = \frac{1}{2}((b-a)x + b + a), \qquad G(s) = f(s)\frac{\sqrt{s+a}}{\sqrt{b-s}}. \qquad (4.8)$$

The integral equation for $G(s)$ given by (4.6) becomes an integral equation for $f(s(x))$, namely

$$f(s(x))\frac{(s(x)+a)\sqrt{s(x)-a}}{s(x)\sqrt{b-s(x)}} = 1 - \frac{4}{\pi^2}\int_{-1}^{1}\frac{s(y)\,f(s(y))}{\sqrt{1-y^2}}K(s(x),s(y))\,dy, \qquad (4.9)$$

where $y$ is a variable of integration. The integral in (4.9) can be approximated using Chebyshev–Gauss quadrature with $n$ Chebyshev points, where the Chebyshev points are defined by

$$\cos\left(\frac{(2i-1)\pi}{2n}\right) \quad \text{for} \quad i = 1, 2, \ldots, n. \qquad (4.10)$$

Then approximating the integral on the right hand side of (4.9) yields

$$\int_{-1}^{1}\frac{s(y)\,f(s(y))}{\sqrt{1-y^2}}K(s(x),s(y))\,dy \approx \sum_{i=1}^{n}\frac{\pi}{n}s(y_i)\,f(s(y_i))\,K(s(x),s(y_i)). \qquad (4.11)$$

With this, and evaluating at $x = x_j$, $j = 1, 2, \ldots, n$ where $x_j$ are Chebyshev points

defined by (4.10), (4.9) becomes

$$f(s(x_j)) \frac{(s(x_j) + a)\sqrt{s(x_j) - a}}{s(x_j)\sqrt{b - s(x_j)}} \approx 1 - \frac{4}{\pi} \sum_{i=1}^{n} \frac{1}{n} s(y_i)\, f(s(y_i))\, K(s(x_j), s(y_i)). \quad (4.12)$$

The system of equations (4.12) comprises $n$ equations for the $n$ unknown values of $f(s(y_i))$ for $i = 1, 2, \ldots, n$. We approximate (4.5) using the same procedure, substituting (4.8) into (4.5). Using Chebyshev–Gauss quadrature on (4.5), the approximate expression for the total evaporative flux, denoted by $\mathcal{F}_{\text{Cooke}}$, is then

$$\mathcal{F}_{\text{Cooke}} = 4 \int_{-1}^{1} \frac{s(y)\, f(s(y))}{\sqrt{1 - y^2}}\, \mathrm{d}y \approx \frac{4\pi}{n} \sum_{i=1}^{n} s(y_i)\, f(s(y_i)), \quad (4.13)$$

where $f(s(y_i))$ are obtained by solving the system of equations (4.12). Note that this method yields $\mathcal{F}_{\text{Cooke}}$ without having to calculate either $c$ or $J$.

Figure 4.3 shows $\mathcal{F}_{\text{Cooke}}$ calculated using $n = 300$ Chebyshev points in Maple™ [49]. Convergence of this method was verified by repeating the calculations using $n = 600$ Chebyshev points, which resulted in changes to $\mathcal{F}_{\text{Cooke}}$ of $O(10^{-9})$.

Figure 4.4 shows a log-log plot of the relative error, $e_{\text{rel}}$, between $\mathcal{F}_{\text{COMSOL}}$ and $\mathcal{F}_{\text{Cooke}}$, calculated according to

$$e_{\text{rel}} = \left| \frac{\mathcal{F}_{\text{Cooke}} - \mathcal{F}_{\text{COMSOL}}}{\mathcal{F}_{\text{Cooke}}} \right|. \quad (4.14)$$

This figure shows that $\mathcal{F}_{\text{COMSOL}}$ is in excellent agreement with $\mathcal{F}_{\text{Cooke}}$ for most values of $k$, with the maximum error in $\mathcal{F}_{\text{COMSOL}}$ in $0 \leq k \leq 0.9$ being $e_{\text{rel}} \approx 0.003$ at $k = 0.9$. However, the agreement between $\mathcal{F}_{\text{COMSOL}}$ and $\mathcal{F}_{\text{Cooke}}$ worsens in the limit $k \to 1^+$, and $e_{\text{rel}} \approx 0.201$ when $k = 0.9996$.
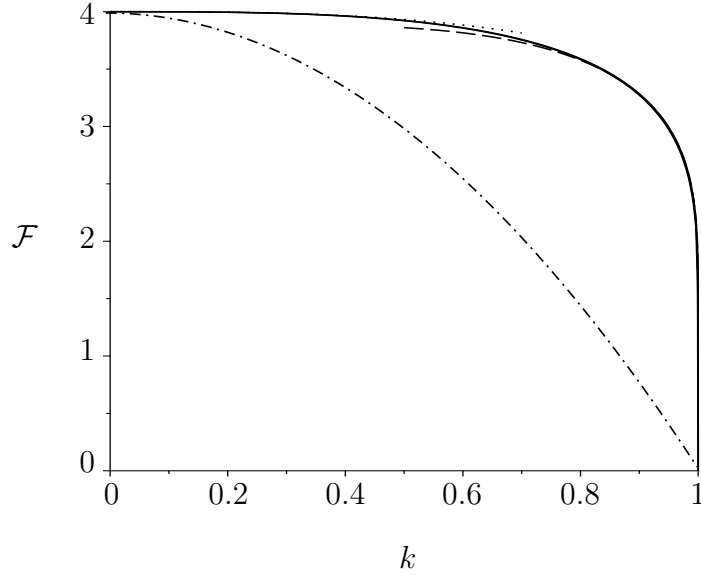
Figure 4.3: The numerical solution $\mathcal{F}_{\text{Cooke}}$ given by (4.13) plotted as a function of $k = a/b$. The visible dotted line represents the asymptotic solution for $\mathcal{F}$ in the limit $k \to 0^+$ given by (4.15). The dashed line represents the solution for $\mathcal{F}$ in the asymptotic limit $k \to 1^-$ given by (4.17). A dotted line shows the numerical solution $\mathcal{F}_{\text{COMSOL}}$ calculated using COMSOL, but it is impossible to see on the scale of this figure. A dash-dot line shows $\mathcal{F}_{\text{U}}$ given by (2.18).
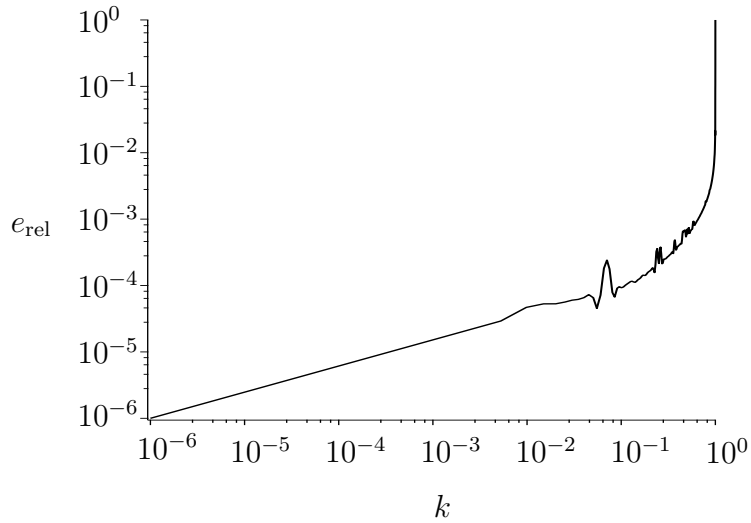


Figure 4.4: A log-log plot of the relative error, $e_{\text{rel}}$, between $\mathcal{F}_{\text{COMSOL}}$ and $\mathcal{F}_{\text{Cooke}}$ given by (4.14), plotted as a function of $k$.

37

## 4.2 Asymptotic solution for $F$ in the limit $k \to 0^+$

By reducing the problem (2.1), (2.11) and (2.12) to a Fredholm integral equation, which was then solved iteratively, Collins [18] gave the asymptotic solution for $\mathcal{F}$ as

$$\mathcal{F} = 4\left(1 - \frac{4}{3\pi^2}k^3 - \frac{8}{15\pi^2}k^5 - \frac{16}{27\pi^4}k^6\right) + O\left(k^7\right) \to 4^- \qquad (4.15)$$

in the limit $k \to 0^+$.

## 4.3 Asymptotic solutions for $J$ and $F$ in the limit $k \to 1^-$

Leppington & Levine [47] detailed a method for deriving the asymptotic solutions for $\mathcal{J}$ and $\mathcal{F}$ in the limit $k \to 1^-$. However, in doing so, they made a small but significant error when calculating the leading order term of $\mathcal{J}$. The details of this mistake, and the corrected solution are included in Appendix A. The corrected asymptotic solutions for $\mathcal{J}$ and the asymptotic solution for $\mathcal{F}$ are

$$\mathcal{J} = \frac{4(1-k)\log 2 - \log\left(\frac{32k}{1-k}\right)\left[(1-k)\log\left(\frac{32k}{1-k}\right)\log 2(r - kb) + 2 - 2\log 2\right]}{16\pi \log 2 \log\left(\frac{32k}{1-k}\right) r\sqrt{\left(\frac{r}{b} - k\right)\left(1 - \frac{r}{b}\right)}} + o(1-k) \qquad (4.16)$$

and

$$\mathcal{F} = \pi^2\left[\frac{1+k}{\log\dfrac{32}{1-k}} - \frac{1-k}{\left(\log\dfrac{32}{1-k}\right)^2}\right] + o(1-k). \qquad (4.17)$$

Figures 4.2 and 4.3 show plots of $\mathcal{J}$ (4.16) and $\mathcal{F}$ (4.17), respectively.

## 4.4 Approximate solutions for $J$ and $F$

Previous work on the solution of Laplace's equation in an annular geometry provides approximate solutions for $J$ and $F$.

By utilising a Papkovich–Neuber solution, and imposing suitable boundary conditions, Gladwell & Gupta [36] gave a very accurate approximate solution for $\mathcal{J}$ in the range $0 < k \leq 0.8$,

$$\mathcal{J}_{\mathrm{GG}}(r) = \frac{2}{\pi} \frac{b}{\sqrt{b^2 - r^2}} - \frac{12}{9\pi^2 - 4k^2} \left[ \frac{2k^3 b^3}{\pi r^3} S\left(\frac{r}{b}\right) + 3S\left(\frac{kb}{r}\right) \right], \tag{4.18}$$

where the function $S(x)$ is given by

$$S(x) = \arcsin(x) - \frac{x}{\sqrt{1 - x^2}} \quad \text{for} \quad 0 < x < 1. \tag{4.19}$$

Figure 4.2 shows a comparison between $\mathcal{J}_{\mathrm{GG}}$ given by (4.18) and $\mathcal{J}_{\mathrm{COMSOL}}$. Figure 4.2 shows that the approximate solution for $\mathcal{J}_{\mathrm{GG}}$ (4.18) agrees very well with $\mathcal{J}_{\mathrm{COMSOL}}$, particularly for smaller values of $k$. However this accuracy is reduced as $k$ increases.

Using (4.18), the corresponding approximate expression for $F$ is given by

$$\mathcal{F}_{\mathrm{GG}} = \sqrt{1 - k^2} + \frac{3k}{9\pi^2 - 4k^3} \left( 2\pi k^2 - 4k \arcsin k + \frac{3\pi}{2} k + \frac{3}{k} \arcsin k + 3\sqrt{1 - k^2} \right). \tag{4.20}$$

Expanding for small $k$ gives the asymptotic solution for $\mathcal{F}_{\mathrm{GG}}$ (4.15) in the limit $k \to 0^+$, with an error of $O(k^4)$.

Approximate solutions for $\mathcal{F}$ have also been given by Laraqi [43] and Willert et al. [78]. Laraqi [43] used a correlation method (from Churchill & Usagi [16]) to

39
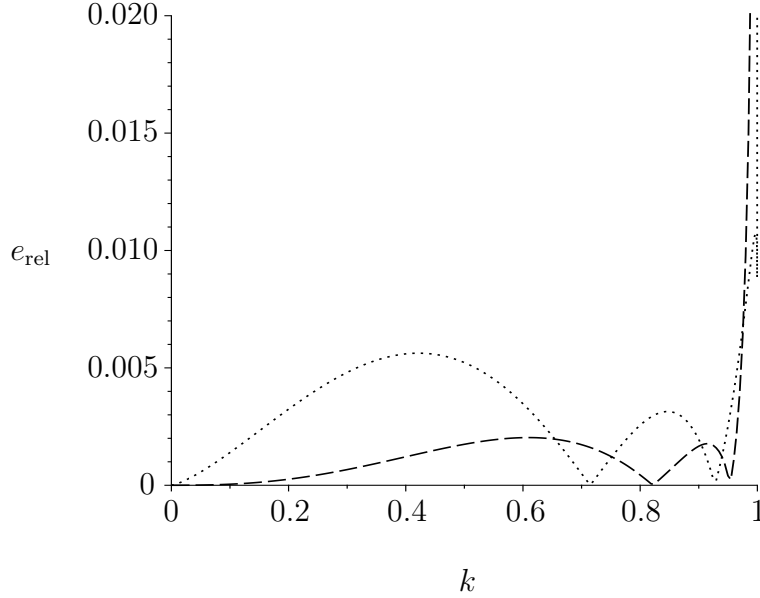
Figure 4.5: Plot of the relative error, $e_{\text{rel}}$, between $\mathcal{F}_{\text{Laraqi}}$ and $\mathcal{F}_{\text{Cooke}}$, shown with a dotted line, and the relative error between $\mathcal{F}_{\text{Willert}}$ and $\mathcal{F}_{\text{Cooke}}$, shown with a dashed line.

combine the behaviour of $\mathcal{F}$ in the case of a spherical-cap droplet (i.e. $\mathcal{F}_{\text{DL}} \to 4^-$ when $k \to 0^+$) and the behaviour of $\mathcal{F}$ in the limit $k \to 1^-$ (i.e. $\mathcal{F} \to 0^+$ in the limit $k \to 1^-$). Willert et al. [78] posed an approximate form for $\mathcal{F}$, namely $\mathcal{F} = 4(1 - k^n)^m$ and used BEM simulations to find best possible values of $n$ and $m$. The expressions due to Laraqi [43] ($\mathcal{F}_{\text{Laraqi}}$) and Willert et al. [78] ($\mathcal{F}_{\text{Willert}}$) are

$$\mathcal{F}_{\text{Laraqi}} = \frac{2\pi n}{\log\left[\left(\frac{8\exp(3/2)k}{1-k}\right)^n + \exp\frac{n\pi^2}{2}\right]} \quad \text{where} \quad n = 1.3, \tag{4.21}$$

$$\mathcal{F}_{\text{Willert}} = 4\left(1 - k^{2.915}\right)^{0.147}. \tag{4.22}$$

Figure 4.5 shows the relative error, $e_{\text{rel}}$, between $\mathcal{F}_{\text{Laraqi}}$ and $\mathcal{F}_{\text{Cooke}}$, and the relative error between $\mathcal{F}_{\text{Willert}}$ and $\mathcal{F}_{\text{Cooke}}$, calculated according to

$$e_{\text{rel}}(\mathcal{F}) = \left|\frac{\mathcal{F}_{\text{Cooke}} - \mathcal{F}}{\mathcal{F}_{\text{Cooke}}}\right|. \tag{4.23}$$

This figure shows that both $\mathcal{F}_{\text{Laraqi}}$ and $\mathcal{F}_{\text{Willert}}$ are in good agreement with $\mathcal{F}_{\text{Cooke}}$, except in the limit $k \to 1^-$, where the relative error of both approximations increases.

# Chapter 5

# Evolution and lifetime of an annular droplet

We now determine the evolution, and hence lifetime, of an annular droplet. To do this, we first need to specify the mode in which the droplet is evaporating. Due to the presence of the second (inner) contact line, there is a wider variety of possible modes in which an annular droplet can evaporate in when compared to a spherical-cap droplet. In the present work we consider the following four modes of evaporation:

- The pinned–pinned mode, in which both contact lines at $r = a$ and $r = b$ are fixed, and the contact angles $\theta_a(t)$ and $\theta_b(t)$ vary over time.

- The free–pinned mode, in which the outer contact line at $r = b$ is pinned and the inner contact angle $\theta_a$ is pinned and the radius of the inner contact line $r = a(t)$ and the inner contact angle $\theta_b(t)$ vary over time.

- The pinned–free mode, in which the inner contact line at $r = a$ is pinned and the outer contact angle $\theta_b$ is fixed, and the inner contact angle $\theta_a(t)$ and the

radius of the outer contact line $r = b(t)$ vary over time.

- The free–free mode, in which both contact angles $\theta_a$ and $\theta_b$ are fixed, and the positions of both of the contact lines at $r = a(t)$ and $r = b(t)$ vary over time.

## 5.1  Evolution and lifetime of an annular droplet evaporating in the pinned–pinned mode

In the pinned–pinned mode $a \equiv a_0$ and $b \equiv b_0$ so that $k \equiv k_0 = a_0/b_0 = a_0$ and $F = \mathcal{F}(k_0)$ are both constant throughout the evaporation. As a consequence of the scalings used in (2.7), $\theta_b = \theta_{b0} = 1$. The evolution of the droplet is determined from (2.20),

$$-\frac{\mathrm{d}V}{\mathrm{d}t} = -\frac{\partial V}{\partial \theta_b}\frac{\mathrm{d}\theta_b}{\mathrm{d}t} = -\mathcal{V}(k_0)\frac{\mathrm{d}\theta_b}{\mathrm{d}t} = \mathcal{F}(k_0). \tag{5.1}$$

Rearranging (5.1) gives

$$\frac{\mathrm{d}\theta_b}{\mathrm{d}t} = -\frac{\mathcal{F}(k_0)}{\mathcal{V}(k_0)}, \tag{5.2}$$

which can be solved subject to the initial condition, $\theta_b(0) \equiv \theta_{b0} = 1$, to yield

$$\theta_b = 1 - \frac{\mathcal{F}(k_0)}{\mathcal{V}(k_0)}t. \tag{5.3}$$

Using this expression for $\theta_b(t)$ (5.3), the evolution of $h(r,t)$, $\theta_a(t)$ and $V(t)$ can be determined from (3.10), (3.14), and (3.18),

$$h(r,t) = \frac{(1-r^2)\log k_0 - (1-k_0^2)\log r}{2\log k_0 + 1 - k_0^2}\left(1 - \frac{\mathcal{F}(k_0)}{\mathcal{V}(k_0)}t\right), \tag{5.4}$$

$$\theta_a(t) = \frac{2k_0^2\log k_0 + 1 - k_0^2}{k_0\left(k_0^2 - 1 - 2\log k_0\right)}\left(1 - \frac{\mathcal{F}(k_0)}{\mathcal{V}(k_0)}t\right), \tag{5.5}$$

$$V(t) = \frac{\pi(1-k_0^2)\left[(1+k_0^2)\log k_0 + 1 - k_0^2\right]}{2(2\log k_0 + 1 - k_0^2)}\left(1 - \frac{\mathcal{F}(k_0)}{\mathcal{V}(k_0)}t\right). \tag{5.6}$$

Then from (2.21) the expression for the lifetime of an annular drop evaporating in the pinned–pinned mode is

$$t_{\text{lifetime}} = \frac{\mathcal{V}(k_0)}{\mathcal{F}(k_0)}. \tag{5.7}$$

## 5.1.1 Evolution of an annular droplet evaporating in the pinned–pinned mode with a spatially-uniform evaporative flux

In the case of a spatially-uniform evaporative flux, the form of $F$ from (2.17) can be used, alongside (5.3), to give the explicit expression for $\theta_b$, namely

$$\theta_b(t) = 1 - \frac{\mathcal{F}(k_0)}{\mathcal{V}(k_0)}t = 1 - \frac{8\left(2\log k_0 + 1 - k_0^2\right)}{\pi\left(1 - k_0^2 + (1+k_0^2)\log k_0\right)}t, \tag{5.8}$$

from which we can determine the evolution of $h(r,t)$, $\theta_a(t)$ and $V(t)$ from (3.10), (3.14), and (3.18),

$$h(r,t) = \frac{(1-r^2)\log k_0 - (1-k_0^2)\log r}{2\log k_0 + 1 - k_0^2}\left(1 - \frac{8\left(2\log k_0 + 1 - k_0^2\right)}{\pi\left(1 - k_0^2 + (1+k_0^2)\log k_0\right)}t\right), \quad (5.9)$$

$$\theta_a(t) = \frac{2k_0^2\log k_0 + 1 - k_0^2}{k_0\left(k_0^2 - 1 - 2\log k_0\right)}\left(1 - \frac{8\left(2\log k_0 + 1 - k_0^2\right)}{\pi\left(1 - k_0^2 + (1+k_0^2)\log k_0\right)}t\right), \quad (5.10)$$

$$V(t) = 4(1-k_0^2)t + \frac{\pi\left(1-k_0^2\right)\left[(1+k_0^2)\log k_0 + 1 - k_0^2\right]}{2\log k_0 + 1 - k_0^2}. \quad (5.11)$$

The lifetime of the droplet, defined on (5.7), is given by

$$t_{\text{lifetime}} = \frac{\mathcal{V}(k_0)}{\mathcal{F}(k_0)} = \frac{\pi\left(1-k_0^2 + (1+k_0^2)\log k_0\right)}{8\left(2\log k_0 + 1 - k_0^2\right)}. \quad (5.12)$$

Figure 5.1 shows the evolution of an annular droplet with a spatially-uniform evaporative flux evaporating in the pinned–pinned mode, in particular plots of (a) $\theta_a(t)$, (b) $\theta_b(t)$ and (c) $V(t)$, plotted as functions of $t$ for $k_0 = 0.2, 0.4, 0.6, 0.8$, (d) $h(r)$ plotted as functions of $r$ at time intervals $t = t_{\text{lifetime}}/10$ for $k_0 = 0.2$, and (e) $t_{\text{lifetime}}$ plotted as a function of $k_0$, where arrows indicates the direction of increasing $t$.

### 5.1.2 Evolution of an annular droplet evaporating in the pinned–pinned mode with a diffusion-limited evaporative flux

In the case of a diffusion-limited evaporative flux, we use $\mathcal{F}_{\text{Cooke}}$ to determine the evolution of an annular droplet evaporating in pinned–pinned mode. A consequence of this is that all calculations in the diffusion-limited regime must be performed numerically.

Figure 5.1: Evolution of an annular droplet with a spatially-uniform evaporative flux evaporating in the pinned–pinned mode. (a) A plot of $\theta_b(t)$, given by (5.8), (b) a plot of $\theta_a(t)$, given by (5.10), (c) a plot of $V$, given by (5.11), plotted as a function of time, where arrows indicate direction of increasing $k_0 = 0.2, 0.4, 0.6, 0.8$, (d) a plot of $h(r)$, given by (5.9), with $k_0 = 0.2$ at time intervals of $t = t_{\text{lifetime}}/10$, where arrows indicate direction of increasing time, (e) a plot of $t_{\text{lifetime}}$ plotted as a function of $k_0$.

The asymptotic solutions for $\mathcal{F}$ in the limits $k \to 0^+$ and $k \to 1^-$, given by (4.15) and (4.17), respectively, can be used to determine the behaviour of the lifetime in each limit. In the limit $k_0 \to 0^+$, $t_{\text{lifetime}}$ given by (5.7) approaches

$$t_{\text{lifetime}} = \frac{\pi(1 + \log k_0)}{8(1 + 2\log k_0)} - \frac{\pi\,(1 + 3\log k_0)}{8\,(1 + 2\log k_0)^2}k_0^2 + O\left(\frac{k_0^3(1 + \log k_0)}{(1 + 2\log k_0)}\right) \to \frac{\pi}{16}^-, \quad (5.13)$$

which tends to $\pi/16$ as $k_0 \to 0^+$, the value for a spherical-cap droplet evaporating with a pinned contact line (i.e. in the CR mode). Similarly, in the limit $k_0 \to 1^-$, $t_{\text{lifetime}}$ given by (5.7) approaches

$$t_{\text{lifetime}} = \frac{1}{6\pi} \log\left(\frac{32}{1 - k_0}\right)(1 - k_0)^2 + O\left((1 - k_0)^3 \left[3 - \log\left(\frac{32}{1 - k_0}\right)\right]\right) \to 0^+.$$

$$(5.14)$$

Figure 5.2 shows the evolution of an annular droplet with a diffusion-limited evaporative flux evaporating in the pinned–pinned mode, calculated with $\mathcal{F}_{\text{Cooke}}$. In particular, plots of (a) $\theta_b(t)$, (b) $\theta_a(t)$ and (c) $V(t)$, plotted as functions of $t$ for $k_0 = 0.2, 0.4, 0.6, 0.8$ where arrows indicates the direction of increasing $t$, (d) $h(r)$ plotted as functions of $r$ at time intervals $t = t_{\text{lifetime}}/10$ for $k_0 = 0.2$, where the arrow indicates direction of increasing $t$, and (e) $t_{\text{lifetime}}$ plotted as a function of $k_0$, where dashed lines show the asymptotic results given by (5.13) and (5.14).

## 5.2 Evolution and lifetime of an annular droplet evaporating in the free–pinned mode

In this case $\theta_a \equiv \theta_{a0}$ and $b \equiv b_0 \equiv 1$ so that $k = a(t)/b_0 = a(t)$ throughout. As a consequence of the scalings used in (2.7), $b = b_0 = 1$. From (25), the initial value

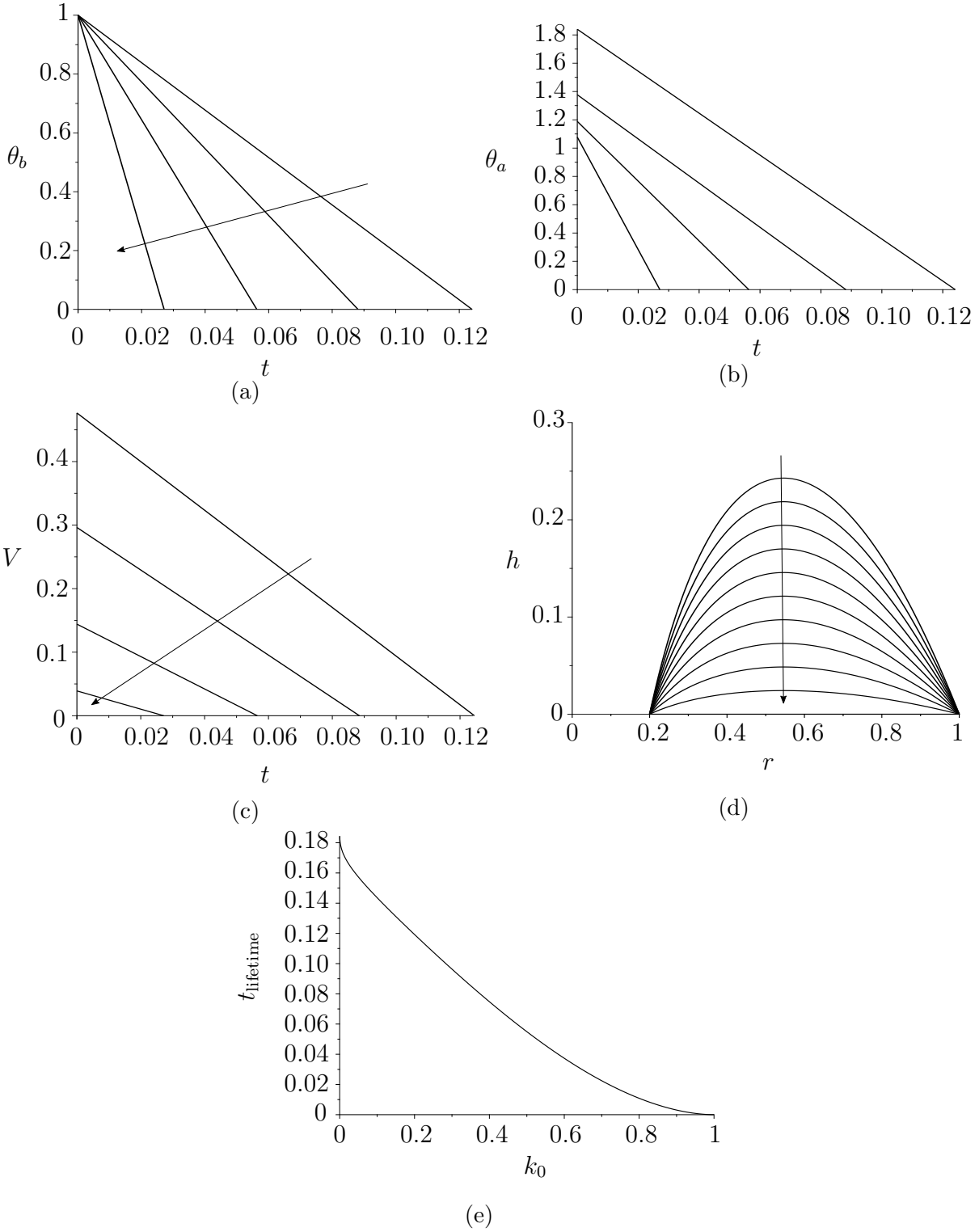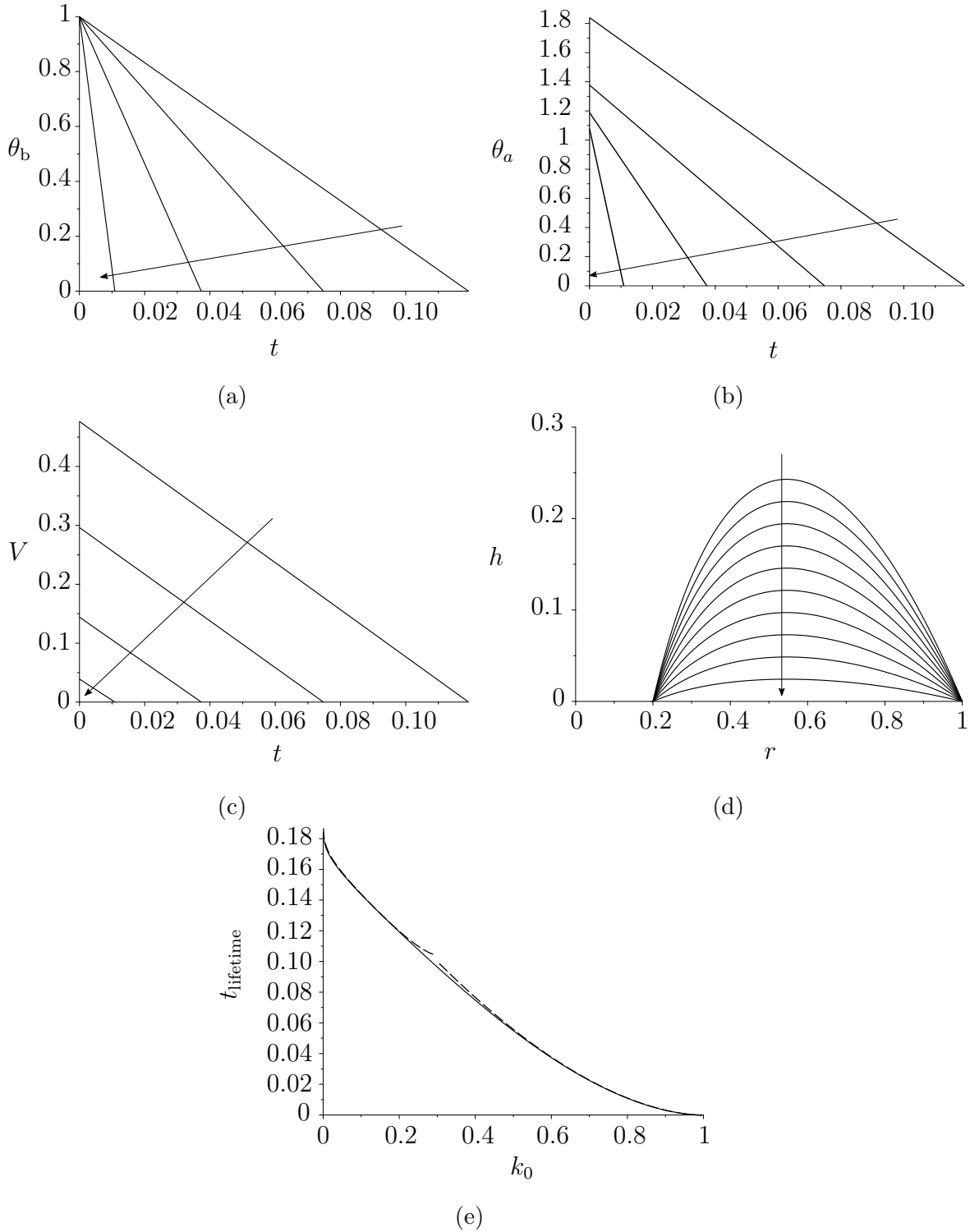Figure 5.2: Evolution of a droplet with a diffusion-limited evaporative flux evaporating in the pinned–pinned mode. (a) A plot of $\theta_b(t)$, given by (5.3), (b) a plot of $\theta_a(t)$, given by (5.5), (c) a plot of $V(t)$, given by (5.6), plotted as a function of time, where arrows indicate direction of increasing $k_0 = 0.2, 0.4, 0.6, 0.8$, (d) a plot of $h(r, t)$, given by (5.4), with $k_0 = 0.2$ at time intervals $t = t_{\text{lifetime}}/10$, where arrows indicate direction of increasing time, (e) a plot of $t_{\text{lifetime}}$ plotted as a function of $k_0$, where dashed lines represent the asymptotic solution for $t_{\text{lifetime}}$ in the limit $k_0 \to 0^+$ and $k_0 \to 1^-$.

48

$\theta_{a0}$ is

$$\theta_{a0} = \mathcal{T}(k_0), \qquad (5.15)$$

and the outer contact angle $\theta_b$ is

$$\theta_b = \frac{\theta_{a0}}{\mathcal{T}(k)} = \frac{\mathcal{T}(k_0)}{\mathcal{T}(k)}. \qquad (5.16)$$

The evolution of the droplet is then determined from (13)

$$-\frac{\mathrm{d}V}{\mathrm{d}t} = -\mathcal{T}(k_0)\frac{\mathrm{d}}{\mathrm{d}k}\left(\frac{\mathcal{V}(k)}{\mathcal{T}(k)}\right)\frac{\mathrm{d}k}{\mathrm{d}t} = \mathcal{F}(k). \qquad (5.17)$$

Then (5.17) gives

$$\frac{\mathrm{d}k}{\mathrm{d}t} = -\frac{\mathcal{F}}{\mathcal{T}(k_0)}\left[\frac{\mathrm{d}}{\mathrm{d}k}\left(\frac{\mathcal{V}(k)}{\mathcal{T}(k)}\right)\right]^{-1}, \qquad (5.18)$$

which can be solved implicitly to give an integral equation for $k(t)$.

$$t = -\mathcal{T}(k_0)\int_{k_0}^{k}\frac{1}{\mathcal{F}(\tilde{k})}\frac{\mathrm{d}}{\mathrm{d}\tilde{k}}\left(\frac{\mathcal{V}(\tilde{k})}{\mathcal{T}(\tilde{k})}\right)\mathrm{d}\tilde{k}. \qquad (5.19)$$

Then from (2.21) the expression for the lifetime of an annular drop evaporating in the free–pinned mode is

$$t_{\text{lifetime}} = -\mathcal{T}(k_0)\int_{k_0}^{1}\frac{1}{\mathcal{F}(k)}\frac{\mathrm{d}}{\mathrm{d}k}\left(\frac{\mathcal{V}(k)}{\mathcal{T}(k)}\right)\mathrm{d}k. \qquad (5.20)$$

### 5.2.1 Evolution of an annular droplet evaporating in the free–pinned mode with a spatially-uniform evaporative flux

Since the evolution of $k(t)$, and hence $t_{\mathrm{lifetime}}$, are expressed as an integral equation, no expressions in the free–pinned mode can be expressed explicitly. The evolution of $k(t)$, and hence $a(t)$, can be determined by numerically integrating (5.19), from which the evolution of $\theta_b(t)$, $h(r,t)$ and $V(t)$ may be determined. Figure 5.3 shows the evolution of a droplet with a uniform flux evaporating in the free–pinned mode, in particular the evolution of (a) $\theta_b(t)$, (b) $a(t)$, (c) $h(r)$, (d) $V$, and (e) $t_{\mathrm{lifetime}}$. Figure 5.3(a) shows that $\theta_b$ tends to $\theta_{a0}$ throughout the duration of the evaporation process.

### 5.2.2 Evolution of an annular droplet evaporating in the free–pinned mode with a diffusion-limited evaporative flux

The asymptotic behaviour of (5.20) in the limit $k_0 \to 0^+$ is

$$t_{\mathrm{lifetime}} \sim \frac{1}{2\log k_0 + 1} k_0^{-1} \int_{k_0}^{1} \frac{1}{\mathcal{F}(k)} \frac{\mathrm{d}}{\mathrm{d}k}\left(\frac{\mathcal{V}(k)}{\mathcal{T}(k)}\right)\,\mathrm{d}k. \qquad (5.21)$$

Similarly, the asymptotic behaviour of (5.20) in the limit $k_0 \to 1^-$ is

$$t_{\mathrm{lifetime}} \sim \left(1 + \frac{1-k_0}{3}\right)\int_{k_0}^{1} \frac{\log\left(\frac{32k}{1-k}\right)(k-1)}{3\pi}\,\mathrm{d}k. \qquad (5.22)$$

The evolution of $k(t)$ and hence $a(t)$ can be found by numerically integrating (5.19). Then $\theta_b(t)$, $h(r,t)$ and $V(t)$ can be found. Figure 5.4 shows the evolution

Figure 5.3: Evolution of a droplet with a spatially-uniform evaporative flux evaporating in the free–pinned mode. (a) A plot of $a(t)$, (b) a plot of $\theta_b(t)$, (c) a plot of $V(t)$, plotted as a function of time, where arrows indicate direction of increasing $k_0 = 0.2, 0.4, 0.6, 0.8$, (d) a plot of $h(r,t)$, with $k_0 = 0.2$ at time intervals $t = t_{\text{lifetime}}/10$, where arrows indicate direction of increasing time, (e) a plot of $t_{\text{lifetime}}$ plotted as a function of $k_0$.

51

of a droplet with a diffusion-limited flux evaporating in the free–pinned mode with $\mathcal{F}_{\text{Cooke}}$, in particular the evolution of (a) $a(t)$, (b) $b(t)$, (c) $h(r,t)$, (d) $V(t)$, and (e) $t_{\text{lifetime}}$, where dashed lines show the asymptotic results given by (5.21) and (5.22).

## 5.3 Evolution and lifetime of an annular droplet evaporating in the pinned–free mode

In this case $\theta_b \equiv \theta_{b0}$ and $a \equiv a_0$ so that $k(t) = a_0/b(t)$ throughout. As a consequence of the scalings used in (2.7), $\theta_b \equiv \theta_{b0} \equiv 1$. The evolution of the droplet is determined by (2.20)

$$-\frac{\mathrm{d}V}{\mathrm{d}t} = b(t)^2 \frac{\mathrm{d}b}{\mathrm{d}t} \left(k\mathcal{V}'(k) - 3\mathcal{V}(k)\right) = b(t)\mathcal{F}(k), \tag{5.23}$$

so

$$b\frac{\mathrm{d}b}{\mathrm{d}t} = \frac{\mathcal{F}(k)}{k\mathcal{V}'(k) - 3\mathcal{V}(k)}. \tag{5.24}$$

As in the free–pinned case, from (5.24) we can obtain an implicit solution for $k(t)$,

$$t = k_0^2 \int_{k_0}^{k(t)} \frac{3\mathcal{V}(\tilde{k}) - k\mathcal{V}'(\tilde{k})}{\tilde{k}^3 \mathcal{F}(\tilde{k})} \, \mathrm{d}\tilde{k}. \tag{5.25}$$

The evolution of $k(t)$ can be found by solving (5.25) numerically.

From (2.21), the expression for the lifetime of an annular drop evaporating in the pinned–free mode is

$$t_{\text{lifetime}} = k_0^2 \int_{k_0}^1 \frac{1}{k^3 \mathcal{F}(k)} \left[3\mathcal{V}(k) - k\mathcal{V}'(k)\right] \mathrm{d}k. \tag{5.26}$$
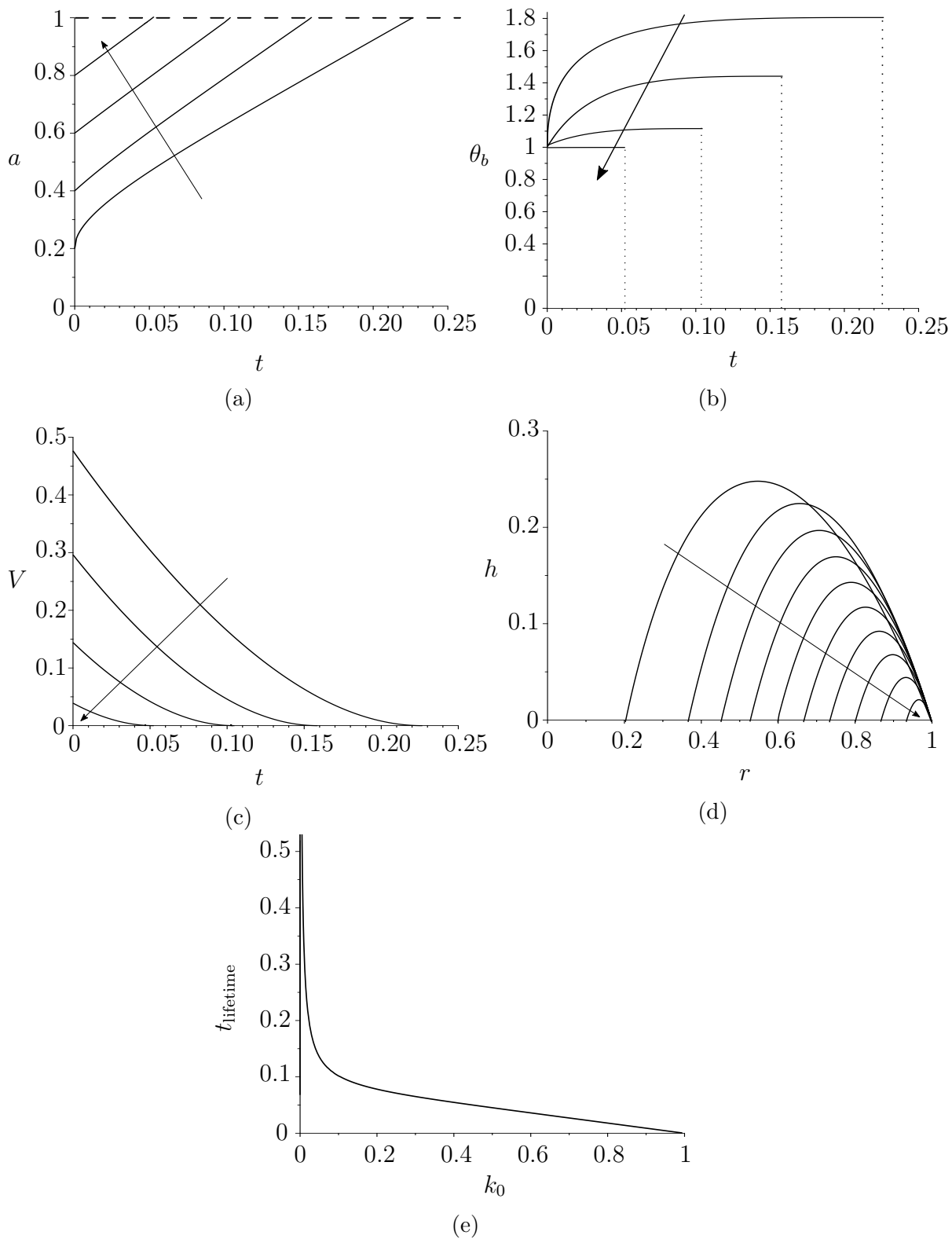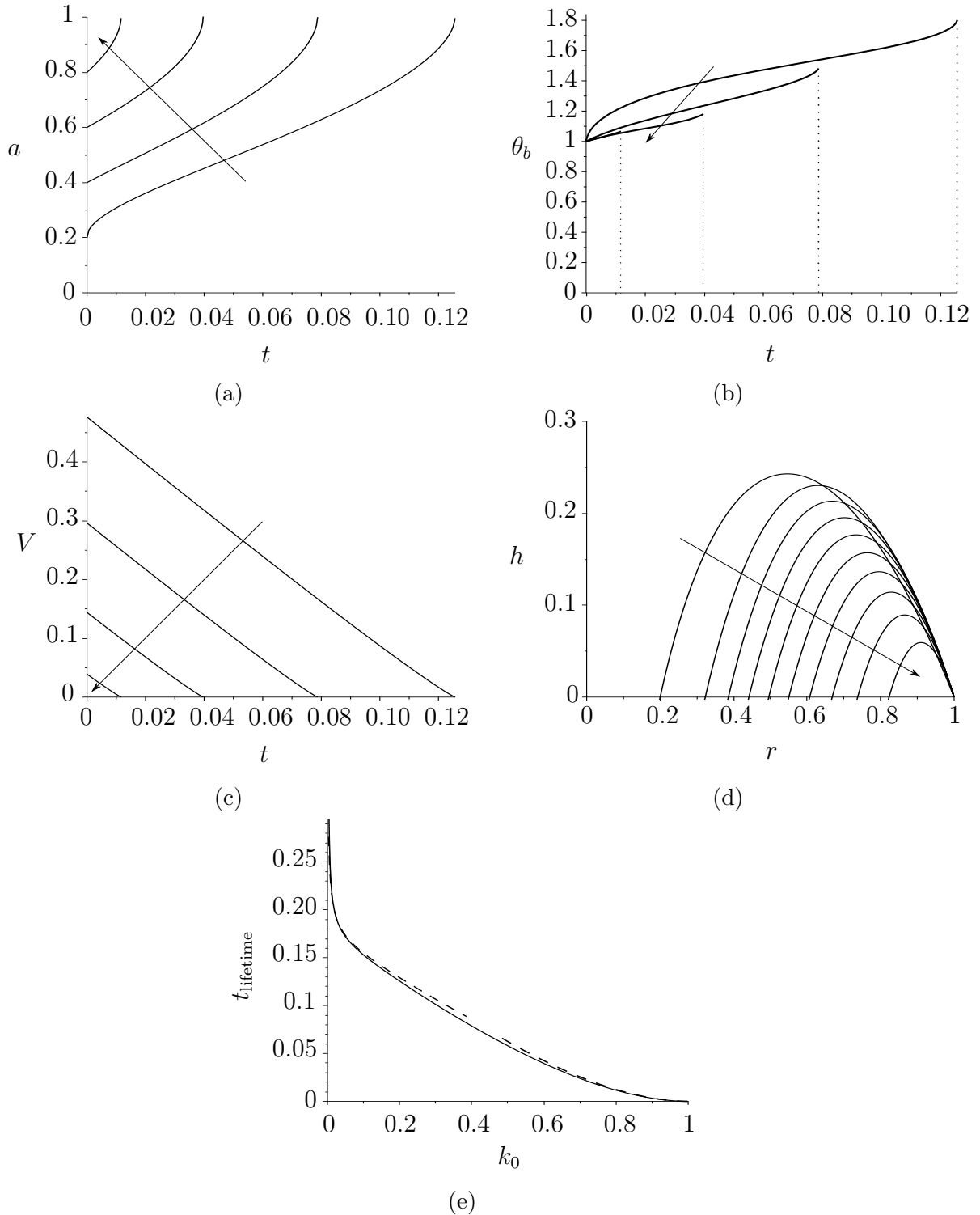
Figure 5.4: Evolution of a droplet with a diffusion-limited flux evaporating in the free–pinned mode. (a) A plot of $a(t)$, (b) a plot of $\theta_b(t)$, (c) a plot of $V(t)$, plotted as a function of time, where arrows indicate direction of increasing $k_0 = 0.2, 0.4, 0.6, 0.8$, (d) a plot of $h(r, t)$, with $k_0 = 0.2$ at time intervals $t = t_{\text{lifetime}}/10$, where arrows indicate direction of increasing time, (e) a plot of $t_{\text{lifetime}}$ plotted as a function of $k_0$, where the dashed lines denote the asymptotic solutions in the limit $k_0 \to 0^+$ and $k_0 \to 1^-$.

### 5.3.1 Evolution of an annular droplet evaporating in the pinned–free mode with a spatially-uniform evaporative flux

The evolution of $k(t)$ and hence $b(t)$ can be determined by numerically integrating (5.25), with which the evolution of $\theta_a(t)$, $h(r,t)$ and $V(t)$ are found. Figure 5.5 shows the evolution of a droplet with a spatially-uniform evaporative flux evaporating in the pinned–free mode, in particular the evolution of (a) $\theta_a(t)$, (b) $b(t)$, (c) $h(r,t)$, (d) $V(t)$, and (e) $t_{\text{lifetime}}$. Figure 5.5(a) shows that $\theta_a$ will tend to $\theta_{b0} = 1$, similar to the free–pinned case.

### 5.3.2 Evolution of an annular droplet evaporating in the pinned–free mode with a diffusion-limited evaporative flux

The asymptotic behaviour of (5.26) in the limit $k_0 \to 0^+$ is

$$t_{\text{lifetime}} \sim \frac{k_0^2 \pi}{8} \int_{k_0}^{1} \frac{1}{k^3 \mathcal{F}(k)} \left[ 3\mathcal{V}(k) - k\mathcal{V}'(k) \right] \, \mathrm{d}k. \tag{5.27}$$

Similarly, the asymptotic behaviour of (5.26) in the limit $k_0 \to 1^-$ is

$$t_{\text{lifetime}} \sim \frac{1}{3\pi} \int_{k_0}^{1} \log\left( \frac{32}{1-k} \right) (k-1) \, \mathrm{d}k. \tag{5.28}$$

Figure 5.6 shows the evolution of a droplet with a diffusion-limited evaporative flux evaporating in the pinned–free mode with $\mathcal{F}_{\text{Cooke}}$. In particular, plots of (a) $a(t)$, (b) $b(t)$, (c) $h(r,t)$, (d) $V(t)$, and (e) $t_{\text{lifetime}}$, where dashed lines show the asymptotic results given by (5.27) and (5.28).

54
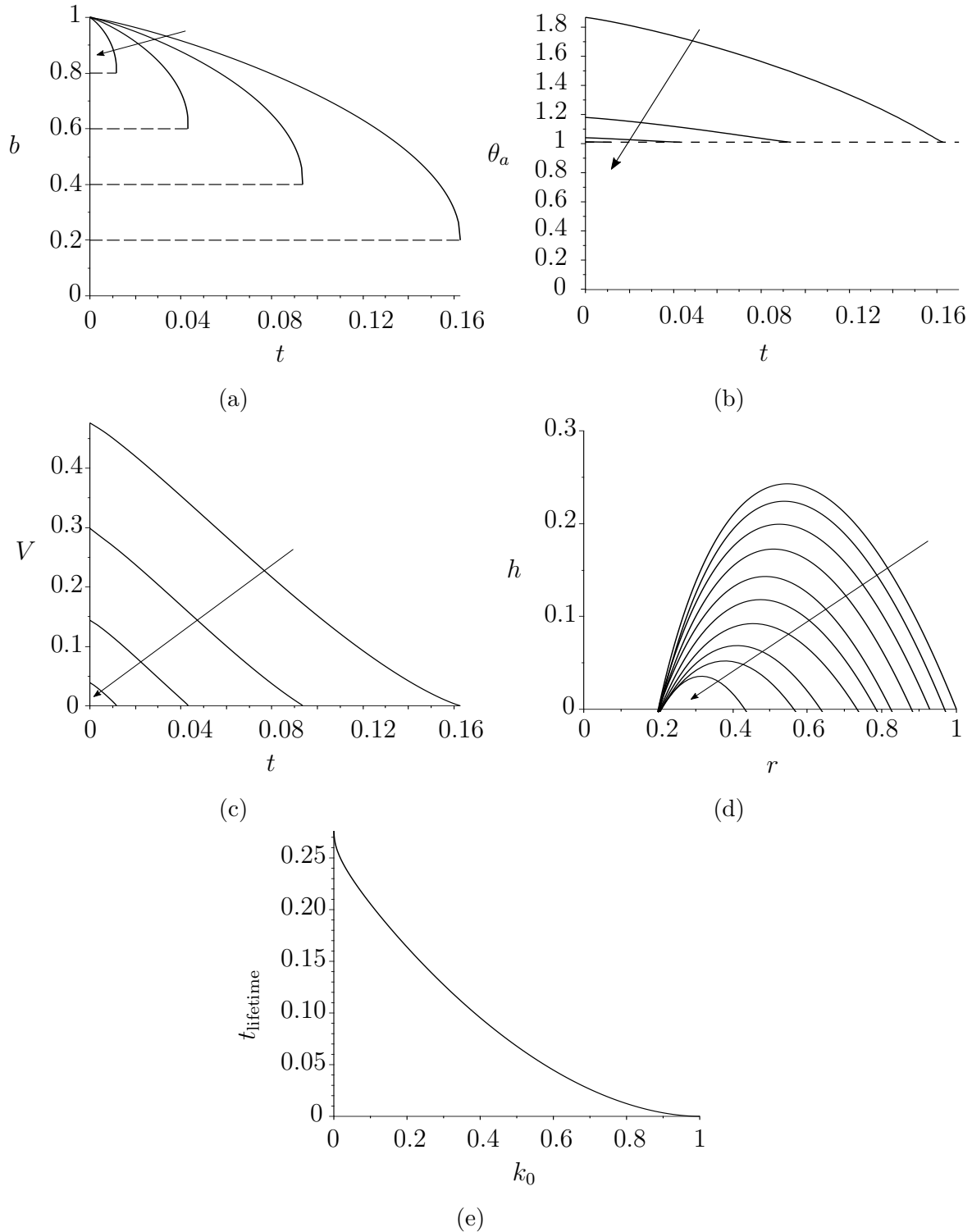
Figure 5.5: Evolution of a droplet with a spatially-uniform evaporative flux evaporating in the pinned–free mode. A plot of (a) $b(t)$, (b) $\theta_a(t)$, (c) $V(t)$, plotted as a function of time, where arrows indicate direction of increasing $k_0 = 0.2, 0.4, 0.6, 0.8$, (d) $h(r,t)$, with $k_0 = 0.2$ at time intervals $t = t_{\text{lifetime}}/10$, where arrows indicate direction of increasing time, (e) $t_{\text{lifetime}}$ plotted as a function of $k_0$. The dashed lines in (a) and (b) show the final values of $b$ and $\theta_a$, respectively.
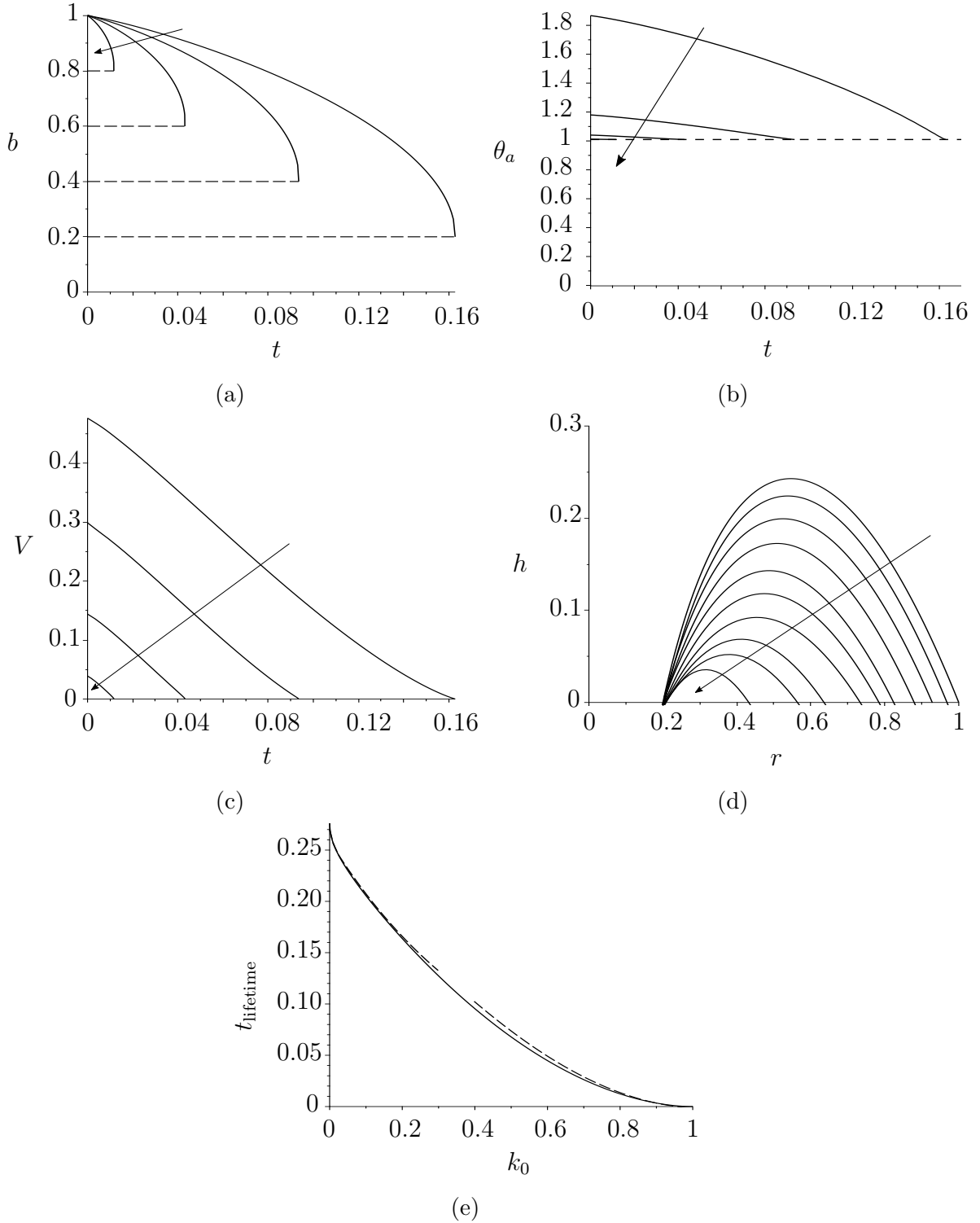
Figure 5.6: Evolution of a droplet with a diffusion-limited evaporative flux evaporating in the pinned–free mode. A plot of (a) $b(t)$, (b) $\theta_a(t)$, (c) $V(t)$, plotted as a function of time, where arrows indicate direction of increasing $k_0 = 0.2, 0.4, 0.6, 0.8$, (d) $h(r, t)$, with $k_0 = 0.2$ at time intervals $t = t_{\text{lifetime}}/10$, where arrows indicate direction of increasing time, (e) $t_{\text{lifetime}}$ plotted as a function of $k_0$, where dashed lines represent the asymptotic solution for $t_{\text{lifetime}}$ in the limit $k_0 \to 0^+$ and $k_0 \to 1^-$. The dashed lines in (a) and (b) show the final values of $b$ and $\theta_a$, respectively.

## 5.4 Evolution and lifetime of an annular droplet evaporating in the free–free mode

In this case $\theta_b \equiv \theta_{b0}$ and $\theta_a \equiv \theta_{a0}$. As a consequence of the scalings used in (2.7), $\theta_b = \theta_{b0} = 1$. Then from (3.14), $k$ must be constant throughout, and so $k \equiv k_0 = a_0/b_0 = a_0$. The evolution of the droplet is determined from (2.20)

$$\frac{\mathrm{d}V}{\mathrm{d}t} = \frac{\mathrm{d}}{\mathrm{d}t}\left(b^3 \mathcal{V}(k_0)\right) = 3\mathcal{V}(k_0)b^2\frac{\mathrm{d}b}{\mathrm{d}t} = b\mathcal{F}(k_0). \tag{5.29}$$

Then (5.29) gives

$$b\frac{\mathrm{d}b}{\mathrm{d}t} = -\frac{\mathcal{F}(k_0)}{3\mathcal{V}(k_0)}. \tag{5.30}$$

Since $k_0$ is a constant, (5.30) can be integrated to obtain

$$b(t) = \left(1 - \frac{2t\mathcal{F}(k_0)}{3\mathcal{V}(k_0)}\right)^{\frac{1}{2}}. \tag{5.31}$$

By using $k_0 = a(t)/b(t)$, $a(t)$, $h(r,t)$, and $V(t)$ are then

$$a(t) = k_0 b(t) = k_0\left(1 - \frac{2t\mathcal{F}(k_0)}{3\mathcal{V}(k_0)}\right)^{\frac{3}{2}}, \tag{5.32}$$

$$h(r,t) = \frac{b(t)\left(\left(1 - \frac{r^2}{b(t)^2}\right)\log k_0 - (1 - k_0^2)\log\left(\frac{r}{b(t)}\right)\right)}{2\log k_0 + 1 - k_0^2}, \tag{5.33}$$

$$V(t) = \left(1 - \frac{2\mathcal{F}(k_0)t}{3\mathcal{V}(k_0)}\right)^{\frac{3}{2}}\mathcal{V}(k_0). \tag{5.34}$$

From (2.21) the expression for the lifetime of an annular drop evaporating in the free–free mode is

$$t_{\text{lifetime}} = \frac{3\mathcal{V}(k_0)}{2\mathcal{F}(k_0)} = \frac{3\pi(1 - k_0^2)((k_0^2 + 1)\log k_0 + 1 - k_0^2)}{4(2\log k_0 + 1 - k_0^2)\mathcal{F}(k_0)}. \tag{5.35}$$

### 5.4.1 Evolution of an annular droplet evaporating in the free–free mode with a spatially-uniform evaporative flux

Using (2.18), we can obtain explicit expressions for $b(t)$

$$b(t) = \left(1 - \frac{16t \left(2\log k_0 + 1 - k_0^2\right)}{3\pi \left((1 + k_0^2)\log k_0 + 1 - k_0^2\right)}\right)^{\frac{1}{2}}, \tag{5.36}$$

and hence $a(t)$, $h(r,t)$, and $V(t)$ are

$$a(t) = k_0 \left(1 - \frac{16t \left(2\log k_0 + 1 - k_0^2\right)}{3\pi \left((1 + k_0^2)\log k_0 + 1 - k_0^2\right)}\right)^{\frac{1}{2}}, \tag{5.37}$$

$$h(r) = \frac{b(t)\left(\left(1 - \frac{r^2}{b(t)^2}\right)\log k_0 - (1 - k_0^2)\log\left(\frac{r}{b(t)}\right)\right)}{2\log k_0 + 1 - k_0^2}, \tag{5.38}$$

$$V(t) = \left(1 - \frac{16t \left(2\log k_0 + 1 - k_0^2\right)}{3\pi \left((1 + k_0^2)\log k_0 + 1 - k_0^2\right)}\right)^{\frac{3}{2}} \frac{\pi \left(1 - k_0^2\right)\left[(1 + k_0^2)\log k_0 + 1 - k_0^2\right]}{2\left[2\log k_0 + 1 - k_0^2\right]}. \tag{5.39}$$

Figure 5.7 shows the evolution of a droplet with a spatially-uniform evaporative flux evaporating in the free–free mode, in particular, the evolution of (a) $a(t)$, (b) $b(t)$, (c) $h(r,t)$, (d) $V(t)$, and (e) $t_{\text{lifetime}}$.

Figure 5.7: Evolution of a droplet with a spatially-uniform evaporative flux evaporating in the free–free mode. (a) A plot of $a(t)$ given by (5.32), (b) a plot of $b(t)$ given by (5.31), (c) a plot of $V(t)$ given by (5.34), plotted as a function of time, where arrows indicate direction of increasing $k_0 = 0.2, 0.4, 0.6, 0.8$, (d) a plot of $h(r, t)$ given by (5.33), with $k_0 = 0.2$ at time intervals $t = t_{\text{lifetime}}/10$, where arrows indicate direction of increasing time, (e) a plot of $t_{\text{lifetime}}$ given by (5.35) plotted as a function of $k_0$.

### 5.4.2 Evolution of an annular droplet evaporating in the free–free mode with a diffusion-limited evaporative flux

The asymptotic behaviour of (5.35) in the limit $k_0 \to 0^+$ is

$$t_{\text{lifetime}} = \frac{3\pi(1 + \log k_0)}{16(2\log k_0 + 1)} + O\left(\frac{k_0^2(1 + 3\log k_0)}{1 + 2\log k_0}\right) \to \frac{3\pi}{32}^-, \qquad (5.40)$$

which gives the solutions for a spherical-cap droplet evaporating with a constant contact angle (i.e. in the CA mode). Similarly, the asymptotic behaviour of (5.35) in the limit $k_0 \to 1^-$ is

$$t_{\text{lifetime}} = \frac{\log\left(\frac{32}{1-k_0}\right)}{4\pi}(1 - k_0)^2 + O\left((1 - k_0)^3\left(3 - \log\left(\frac{32}{1 - k_0}\right)\right)\right) \to 0^+. \quad (5.41)$$

Figure 5.8 shows the evolution of a droplet with a diffusion-limited evaporative flux evaporating in the free–free mode with $\mathcal{F}_{\text{Cooke}}$, in particular the evolution of (a) $a(t)$, (b) $b(t)$, (c) $h(r,t)$, (d) $V(t)$, and (e) $t_{\text{lifetime}}$, where dashed lines show the asymptotic results given by (5.40) and (5.41).

## 5.5 Comparison between diffusion-limited and spatially-uniform evaporative fluxes

Figure 5.9(a) shows a plot of the lifetimes of an annular droplet in all four modes of evaporation for the spatially-uniform evaporative flux plotted as functions of $k_0$. Figure 5.9(b) shows a plot of the lifetimes of an annular droplet in all four modes of evaporation with the diffusion-limited evaporative flux plotted as functions of $k_0$.
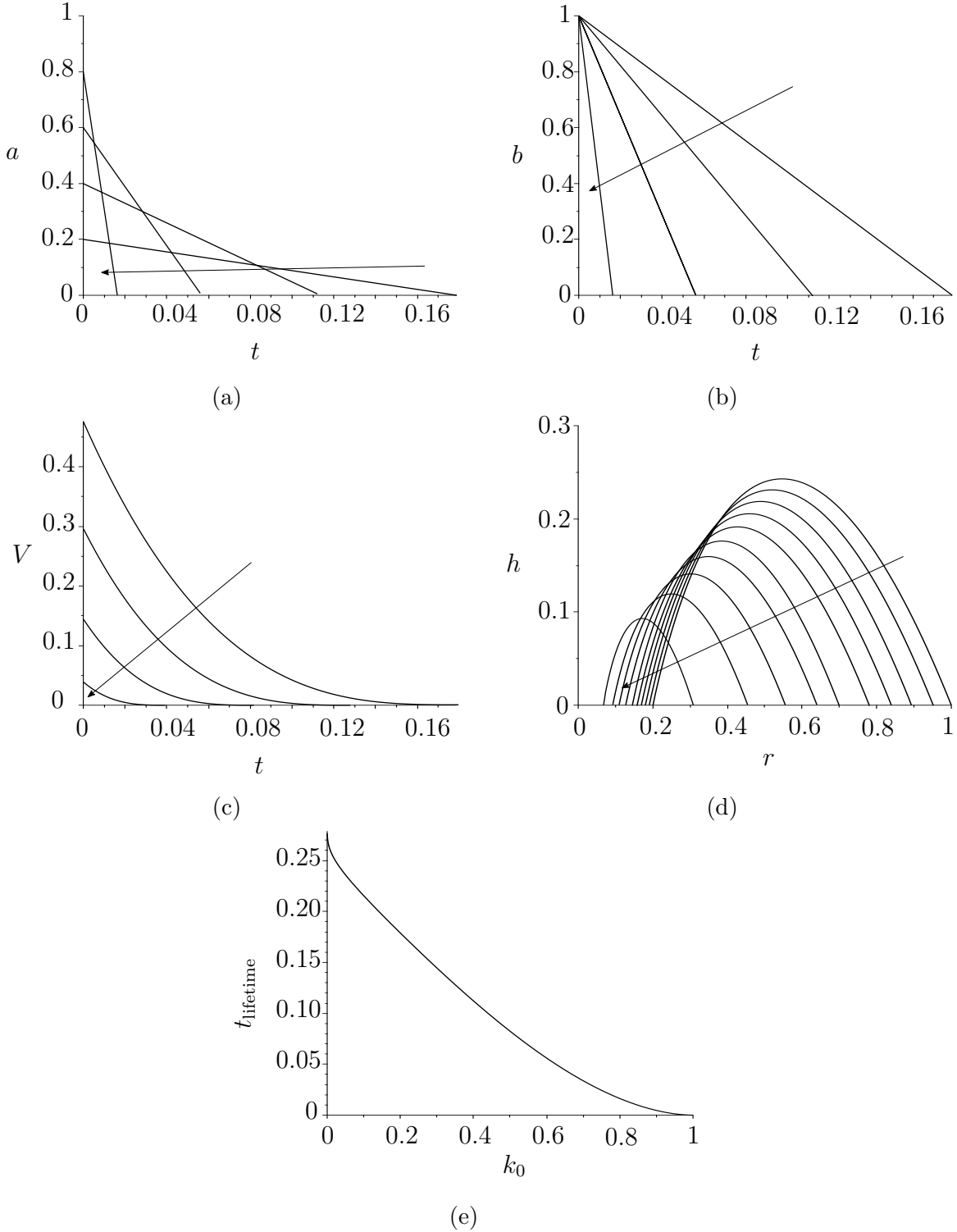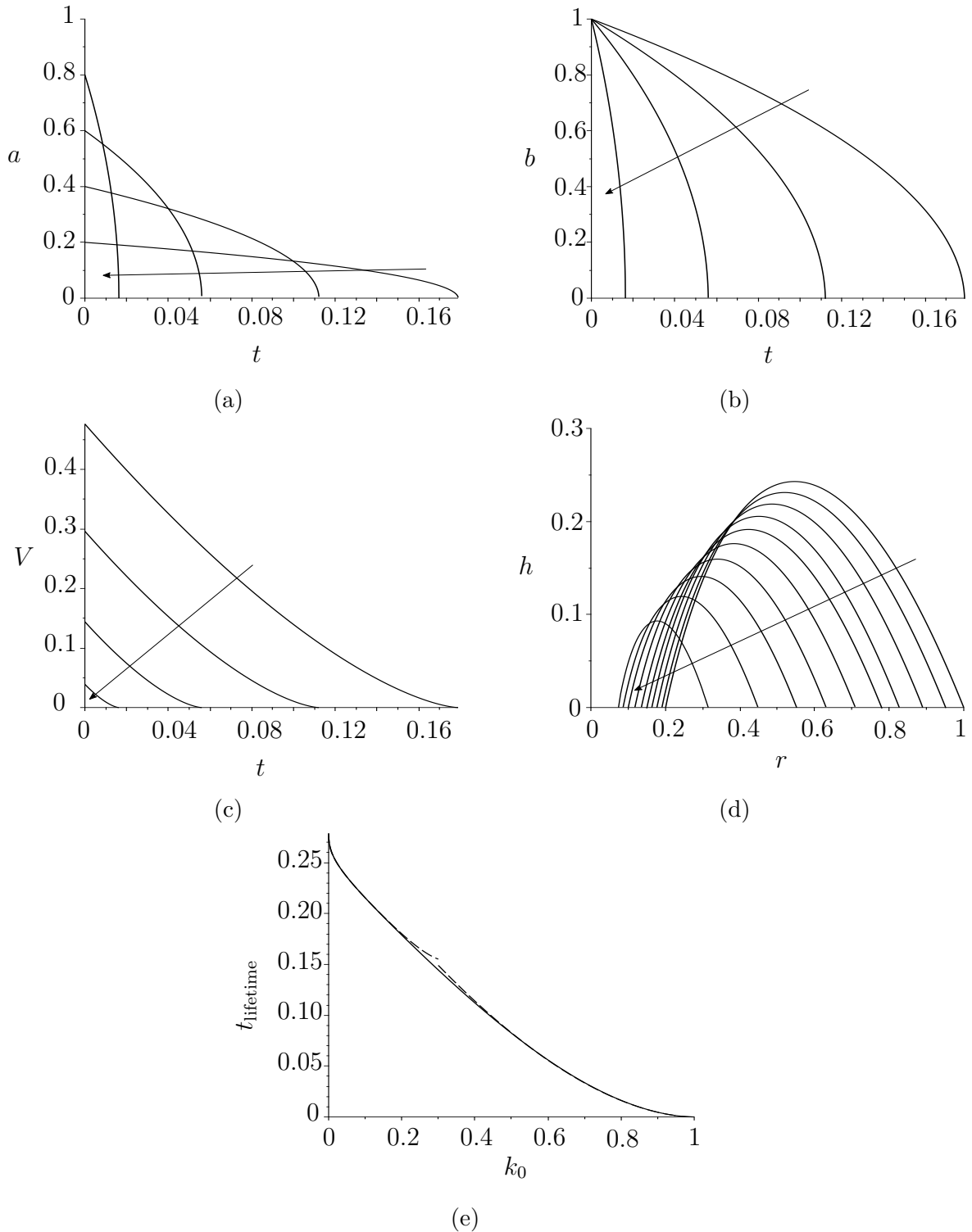
Figure 5.8: Evolution of a droplet with a diffusion-limited evaporative flux evapo-
rating in the free–free mode. (a) A plot of $a(t)$ given by (5.32), (b) a plot of $b(t)$
given by (5.31), (c) a plot of $V(t)$ given by (5.34), plotted as a function of time,
where arrows indicate direction of increasing $k_0 = 0.2, 0.4, 0.6, 0.8$, (d) a plot of
$h(r,t)$ given by (5.33), with $k_0 = 0.2$ at time intervals $t = t_{\text{lifetime}}/10$, where arrows
indicate direction of increasing time, (e) a plot of $t_{\text{lifetime}}$ given by (5.35) plotted as
a function of $k_0$, where dashed lines represent the asymptotic solution for $t_{\text{lifetime}}$ in
the limit $k_0 \to 0^+$ and $k_0 \to 1^-$.

61

Figure 5.9: Plot of the lifetimes of an annular droplet in all four modes of evapora-
tion, plotted as functions of $k_0$ for (a) a spatially-uniform evaporative flux given by
(2.16), and (b) the diffusion-limited evaporative flux given by (4.13). Pinned–pinned
mode is shown with a solid line, free–pinned mode with a dashed line, pinned–free
mode with a dash-dot line and free–free mode with a dotted line

For the spatially-uniform evaporative flux, shown in Figure 5.9(a), annular drop-
lets evaporating in the pinned–free mode and the free–free mode tend to the same
lifetime in the limit $k \to 0^-$, while in free–pinned mode, $t_{\text{lifetime}} \to \infty$ as $\theta_{a0} \to \infty$
in the limit $k \to 0^+$.

For the diffusion-limited evaporative flux, shown in Figure 5.9(b), in the limit
$k \to 0^+$, the lifetime of a droplet evaporating in the pinned–pinned mode tends to
$\pi/16$, the lifetime for a spherical-cap droplet evaporating in the CR mode. In both
cases where the outer contact line is not pinned (i.e. pinned–free and free–free mode)
the lifetime tends to $3\pi/32$, the lifetime for a spherical-cap droplet evaporating in
the CA mode. The lifetime of a droplet evaporating in the free–pinned mode does
not tend to the lifetime of a spherical-cap droplet evaporating in one of the extreme
modes of evaporation.

The modes of evaporation in which the lifetimes coincide for both the diffusion-
limited flux and the spatially-uniform flux in the limit $k \to 0^+$, namely the pinned–

pinned and the free–free mode, are the two modes in which $k \equiv k_0$ throughout the lifetime of the droplet. This is due to the fact that $\mathcal{F}_{\mathrm{U}}$ was chosen such that $\mathcal{F}_{\mathrm{DL}} = \mathcal{F}_{\mathrm{U}}$ in that limit.

The modes of evaporation in which the lifetimes do not coincide for both the diffusion-limited and spatially-uniform evaporative fluxes, namely the free–pinned and the pinned–free modes, are modes in which $k \equiv k(t)$ and hence the total evaporative fluxes change throughout the lifetime of the droplet.

In the limit $k \to 0^+$, the pinned–pinned mode reduces to the CR mode of a spherical-cap droplet (in which the outer contact line is pinned and the outer contact angle varies with time), and so in this limit the lifetime reduces to that of the CR mode. Similarly the pinned–free and free–free modes reduce to the CA mode of a spherical-cap droplet (in which the outer contact line varies with time and the outer contact angle is constant) and so in this limit the lifetime reduces to that of the CA mode. The free–pinned mode is the only mode which does not reduce to either the CA or the CR mode of a spherical-cap droplet in the limit $k \to 0^+$. The inner contact angle is fixed in the free–pinned mode, and is determined by $\theta_{a0} = \mathcal{T}(k_0)$ (3.14). Noting that $\mathcal{T}(k_0)$ is singular in the limit $k \to 0^+$, the factor of $\mathcal{T}(k_0)$ in the expression for the lifetime in the free–pinned mode (5.19) causes the lifetime to be singular in this limit. This directly contrasts with the free–free mode in which the inner contact angle is finite.

In practice, diffusion-limited evaporation is more common than spatially-uniform evaporation. As mentioned in Chapter 1.1, spatially-uniform evaporation only occurs for rather specialised conditions, such as a droplet evaporating on a hydrogel (see, for example, Okuzono *et al.* [61]), or the evaporation of a hemispherical droplet (see, for example, Stauber *et al.* [74]). In contrast, diffusion-limited evaporation is

controlled by the diffusion of vapour into the atmosphere, and has been observed in a wide range of real-world situations, as discussed in Chapter 1.

# Chapter 6

# Deposition

We now consider a particle-laden annular droplet. We assume that the suspended particles are passive (see, for example, Boulogne *et al.* [12]), so that they do not affect the flow within the droplet. The evaporation of the droplet induces a flow within it, which advects the particles suspended in the bulk of the droplet. In the following, we will find that the suspended particles are advected to the contact lines for both the diffusion-limited flux and the uniform flux.

In the case of a spherical-cap droplet with either a spatially-uniform or diffusion-limited evaporative flux, all of the mass of suspended particles are advected to the (single) contact line; in the case of an annular droplet, the mass of suspended particles is split, generally unequally, between the inner and outer contact lines. The suspended particles build up at the contact lines during the evaporation process, and at $t = t_{\mathrm{lifetime}}$, all of the mass of the suspended particles has been advected to the contact lines of the droplet.

We discuss the deposition in the case of the spatially-uniform evaporative flux (2.16) and the diffusion-limited evaporative flux (2.15). Specifically, we consider the

case in which the droplet is evaporating in the pinned–pinned mode, and so both contact lines are fixed and the ratio of the radii of the contact lines, $k$, takes the constant value $k_0 = a_0/b_0 = a_0$. As we have already seen, in the pinned–pinned mode, the evolution of $\theta_b(t)$ is given by (5.3), the evolution of $h(r, t)$, $V(t)$ and $\theta_a(t)$ are given by (5.4)–(5.5), and the lifetime of the droplet is given by (5.7).

In Chapter 6.1, we solve the hydrodynamic problem within the droplet, and determine the velocity $\mathbf{u} = (u, w)$ and depth-averaged radial velocity $\bar{u}$. In Chapter 6.2, we then solve the advection problem to derive the solution for the concentration of suspended particles $\phi(r, z, t)$ within the droplet. In Chapter 6.3, we use the solution for $\phi$ to derive an expression for the mass of suspended particles in the droplet $M$ and the masses of particles at the inner and outer contact lines, $M_a$ and $M_b$. In Chapter 6.4, we look at the deposition in the case of the spatially-uniform evaporative flux discussed in Chapter 2. In Chapter 6.5, we look at the deposition in the case of the diffusion-limited evaporative flux discussed in Chapter 2.

## 6.1 Solving the hydrodynamic problem within the droplet

The continuity equation is given by

$$\frac{1}{\hat{r}} \frac{\partial}{\partial \hat{r}} (\hat{r}\hat{u}) + \frac{\partial \hat{w}}{\partial \hat{z}} = 0. \tag{6.1}$$

By considering Stokes flow in a thin droplet the lubrication equation are

$$\hat{\mu} \frac{\partial^2 \hat{u}}{\partial \hat{z}^2} = \frac{\partial \hat{p}}{\partial \hat{r}} \tag{6.2}$$

and

$$\frac{\partial \hat{p}}{\partial \hat{z}} = 0, \tag{6.3}$$

where $\hat{\mu}$ is the constant viscosity. We scale and non-dimensionalise the variables according to (2.7) and (2.8).

To determine $u$, we first integrate (6.2) with respect to $z$,

$$\frac{\partial u}{\partial z} - \left.\frac{\partial u}{\partial z}\right|_{z=h} = \frac{\partial p}{\partial r}(z - h). \tag{6.4}$$

By imposing the tangential stress condition on the surface of the droplet,

$$\frac{\partial u}{\partial z} = 0 \quad \text{on} \quad z = h, \tag{6.5}$$

equation (6.4) gives

$$\frac{\partial u}{\partial z} = \frac{\partial p}{\partial r}(z - h). \tag{6.6}$$

Integrating (6.6) with respect to $z$ from $0$ to $h$ and imposing the no slip condition on the substrate, $u = 0$ on $z = 0$, yields

$$u = \frac{1}{2}\frac{\partial p}{\partial r}\left(z^2 - 2hz\right). \tag{6.7}$$

Define the radial flux $Q(r,t)$ as

$$Q = \int_0^h u \, \mathrm{d}z. \tag{6.8}$$

The depth-averaged radial velocity $\bar{u}(r,t)$ is then

$$\bar{u} = \frac{Q(r,t)}{h} = \frac{1}{h}\int_0^h u \; \mathrm{d}z = -\frac{h^2}{3}\frac{\partial p}{\partial r}. \tag{6.9}$$

Rearranging (6.9) gives

$$\frac{\partial p}{\partial r} = -\frac{3\bar{u}}{h^2}. \tag{6.10}$$

Substituting (6.10) into (6.7) yields

$$u = \frac{3Q}{2h^3}(2hz - z^2). \tag{6.11}$$

To find an explicit expression for $Q$, we first use the kinematic condition,

$$\frac{\partial h}{\partial t} + \frac{1}{r}\frac{\partial}{\partial r}(rQ) = -J. \tag{6.12}$$

Expressing $\partial h/\partial t$ in terms of $\mathrm{d}\theta_b/\mathrm{d}t$ yields,

$$\frac{\partial h}{\partial t} = \frac{\partial h}{\partial \theta_b}\frac{\mathrm{d}\theta_b}{\mathrm{d}t} = \mathcal{H}(r,k_0)\frac{\mathrm{d}\theta_b}{\mathrm{d}t}, \tag{6.13}$$

then by using (5.2) to write $\mathrm{d}\theta_b/\mathrm{d}t$ in terms of $\mathcal{V}$ and $\mathcal{F}$, (6.13) gives

$$\frac{\partial h}{\partial t} = -\frac{\mathcal{H}(r,k_0)\mathcal{F}(k_0)}{\mathcal{V}(k_0)}. \tag{6.14}$$

Substituting (6.14) into (6.12), multiplying through by $r$, and integrating from $r = k_0$ to $r$ gives

$$-\frac{\mathcal{F}(k_0)}{\mathcal{V}(k_0)}\int_{k_0}^r \mathcal{H}(\tilde{r},k_0)\tilde{r} \; \mathrm{d}\tilde{r} + rQ = -\int_{k_0}^r J\tilde{r} \; \mathrm{d}\tilde{r}, \tag{6.15}$$

which gives $Q(r, t)$ to be

$$Q(r, t) = \frac{1}{r\mathcal{V}(k_0)} \int_{k_0}^{r} [\mathcal{F}(k_0)\mathcal{H}(\tilde{r}, k_0) - \mathcal{V}(k_0)J(\tilde{r}, t)]\, \tilde{r}\, \mathrm{d}\tilde{r}, \qquad (6.16)$$

and so using the expression for $Q$ from (6.16), $\bar{u}(r, t)$ can be calculated from (6.9), giving

$$\bar{u}(r, t) = \frac{1}{r\theta_b(t)\mathcal{H}(r, k_0)\mathcal{V}(k_0)} \int_{k_0}^{r} [\mathcal{F}(k_0)\mathcal{H}(\tilde{r}, k_0) - \mathcal{V}(k_0)J(\tilde{r}, t)]\, \tilde{r}\, \mathrm{d}\tilde{r}. \qquad (6.17)$$

The sign of $\bar{u}$ determines whether the flow travels towards the inner or outer contact line: if $\bar{u}(r, t) < 0$, the flow within the droplet advects the suspended particles to the inner contact line, and if $\bar{u}(r, t) > 0$, the flow within the droplet advects the suspended particles to the outer contact line. If $\bar{u}(r, t) = 0$ for some value of $r$ in $0 < k < 1$, this would indicate that the sign of $\bar{u}$ changes within the domain, and hence the suspended particles would be advected to both the inner and outer contact lines.

## 6.2 Solving the advection problem for the concentration of suspended particles

We denote the concentration of the suspended particles as $\phi = \phi(r, z, t)$, where $\phi$ is nondimensionalised according to $\hat{\phi} = \hat{\phi}_0\phi$ and $\hat{\phi}_0$ denotes the initial value of $\hat{\phi}$. The Péclet number, $Pe$, is a dimensionless number which describes the ratio of the diffusion and advection timescales,

$$Pe = \frac{\text{diffusion timescale}}{\text{advection timescale}} = \frac{\hat{D}\,(\hat{c}_{\text{sat}} - \hat{c}_\infty)}{\hat{D}_p\hat{\rho}\hat{\theta}_{b0}} \quad \text{in the } r \text{ direction,} \qquad (6.18)$$

where $\hat{D}_p$ is the diffusivity of the suspended particles. For the present purposes, we are interested in the case where the effects of advection dominate in the $r$ direction (i.e. $Pe \gg 1$). However, as a result of the scales used for $r$ and $z$ (namely $\hat{r} = \hat{b}_0 r$ and $\hat{z} = \hat{b}_0 \hat{\theta}_{b0} z$), the diffusion timescales differ in the $r$ and $z$ direction by a factor of $\hat{\theta}_{b0}^2$. We therefore assume that $\hat{\theta}_{b0}^2 Pe$ satisfies $\hat{\theta}_{b0}^2 \ll \hat{\theta}_{b0}^2 Pe \ll 1$ (i.e. that $\hat{\theta}_{b0}^2 Pe$ is sufficiently small).

The governing equation for the leading-order concentration of particles $\phi$ (see, for example, Wray *et al.* [84]), is then given by

$$\frac{\partial \phi}{\partial t} + \bar{u} \frac{\partial \phi}{\partial r} = \frac{J\phi}{h}. \tag{6.19}$$

The derivation of (6.19) is given in Appendix B. Equation (6.19) has the characteristic equations

$$\frac{\mathrm{d}r}{\mathrm{d}t} = \bar{u} \quad \text{and} \quad \frac{\mathrm{d}\phi}{\mathrm{d}t} = \frac{J\phi}{h}. \tag{6.20}$$

By dividing the first of the characteristic equations (6.20) by $\mathrm{d}\theta_b/\mathrm{d}t$ (5.2), we obtain

$$\frac{\mathrm{d}r/\mathrm{d}t}{\mathrm{d}\theta_b/\mathrm{d}t} = \frac{\mathrm{d}r}{\mathrm{d}\theta_b} = -\frac{Q(r,t)\,\mathcal{V}(k_0)}{\theta_b(t)\mathcal{H}(r,k_0)\mathcal{F}(k_0)}. \tag{6.21}$$

Integrating from $r = k_0$ to $r$ gives

$$-\int_{r_0}^r \frac{\mathcal{H}(r,k_0)\mathcal{F}(k_0)}{Q(r,t)\mathcal{V}(k_0)}\,\mathrm{d}r = \int_{r_0}^r \frac{1}{\theta_b} \frac{1}{\frac{\mathrm{d}r}{\mathrm{d}\theta_b}}\,\mathrm{d}r = \int_1^{\theta_b} \frac{1}{\theta_b}\,\mathrm{d}\theta_b = \log\theta_b, \tag{6.22}$$

where $r_0(r,t)$ is the initial radial position of a particle that is at the radial position $r$ at time $t$.

The second of the characteristic equations (6.20) gives

$$\frac{\mathrm{d}\phi/\mathrm{d}t}{\mathrm{d}r/\mathrm{d}t} = \frac{\mathrm{d}\phi}{\mathrm{d}r} = \frac{J\phi}{h}\frac{h}{Q} = \frac{J\phi}{Q}, \tag{6.23}$$

which leads to

$$\int_{r_0}^{r} \frac{J}{Q}\,\mathrm{d}r = \int_{r_0}^{r} \frac{1}{\phi}\frac{\mathrm{d}\phi}{\mathrm{d}r}\,\mathrm{d}r = \log\left(\frac{\phi}{\phi_0}\right), \tag{6.24}$$

where $\phi_0$ is unity by definition. Adding together the two results from (6.22) and (6.24), we obtain

$$\log\theta_b(t) + \log\left(\frac{\phi(r,t)}{\phi_0}\right) = \log\frac{r_0(r,t)Q(r_0,t)}{rQ(r,t)}. \tag{6.25}$$

Taking the exponent of (6.25) and rearranging for $\phi$ gives

$$\phi(r,t) = \frac{\phi_0 r_0(r,t)Q(r_0,t)}{\theta_b(t)rQ(r,t)}, \tag{6.26}$$

where $r_0(r,t)$ is determined by solving (6.22) for $r_0(r,t)$.

## 6.3   Solving for the mass of suspended particles

The total mass of suspended particles in the bulk of the droplet, $M(t)$, is non-dimensionalised according to $\hat{M} = \hat{\rho}\hat{b}^3\hat{\theta}_{b0}M$, and is given by

$$M(t) = 2\pi\int_{k_0}^{1} \phi h r\,\mathrm{d}r = 2\pi\int_{k_0}^{1} r\phi(r,t)\theta_b(t)\mathcal{H}(r,k_0)\,\mathrm{d}r, \tag{6.27}$$

and the initial mass of suspended particles in the droplet, $M(0) = M_0$, is given by

$$M_0 = \int_{k_0}^{1} r\phi_0\mathcal{H}(r,k_0)\,\mathrm{d}r. \tag{6.28}$$

The masses of particles at the inner contact line, $M_a$, and the outer contact line, $M_b$, can be found by calculating the flow of the suspended particles through the contact lines,

$$M_a(t) = -\int_0^t \lim_{r \to k_0} \int_0^h \phi(r,t)\bar{u}(r,t)r\,\mathrm{d}z\,\mathrm{d}t = -\int_0^t \lim_{r \to k_0} \phi(r,t)Q(r,t)r\,\mathrm{d}t, \quad (6.29)$$

$$M_b(t) = \int_0^t \lim_{r \to 1} \int_0^h \phi(r,t)\bar{u}(r,t)r\,\mathrm{d}z\,\mathrm{d}t = \int_0^t \lim_{r \to 1} \phi(r,t)Q(r,t)r\,\mathrm{d}t, \quad (6.30)$$

respectively.

## 6.4 Deposition of an annular droplet with a spatially-uniform evaporative flux

In the case of a spatially-uniform evaporative flux, where $J$ is given by (2.16), $\bar{u}$, $Q$, and $\phi$, given by (6.9), (6.16) and (6.26), respectively, are

$$Q = \frac{2(1-r^2)(k_0^2 + r^2)\log k_0 - 4r^2(1-k_0^2)\log r}{r\pi((k_0^2+1)\log k_0 + 1 - k_0^2)}, \quad (6.31)$$

$$\bar{u} = \frac{(2\log k_0 + 1 - k_0^2)\left(2(1-r^2)(k_0^2 + r^2)\log k_0 - 4r^2(1-k_0^2)\log r\right)}{\theta_b r\pi\left[(k_0^2+1)\log k_0 + 1 - k_0^2\right]\left[(1-r^2)\log k_0 - (1-k_0^2)\log r\right]}, \quad (6.32)$$

$$\phi = \frac{\phi_0 r_0 Q(r_0)}{\theta_b r Q(r)} = \frac{\phi_0\left((1-r_0^2)(k_0^2 + r_0^2)\log k_0 - 2r_0^2(1-k_0^2)\log r_0\right)}{\theta_b\left((1-r^2)(k_0^2 + r^2)\log k_0 - 2r^2(1-k_0^2)\log r\right)}. \quad (6.33)$$

There is a critical value of $r$, denoted by $r = \mathcal{R}$, at which $\bar{u} = 0$. This critical value $\mathcal{R}$ refers to the position in the droplet at which there is a change in direction of the flow of suspended particles. Since $Q = 0$ when $\bar{u} = 0$, this critical value of $\mathcal{R}$ can be found by solving $Q(\mathcal{R}, k_0) = 0$, which is satisfied when

$$\left[\mathcal{R}^4 - k_0^2 + \mathcal{R}^2(k_0^2 - 1)\right]\log k_0 + 2\mathcal{R}^2(1-k_0^2)\log \mathcal{R} = 0, \quad (6.34)$$

and has the solution $\mathcal{R} = \sqrt{k_0}$. Note that $\mathcal{R} = -\sqrt{k_0}$ is also a solution to (6.34), however this solution is not physically relevant. Experimentally, the critical value $\mathcal{R}$ could be found using dyes and tracers. This would involve injecting the droplet with a dye that makes the flow within the droplet visible. In this case, investigating the region around the critical value $r = \mathcal{R} = \sqrt{a}$ would reveal flow on either side of $\mathcal{R}$ in different directions.

To determine the direction in which the liquid is moving, and hence in which the suspended particles are convected, we first need to determine the sign of $\bar{u}$ at either side of the critical position $r = \mathcal{R}$. Since there is only one physically relevant solution for (6.34), we can instead calculate the sign of $\bar{u}$ in the limits $r \to k_0^+$ and $r \to 1^-$ without the loss of generality. In the limits $r \to k_0^+$ and $r \to 1^-$, $\bar{u}$ tends to

$$
\begin{aligned}
\lim_{r \to k_0^+} \bar{u} &= \lim_{r \to k_0^+} \left( \frac{Q}{h} \right) \\
&= -\frac{4k_0(k_0^2 - 1 - 2\log k_0)(\log k_0(k_0^2 + 1) - k_0^2 + 1)}{\left[ k_0^2(2\log k_0 - 1) + 1 \right] \left[ (1 - k_0^2)(\pi - 8t) - (\pi(1 + k_0^2) - 16t)\log k_0 \right]} < 0,
\end{aligned}
$$

$$(6.35)$$

and

$$
\begin{aligned}
\lim_{r \to 1^-} \bar{u} &= \lim_{r \to 1^-} \left( \frac{Q}{h} \right) \\
&= \frac{4[1 - k_0^2 + (1 + k_0^2)\log k_0]}{(1 - k_0^2)(\pi - 8t) - (\pi(1 + k_0^2) - 16t)\log k_0} > 0.
\end{aligned}
$$

$$(6.36)$$

Equations (6.35) and (6.36) illustrate that the limiting values of $\bar{u}$ at $r = k_0^+$ and $r = 1^-$ are finite, and satisfy $\bar{u} < 0$ near the inner contact line and $\bar{u} > 0$ near the outer contact line. Since there is only one value for $\mathcal{R}$ in $k_0 < \mathcal{R} < 1$, in $k_0 < r < \mathcal{R}$ the flow within the droplet is towards the inner contact line, and that in $\mathcal{R} < r < 1$ the flow within the droplet is towards the outer contact line.

Figures 6.1, 6.2 and 6.3 show (a) $J(r,t)$ from (2.16), (b) $Q(r,t)$, (c) $\phi(r,t)$, (d) $\phi h(r,t)$, (e) $M_{\mathrm{droplet}}(t)$, $M_a(t)$, and $M_b(t)$ and (f) $M_a/(2\pi k_0)$ and $M_{\mathrm{b}}/(2\pi)$ for a droplet with a spatially-uniform evaporative flux with $k_0 = 0.2, 0.5, 0.8$.

Figures 6.1(b), 6.2(b) and 6.3(b) confirm that $Q(r,t) < 0$ near the inner contact line $r = k_0$ and $Q(r,t) > 0$ near the outer contact line $r = 1$. Therefore suspended particles are advected towards both contact lines. Figures 6.1(c), 6.2(c) and 6.3(c) show the concentration of suspended particles $\phi$ plotted as a function of $r$ at time intervals of $t_{\mathrm{lifetime}}/10$. Figures 6.1(e), 6.2(e) and 6.3(e) show the decrease in $M$, and the increase of $M_a$ and $M_b$, as the suspended particles are advected to the contact lines of the droplet and leave the bulk of the droplet. Figures 6.1(f), 6.2(f) and 6.3(f) illustrate that while during the evaporation process the density of the deposit at the outer contact line is higher than that at the inner contact line, at $t = t_{\mathrm{lifetime}}$ the density of the deposits at the two contact lines are equal. As $k_0$ is increased (i.e. in the limit $k_0 \to 1^-$), the density at the inner and outer contact lines become more alike throughout the evaporation process.

## 6.5 Deposition of an annular droplet with a diffusion-limited evaporative flux

In the diffusion-limited case, the presence of square root singularities in $J$ at the contact lines mean that now $J(r,t) \to \infty$ at $r = k_0$ and $r = 1$, rather than being finite, as was the case for the spatially-uniform evaporative flux. This means that in the limits $r = k_0$ and $r = 1$, $\bar{u}$ will not approach a finite limit. The limit of $\bar{u}$ at

Figure 6.1: (a) $J(r) = J_0 = 4/\pi$ from (2.16), (b) $Q(r,t)$, (c) $\phi(r,t)$ (d) $\phi h(r,t)$, (e) $M(t)$, $M_a(t)$ and $M_b(t)$ and (f) $M_a/(2\pi k_0)$ and $M_b/(2\pi)$. Here $k_0 = 0.2$ and (a)–(d) are plotted as functions of $r$, and (e) and (f) are plotted as functions of $t$, where arrows indicate direction of increasing $t$. In (e) and (f), the mass and density of the inner contact line is represented with a dotted line, and the mass and density of the outer contact line is represented with a dashed line.
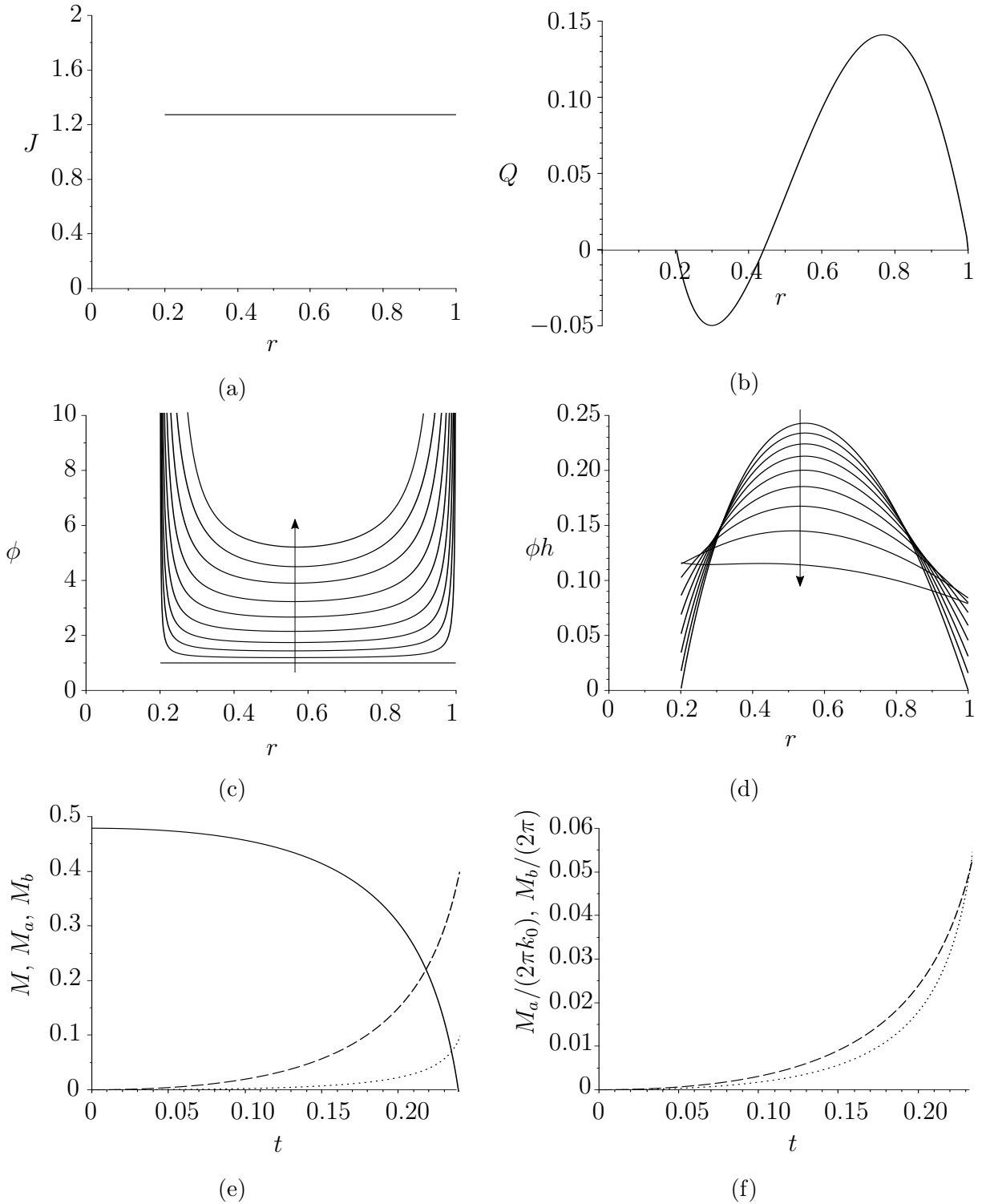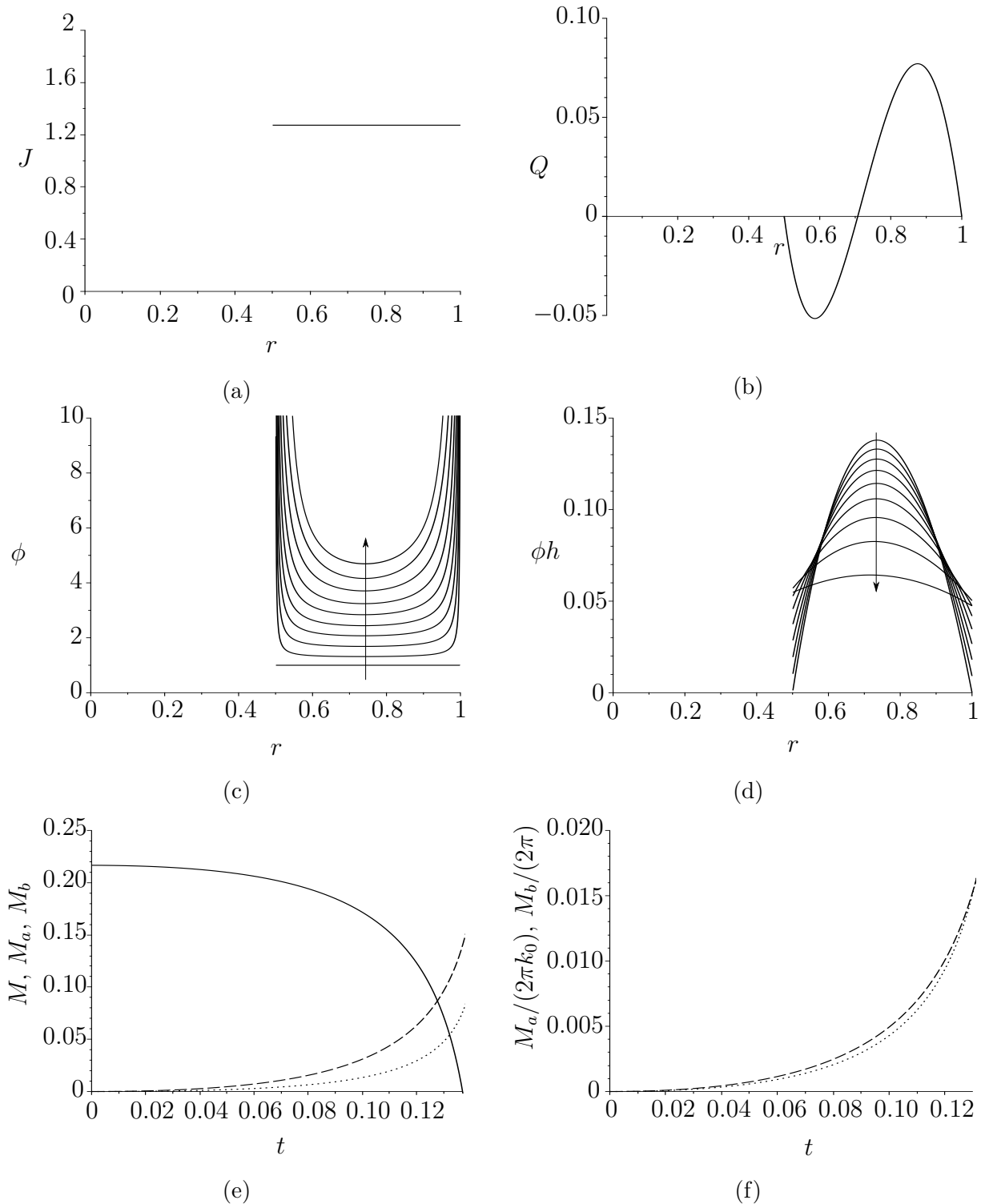
Figure 6.2: (a) $J(r) = J_0 = 4/\pi$ from (2.16), (b) $Q(r,t)$, (c) $\phi(r,t)$ (d) $\phi h(r,t)$, (e) $M(t)$, $M_a(t)$ and $M_b(t)$ and (f) $M_a/(2\pi k_0)$ and $M_b/(2\pi)$. Here $k_0 = 0.5$ and (a)–(d) are plotted as functions of $r$, and (e) and (f) are plotted as functions of $t$, where arrows indicate direction of increasing $t$. In (e) and (f),the mass and density of the inner contact line is represented with a dotted line, and the mass and density of the outer contact line is represented with a dashed line.

Figure 6.3: (a) $J(r) = J_0 = 4/\pi$ from (2.16), (b) $Q(r,t)$, (c) $\phi(r,t)$ (d) $\phi h(t)$, (e) $M(t)$, $M_a(t)$ and $M_b(t)$ and (f) $M_a/(2\pi k_0)$ and $M_b/(2\pi)$. Here $k_0 = 0.8$ and (a)–(d) are plotted as functions of $r$, and (e) and (f) are plotted as functions of $t$, where arrows indicate direction of increasing $t$. In (e) and (f), the mass and density of the inner contact line is represented with a dotted line, and the mass and density of the outer contact line is represented with a dashed line.
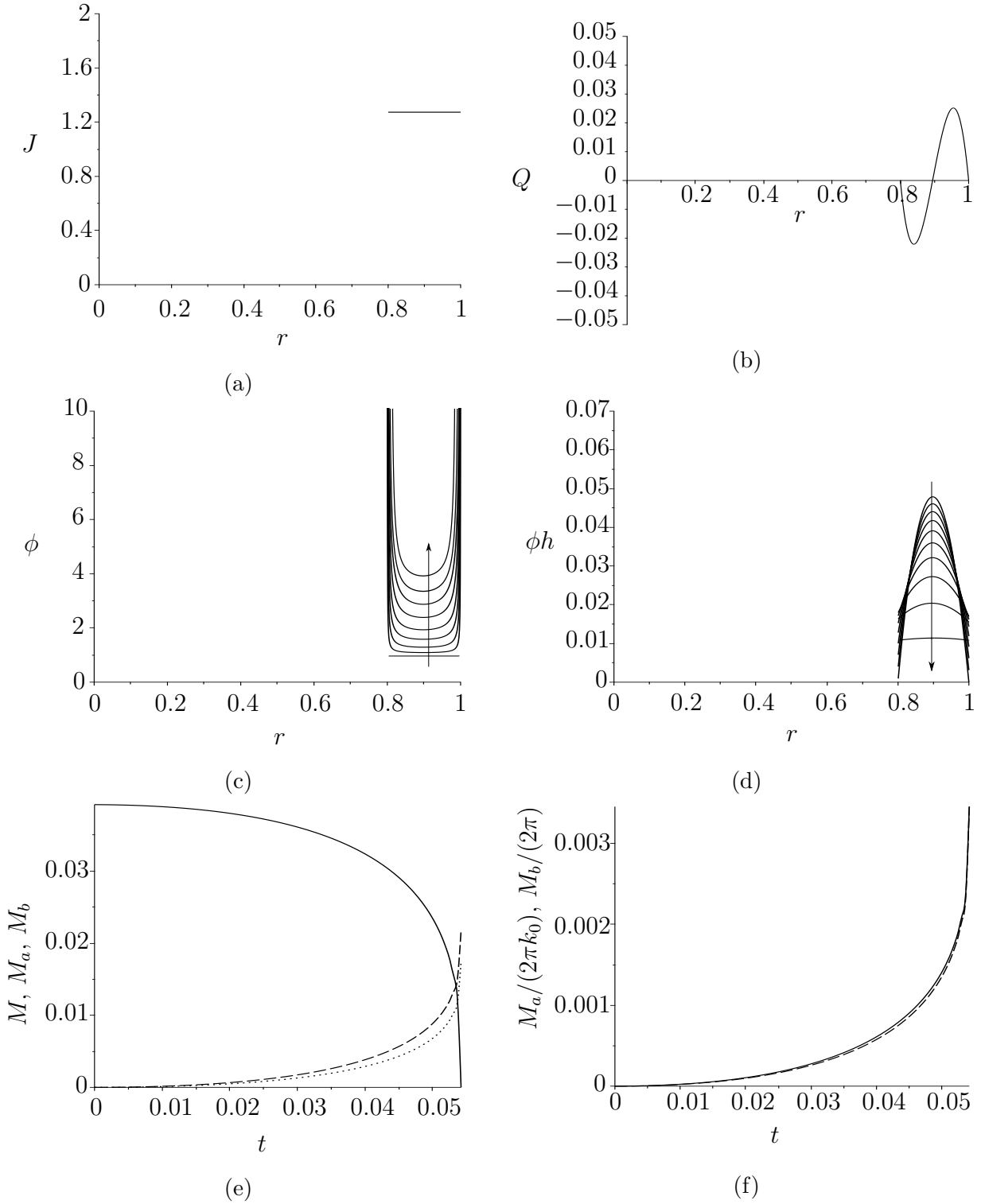
the contact lines is

$$\lim_{r \to k_0^+} \bar{u} = \lim_{r \to k_0^+} \left( \frac{Q}{h} \right) = -\infty, \tag{6.37}$$

$$\lim_{r \to 1^-} \bar{u} = \lim_{r \to 1^-} \left( \frac{Q}{h} \right) = \infty. \tag{6.38}$$

Note that in these calculations a specific expression of $J$ has not been assumed, just that $J(r,t) \to \infty$ as $r \to k_0^+$ and $r \to 1^-$.

Figures 6.4, 6.5 and 6.6 show numerically calculated solutions for (a) $J(r,t)$ obtained via COMSOL (b) $Q(r,t)$, (c) $\phi(r,t)$, (d) $\phi h(r,t)$, (e) $M(t)$, $M_a(t)$ and $M_b(t)$ and (f) $M_a/(2\pi k_0)$ and $M_b/(2\pi)$ for a droplet with diffusion-limited evaporative flux with $k_0 = 0.2, 0.5, 0.8$.

Figures 6.4(b), 6.5(b) and 6.6(b) shows that $Q(r,t) < 0$ near the inner contact line $r = k_0$ and $Q(r,t) > 0$ near the outer contact line $r = 1$. Figures 6.4(e), 6.5(e) and 6.6(e) show the decrease in $M(t)$ over time, and the increase of $M_a(t)$ and $M_b(t)$, as suspended particles are advected to the contact lines of the droplet and leaves the bulk of the droplet. Figures 6.4(f), 6.5(f) and 6.6(f) show that the density of the deposit at the contact lines is no longer equal at $t = t_{\text{lifetime}}$ (as was the case with the spatially-uniform evaporative flux). Instead the density of deposit at the outer contact line stays higher than that at the inner contact line.

## 6.6  Comparison between spatially-uniform and diffusion-limited evaporative fluxes

Figures 6.7(a) and 6.8(a) show plots of the critical value of $r$, $\mathcal{R}$, plotted as a function of $k_0$. The critical value $\mathcal{R}$ is strictly greater for the spatially-uniform evaporative

Figure 6.4: Numerically calculated solutions for (a) $J(r,t)$, (b) $Q(r,t)$, (c) $\phi(r,t)$ (d) $\phi h(r,t)$, (e) $M(t)$, $M_a(t)$ and $M_b(t)$ and (f) $M_a/(2\pi k_0)$ and $M_b/(2\pi)$. Here $k_0 = 0.2$ and (a)–(d) are plotted as functions of $r$, and (e) and (f) are plotted as functions of $t$, where arrows indicate direction of increasing $t$. In (e) and (f), quantities at the inner contact line is represented with a dotted line, and those at the outer contact line is represented with a dashed line.
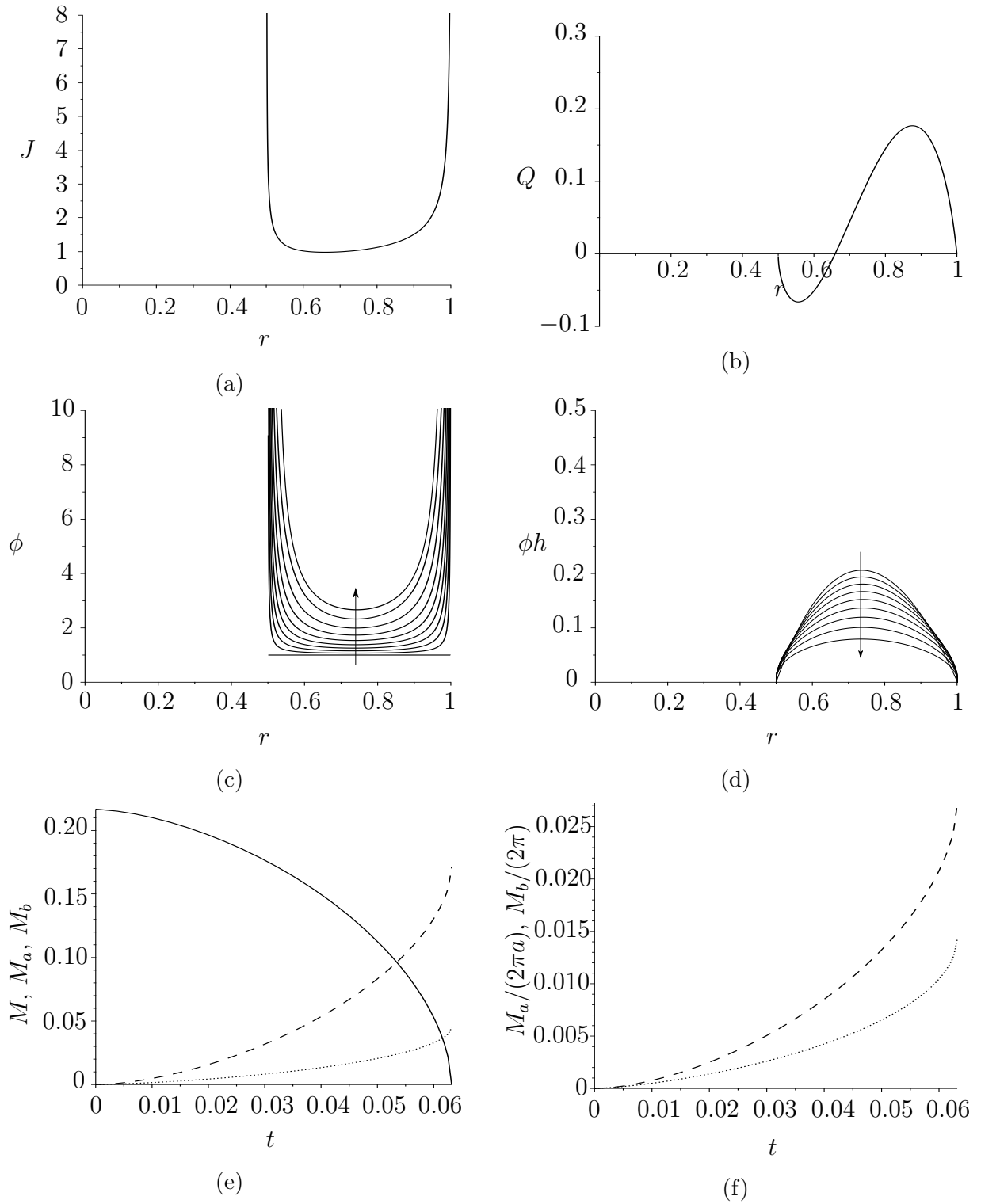
Figure 6.5: Numerically calculated solutions for (a) $J(r,t)$, (b) $Q(r,t)$, (c) $\phi(r,t)$ (d) $\phi h(r,t)$, (e) $M(t)$, $M_a(t)$ and $M_b(t)$ and (f) $M_a/(2\pi k_0)$ and $M_b/(2\pi)$. Here $k_0 = 0.5$ and (a)–(d) are plotted as functions of $r$, and (e) and (f) are plotted as functions of $t$, where arrows indicate direction of increasing $t$. In (e) and (f), quantities at the inner contact line is represented with a dotted line, and those at the outer contact line is represented with a dashed line.
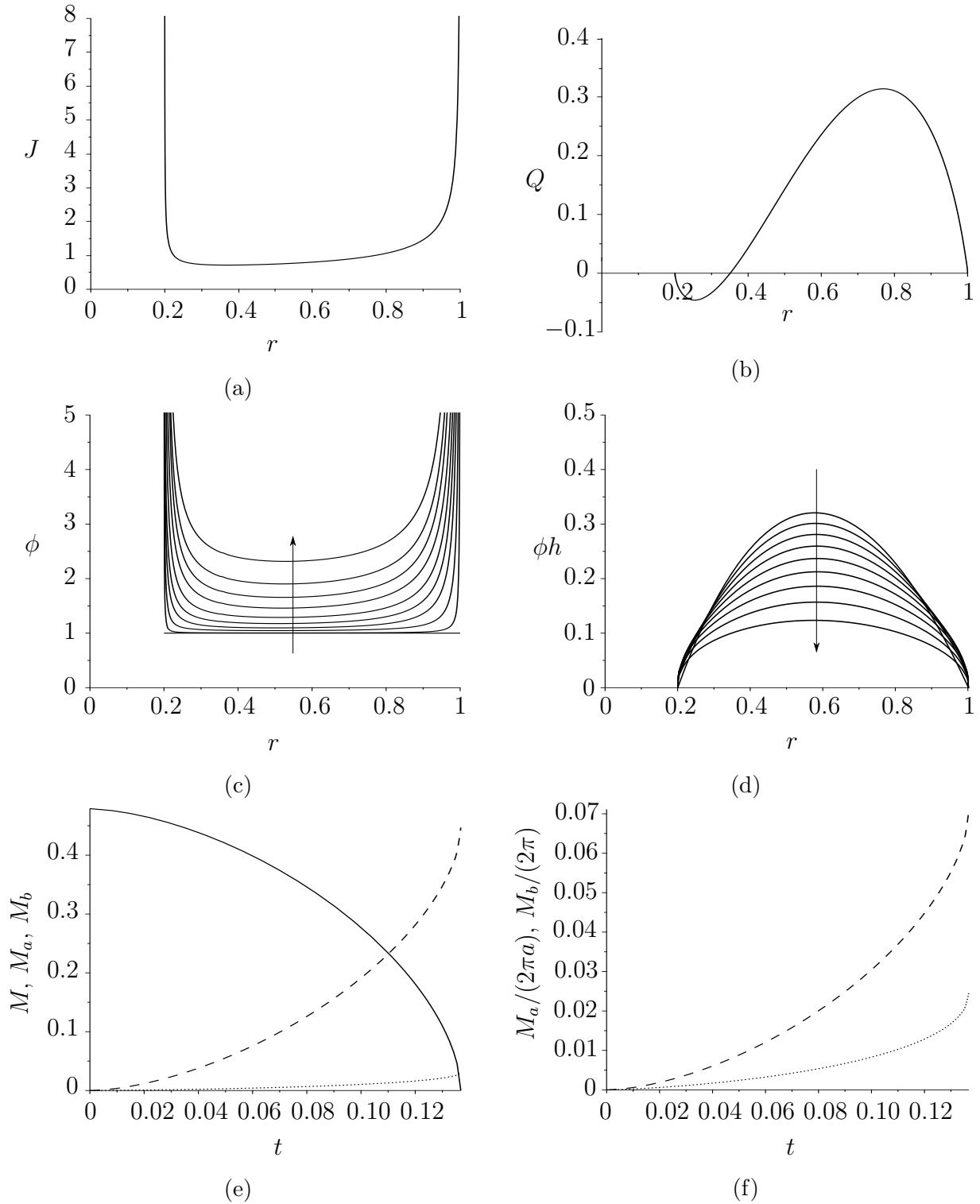
Figure 6.6: Numerically calculated solutions for (a) $J(r,t)$, (b) $Q(r,t)$, (c) $\phi(r,t)$ (d) $\phi h(r,t)$, (e) $M(t)$, $M_a(t)$ and $M_b(t)$ and (f) $M_a/(2\pi k_0)$ and $M_b/(2\pi)$. Here $k_0 = 0.8$ and (a)–(d) are plotted as functions of $r$, and (e) and (f) are plotted as functions of $t$, where arrows indicate direction of increasing $t$. In (e) and (f), quantities at the inner contact line is represented with a dotted line, and those at the outer contact line is represented with a dashed line.
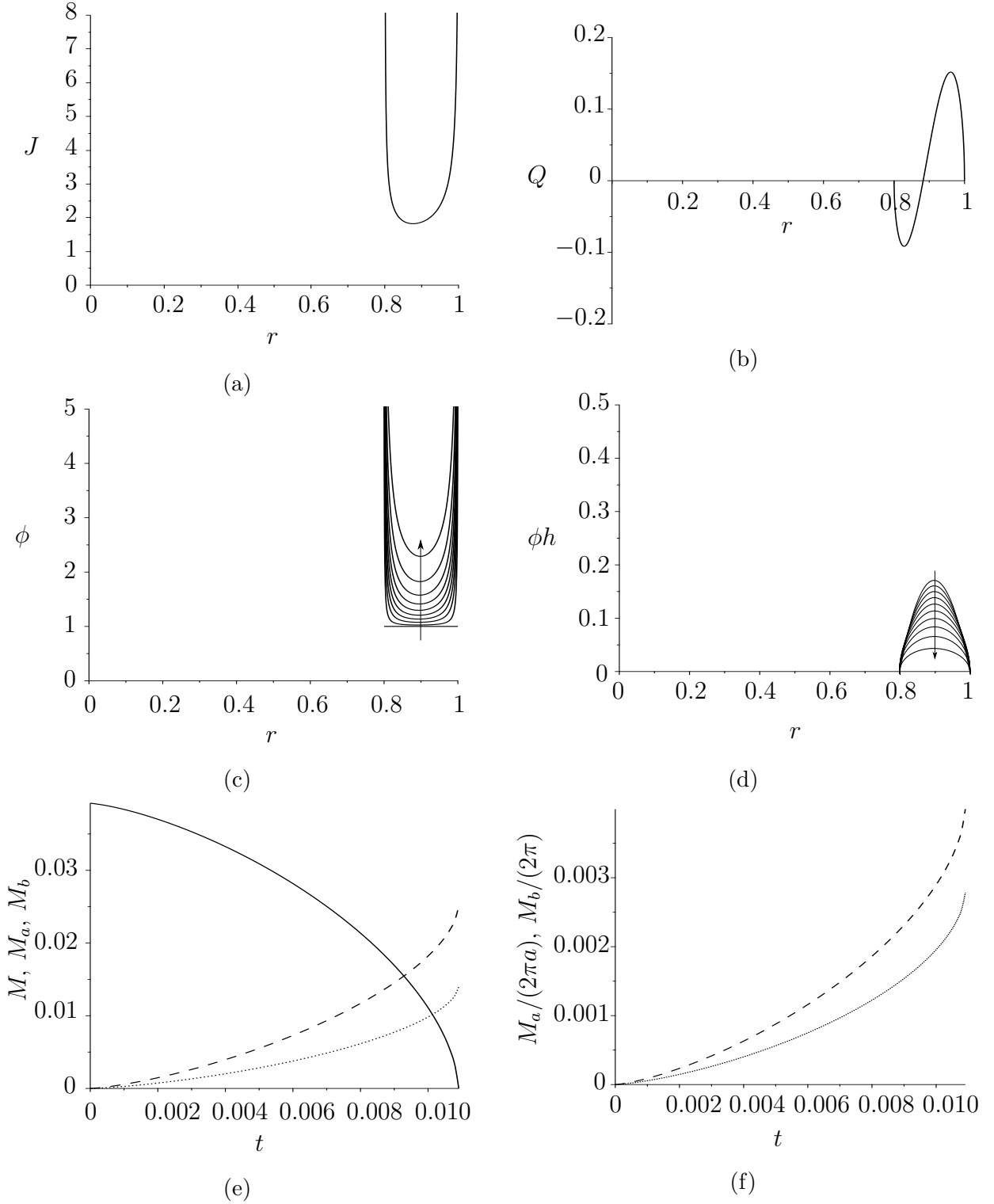
flux than for the diffusion-limited evaporative flux for all $0 < k_0 < 1$, however, they do coincide when $k_0 = 0$ and $k_0 = 1$.

Figures 6.7(b) and 6.8(b) show a comparison of the final split of mass between the inner and outer contact lines at $t = t_{\text{lifetime}}$ and the initial mass of suspended particles in the bulk of the droplet. The final mass of suspended particles at the outer contact line is strictly greater than that at the inner contact line for all $k_0$. In the limit $k_0 \to 0^+$, we expect the final split in mass to return to that of a spherical-cap droplet, and indeed, $M_a(t_{\text{lifetime}}) \to 0$ in this limit, and the suspended particles in the bulk of the droplet is all advected to the outer contact line. In the limit $k_0 \to 1^-$, both $M_a(t_{\text{lifetime}}) \to 0$ and $M_b(t_{\text{lifetime}}) \to 0$ as $V \to 0$, and so $M_0 \to 0$.

Figure 6.7(c) shows that the ratio of masses at the inner and outer contact lines at $t = t_{\text{lifetime}}$ is equal to $k_0$ (i.e. $M_a/M_b = k_0$) and hence that the ratio of densities at $t = t_{\text{lifetime}}$, is equal to unity for all values of $k$. Figures 6.7(d) and 6.8(d) show the ratio of the densities at the inner and contact lines, $M_a/(2\pi k_0)$ and $M_b/(2\pi)$, plotted as a function of time. These plots show that for a spatially-uniform evaporative flux, density of the deposit at the outer contact line is higher than at the inner contact line during the evaporation. However, at $t = t_{\text{lifetime}}$ the densities are equal. In the case of the diffusion-limited evaporative flux, shown in Figure 6.8(c), the final density is lower for smaller values of $k_0$, and lower than 1 for all values of $k_0$, showing that the density of suspended particles at the outer contact line is greater than that at the inner contact line throughout the evaporation for all values of $k_0$.
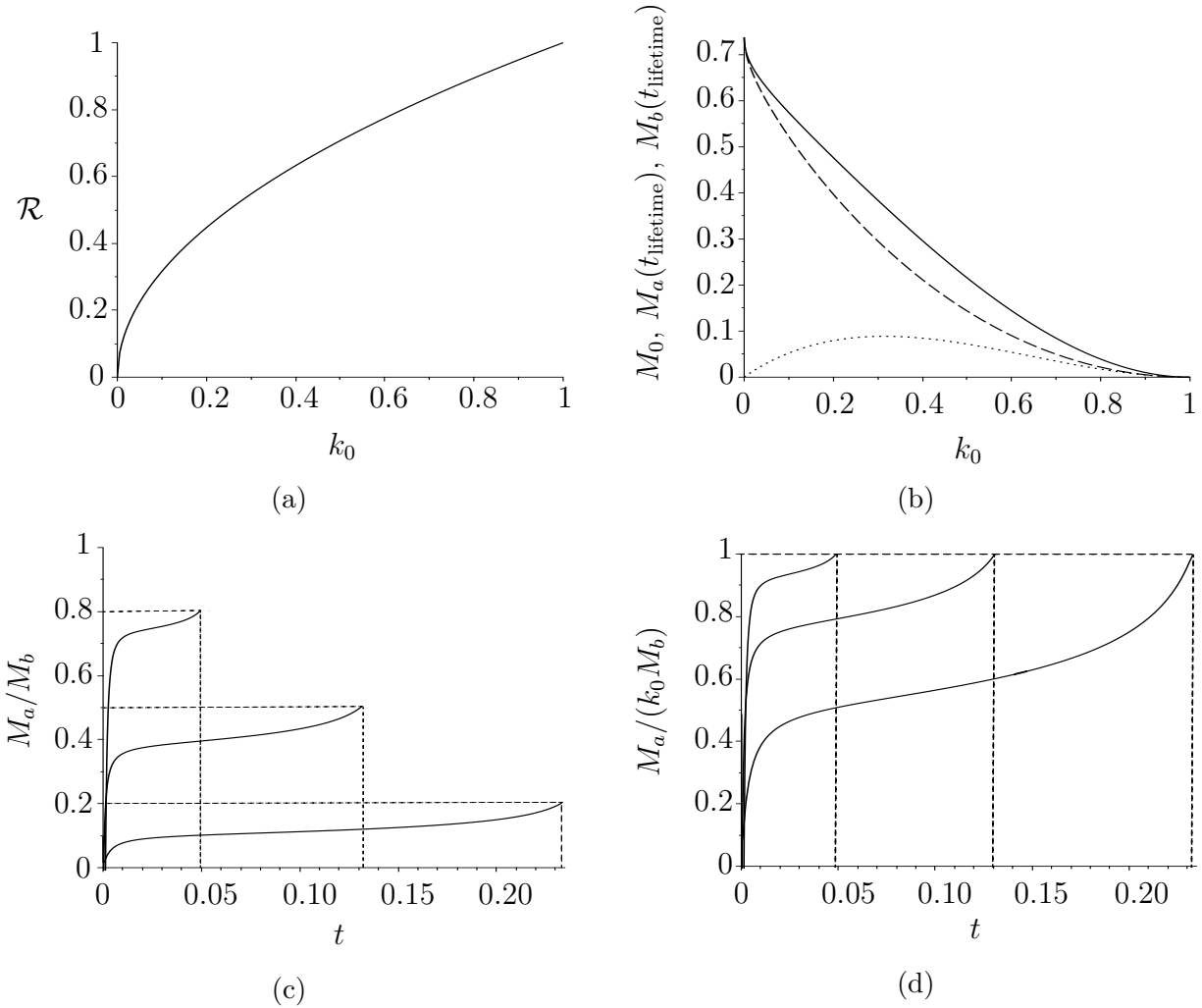
Figure 6.7: (a) $\mathcal{R}(k_0) = \sqrt{k_0}$, the solution to (6.34), (b) the initial mass of the droplet $M_0$ ( solid line), and the final masses at the contact lines $M_a(t_{\text{lifetime}})$ (dotted line), and $M_b(t_{\text{lifetime}})$ (dashed line), (c) $M_a/M_b$ and (d) $M_a/(k_0 M_b)$ for a spatially-uniform evaporative flux (2.16).
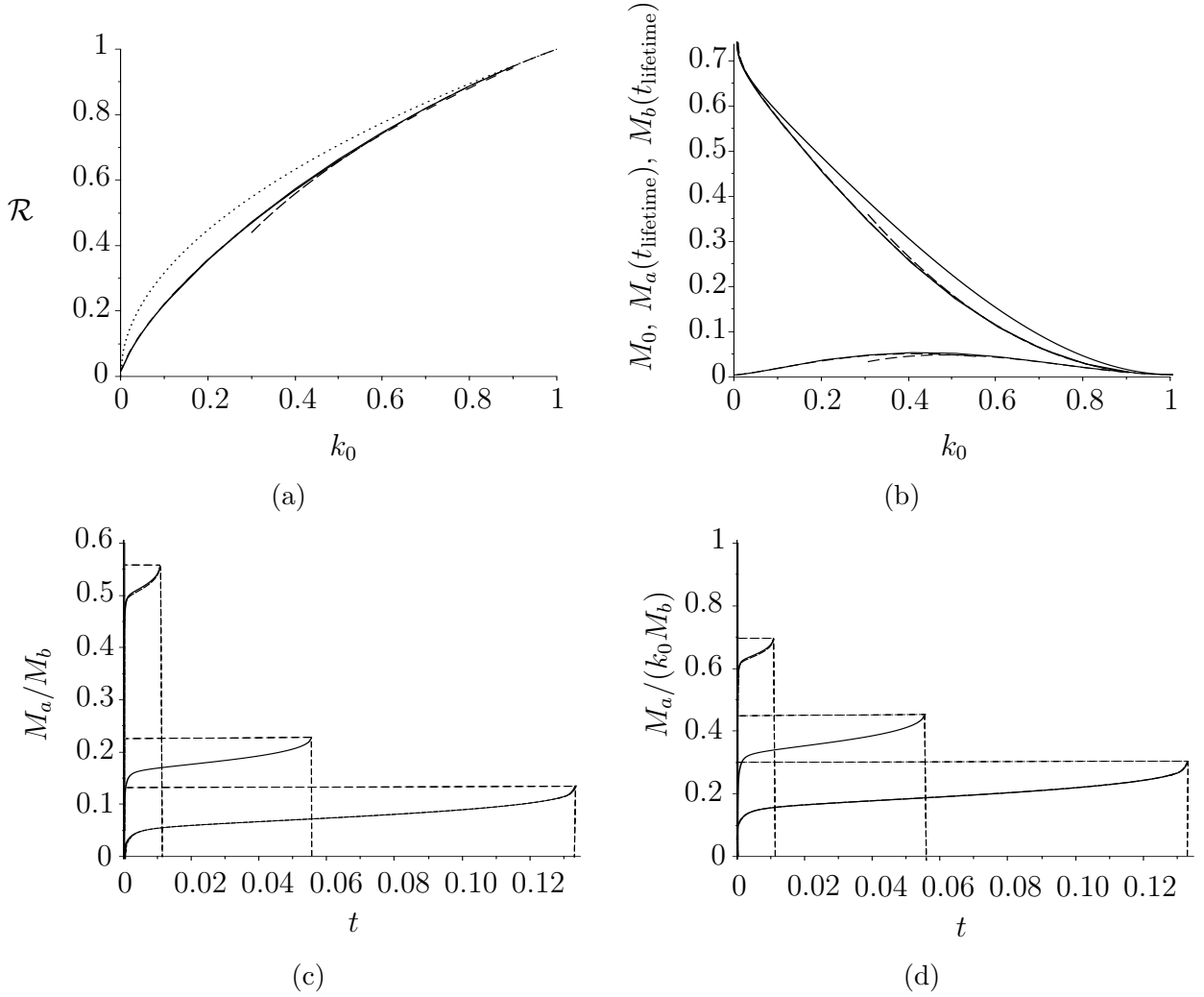
Figure 6.8: (a) $\mathcal{R}(k_0)$, for the numerical solution for $J$ (solid line), the asymptotic solutions in the limit $k_0 \rightarrow 1^-$ (dashed line), and the solution in the spatially-uniform evaporative flux case (dotted line), (b) $M_0$, $M_a(t_{\text{lifetime}})$ and $M_b(t_{\text{lifetime}})$, for the numerical solution to $J$ (solid line), the asymptotic solution for $M_a(t_{\text{lifetime}})$ and $M_b(t_{\text{lifetime}})$ in the limit $k \rightarrow 1^-$ (dashed line), (c) $M_a/M_b$ and (d) $M_a/(k_0 M_b)$, where dashed lines represent asymptotic solutions in the limit $k_0 \rightarrow 1^-$ (4.16).

# Chapter 7

# Conclusions and further work

## 7.1 Conclusions

In this thesis we have analysed the evolution of, and deposition from, an evaporating sessile annular droplet.

In Chapter 2 we formulated the mathematical problem of an evaporating annular droplet, namely the governing equations, associated boundary conditions and the local and total evaporative fluxes.

In Chapter 3 we determined the geometry of an annular droplet, deriving the expressions for the profile, volume and inner contact line of a thin droplet.

In Chapter 4 we derived expressions for the concentration of vapour in the atmosphere and the local and total evaporative fluxes. We obtained numerical solutions, utilising COMSOL Multiphysics® [19] for $c$ and hence obtained numerical solutions for $J$ and $F$. We also made use of the method suggested by Cooke [20] to solve for $F$ without first having to solve for either $c$ or $J$. We also discussed the asymptotic solutions for $F$ in the limit $k \to 0^+$ obtained by Collins [18], and the asymptotic

solution for $J$ and $F$ in the limit $k \to 1-$ obtained by Leppington & Levine [47]. Finally, we discussed several formulations of approximate solutions of $F$, including those obtained by Gladwell & Gupta [36], Laraqi [43], and Willert *et al.* [78].

In Chapter 5, we considered four modes of evaporation for an evaporating annular droplet and derived expressions for the evolution and lifetime of the droplet in each of these modes for both a spatially-uniform and a diffusion-limited evaporative flux. We also compared the lifetimes of the droplet in the different modes with those of a spherical-cap shaped droplet. In the limit $k \to 0^+$, the lifetime of an annular droplet evaporating with both spatially-uniform and diffusion-limited evaporative fluxes tend to the lifetime of a spherical-cap droplet. Specifically, modes of evaporation in which the outer contact line is pinned tend to the lifetime of a spherical-cap droplet evaporating in the CR mode, while modes in which the outer contact line is free tend to the lifetime of a spherical-cap droplet evaporating in the CA mode.

In Chapter 6 we discussed the evaporation of a particle-laden annular droplet, and consider the deposition from such a droplet with either a spatially-uniform or a diffusion-limited evaporative flux. In both cases we show there will be deposits at both contact lines, and determine the critical value of $r = \mathcal{R}$, which determines the radial position at which the flow changes direction. In the case of a spatially-uniform evaporative flux, the density of the final deposits at the contact lines are the same, while in the case of a diffusion-limited evaporative flux the density of the deposit at the outer contact line is strictly greater than that at the inner contact line throughout the evaporation.

## 7.2 Further work

While this work described four modes of evaporation for an annular droplet, other more complicated modes of evaporation are, of course, possible. The approach used in this thesis could be extended to include mixed modes of evaporation. A stick–jump motion of one or both of the contact lines is of particular interest due to the experimental findings of Vlasko-Vlasov *et al.* [76] who, as discussed in Chapter 1.5, observed a stick–jump motion of the outer contact line of an annular droplet in a well.

This work described the deposition patterns due to both spatially-uniform and diffusion-limited evaporative fluxes, both of which resulted in the well-known coffee-ring effect at both the inner and outer contact lines. Further work could expand on this to consider more complicated evaporative fluxes, which could result in more complicated deposition patterns.

The present work only studied the deposition patterns arising in the pinned–pinned mode of evaporation. The approached used in this thesis could be extended to include the deposition patterns of both the other modes of evaporation described in this thesis, and other mixed modes of evaporation. In the pinned–pinned mode, the critical value of $\mathcal{R}$ was shown to be constant, however in other modes of evaporation $\mathcal{R}$ will, in general, be a function of $k$ (and possibly $b$), which might well lead to more complicated deposition patterns.

Future research on this topic can also include testing the theoretical predictions of this work experimentally. Experimental results for the lifetimes of an annular droplet in each of the four modes of evaporation, and the deposition from an annular droplet in the pinned–pinned mode are of particular interest. Moreover, as discussed in Chapter 1.6, annular droplets can be created experimentally by utilising a substrate

patterned with a hydrophobic coating (see, for example, Lenz *et al.* [46], Jokinen *et al.* [41], Schäfle *et al.* [69]). This configuration would allow for the pinning of various contact lines depending on the pattern of the coating.

# Appendix A

# Aymptotic Solutions for $J$ and $F$ in the limit $k \to 1^-$

In this Appendix we will derive the asymptotic solutions for $J$ and $F$ in the limit $k \to 1^-$ given in (4.16) and (4.17) in the main text. Following the method of Leppington & Levine [47], we correct their error in calculating $J$.

Applying Green's Theorem to Laplace's equation (2.1) yields an integral equation for $J$, and imposing the boundary condition (2.10) gives

$$1 = -\frac{1}{4\pi} \int_a^b K(r, r_1) J(r) r \, \mathrm{d}r, \tag{A.1}$$

where the kernel $K(r, r_1)$ is given by

$$K(r, r_1) = \frac{8}{r + r_1} \mathcal{K}\left(\frac{4rr_1}{(r + r_1)^2}\right), \tag{A.2}$$

where $\mathcal{K}(\alpha)$ is the complete elliptic integral of the first kind,

$$\mathcal{K}(\alpha) = \int_0^{\pi/2} \frac{1}{\sqrt{1 - \alpha \sin^2(t)}} \, dt, \tag{A.3}$$

where

$$\alpha = \frac{4rr_1}{(r + r_1)^2}. \tag{A.4}$$

To analyse the limit $k \to 1^-$, we write

$$\varepsilon = \frac{b}{a} - 1 = \frac{1}{k} - 1, \tag{A.5}$$

and take the limit $\varepsilon \to 0^+$. We introduce the change of variables

$$r = a(1 + \varepsilon R), \quad r_1 = a(1 + \varepsilon R_1), \quad J(r) = -\frac{4\pi W(R)}{r}. \tag{A.6}$$

Using (A.6), integral equation for $J(r)$ (A.1) becomes

$$1 = a\varepsilon \int_0^1 K(R, R_1) W(R) \, dR. \tag{A.7}$$

To obtain the asymptotic solution for $W(R)$ in the limit $\varepsilon \to 0^+$, we expand $K(R, R_1)$ and $W(R)$ in terms of $\varepsilon$,

$$K(R, R_1) = K_0(R, R_1) + \varepsilon K_1(R, R_1) + o(\varepsilon), \quad W(R) = W_0(R) + \varepsilon W_1(R) + o(\varepsilon), \tag{A.8}$$

where the elliptic integral in (A.3) can be expanded using

$$\mathcal{K}(\alpha) \sim \log\left(\frac{4}{\sqrt{1 - \alpha}}\right) \tag{A.9}$$

in the limit $\alpha \to 1$ (see, for example, Carlson & Gustafson [13]). Expanding $K$ given

by (A.2) using (A.9) gives

$$K_0(R, R_1) = -\frac{4}{a} \left[ \log \varepsilon + \log \left( \frac{|R - R_1|}{8} \right) \right], \tag{A.10}$$

$$K_1(R, R_1) = -\frac{4}{a} \left[ -\frac{1}{2}(R + R_1) \log \varepsilon - \frac{1}{2}(R + R_1) \log \left( \frac{e|R - R_1|}{8} \right) \right]. \tag{A.11}$$

The error in Leppington & Levine's work [47] came from the expression for $K_1$, where instead of the (A.11), they wrote

$$K_1(R, R_1) = -\frac{4}{a} \left[ -\frac{1}{2}(R + R_1) \log \varepsilon - \frac{1}{2} \log \left( \frac{e|R - R_1|}{8} \right) \right], \tag{A.12}$$

which omits the second $R + R_1$ term.

The expressions for $K_0$ and $K_1$ given by (A.10) and (A.11) can be used to calculate the expressions for $W_0$ and $W_1$, appearing in (A.8). Once these are known we can then derive expressions for $J(r, t)$ and $F(t)$.

First, to calculate $W_0(R)$, we evaluate (A.7) at leading order in $\varepsilon$,

$$1 = a\varepsilon \int_0^1 K_0(R, R_1) W_0(R) \, dR, \tag{A.13}$$

resulting in

$$-\frac{1}{4\varepsilon} = \log\left(\frac{\varepsilon}{8}\right) \int_0^1 W_0(R) \, dR + \int_0^1 \log|R - R_1| W_0(R) \, dR. \tag{A.14}$$

Cooke [21] gave the solution for an unknown function $\Phi(R)$ in an integral equation of the form

$$\int_0^1 \log|R - R_1| \Phi(R) \, dR = \pi f(R_1), \tag{A.15}$$

where $f(R_1)$ is a known function of $R_1$. In particular, he gave the solution as

$$\Phi(R) = \frac{1}{\pi R^{1/2}} \frac{\mathrm{d}}{\mathrm{d}R} \left( \int_R^1 \frac{S(x)}{\sqrt{x-R}} \, \mathrm{d}x \right) - \frac{1}{2\pi \log 2\sqrt{R(1-R)}} \int_0^1 \frac{f(R_1)}{\sqrt{R_1(1-R_1)}} \, \mathrm{d}R_1,$$
(A.16)

where

$$S(x) = \int_0^x \frac{R_1^{1/2} f'(R_1)}{(x-R_1)^{1/2}} \, \mathrm{d}R_1.$$
(A.17)

The integral equation (A.14) can be written in the form of (A.15) by writing

$$f(R_1) = -\frac{1}{\pi} \left( \frac{1}{4\varepsilon} + \log\left(\frac{\varepsilon}{8}\right) \int_0^1 W_0(R) \, \mathrm{d}R \right).$$
(A.18)

However, since $f$ is actually independent of $R_1$ (and thus $f'(R_1) \equiv 0$ and $S(x) \equiv 0$), the solution for $W_0$ is independent of $R_1$ and is given by

$$W_0 = -\frac{1}{2\pi \log 2\sqrt{R(1-R)}} \left( \frac{1}{4\varepsilon} + \log\left(\frac{\varepsilon}{8}\right) \int_0^1 W_0(R) \, \mathrm{d}R \right),$$
(A.19)

which, by integrating with respect to $R$ between 0 and 1, gives

$$\int_0^1 W_0(R) \, \mathrm{d}R = -\frac{1}{4\varepsilon \log\left(\frac{32}{\varepsilon}\right)}.$$
(A.20)

Substituting the expression for $\int_0^1 W_0(R) \, \mathrm{d}R$ from (A.20) into the right hand side of (A.19) gives

$$W_0 = -\frac{1}{4\varepsilon\pi \log(\frac{32}{\varepsilon})} \frac{1}{\sqrt{R(1-R)}}.$$
(A.21)

To find $W_1$, we evaluate (A.7) at order $\varepsilon$,

$$0 = \int_0^1 (K_0(R, R_1) W_1(R) + K_1(R, R_1) W_0(R)) \, \mathrm{d}R.$$
(A.22)

By substituting $K_0$, $K_1$ and $W_0$, given by (A.10), (A.11) and (A.21) respectively, into (A.22) we obtain

$$\frac{2 + (1 + 2R_1)\log(\frac{\varepsilon}{32})}{16\varepsilon \log(\frac{32}{\varepsilon})} - \log\left(\frac{\varepsilon}{8}\right) \int_0^1 W_1 \, \mathrm{d}R = \int_0^1 \log|R - R_1| W_1 \, \mathrm{d}R, \qquad \text{(A.23)}$$

which is of the same form as (A.15) with

$$f(R_1) = \frac{2 + (1 + 2R_1)\log\left(\frac{\varepsilon}{32}\right)}{16\varepsilon\pi \log\left(\frac{32}{\varepsilon}\right)} - \frac{1}{\pi}\log\left(\frac{\varepsilon}{8}\right) \int_0^1 W_1(R) \, \mathrm{d}R. \qquad \text{(A.24)}$$

In this case the function $f(R_1)$ is linear in $R_1$ and using Cooke's solution (A.16) yields

$$W_1 = \frac{1}{\pi R^{1/2}} \frac{\mathrm{d}}{\mathrm{d}R}\left(\int_R^1 \frac{S(x)}{(x - R)^{1/2}} \, \mathrm{d}x\right) - \frac{1}{2\pi \log 2\sqrt{R(1 - R)}} \int_0^1 \frac{f(R_1)}{\sqrt{R_1(1 - R_1)}} \, \mathrm{d}R_1. \qquad \text{(A.25)}$$

Calculating $S$ from (A.17) and substituting into (A.25) gives

$$W_1 = \frac{8\varepsilon \log\left(\frac{\varepsilon}{8}\right)\int_0^1 W_1 \, \mathrm{d}R - 1 - \log\left(\frac{\varepsilon}{32}\right) + 2\log 2 \log\left(\frac{\varepsilon}{32}\right)(1 - 2R)}{16\varepsilon\pi \log 2 \log\left(\frac{32}{\varepsilon}\right)\sqrt{R(1 - R)}}, \qquad \text{(A.26)}$$

which can be integrated with respect to $R$ from 0 to 1 to determine $\int_0^1 W_1 \, \mathrm{d}R$. Substituting this expression into (A.26) gives

$$W_1 = \frac{[2R\log 2 + 1 - \log 2]\left(\log\left(\frac{32}{\varepsilon}\right)\right)^2 - \log\left(\frac{8}{\varepsilon}\right)\log\left(\frac{32}{\varepsilon}\right) - 2\log 2}{8\pi\varepsilon \log 2 \left(\log\left(\frac{32}{\varepsilon}\right)\right)^2 \sqrt{R(1 - R)}}. \qquad \text{(A.27)}$$

So the first-order-accurate solution for $W = W_0(R) + \varepsilon W_1(R) + o(\varepsilon)$ is

$$W = \frac{-2\log 2 \log\left(\frac{32}{\varepsilon}\right) + \varepsilon\left[\left(\log\left(\frac{32}{\varepsilon}\right)\right)^2[1 - (1 - 2R)\log 2] - \log\left(\frac{8}{\varepsilon}\right)\log\left(\frac{32}{\varepsilon}\right) - 2\log 2\right]}{8\pi\varepsilon \log 2 \left(\log\left(\frac{32}{\varepsilon}\right)\right)^2 \sqrt{R(1 - R)}} + o(\varepsilon). \qquad \text{(A.28)}$$

If, however, the incorrect expression for $K_1$ that Leppington & Levine gave (A.12) is used, Leppington & Levine's solution for $W$ is

$$W = \frac{\begin{array}{c} -4 \log 2 \log \left(\frac{32}{\varepsilon}\right) [5 + 5\varepsilon(1 - 2R) \log 2] \\ + \varepsilon \left[ \left(\log \left(\frac{32}{\varepsilon}\right)\right)^2 [(1 - 2R) \log 2 + 1] + \log \left(\frac{8}{\varepsilon}\right) \log \left(\frac{32}{\varepsilon}\right) + 2 \log 2 \right] \end{array}}{16\pi\varepsilon \log 2 \left(\log \left(\frac{32}{\varepsilon}\right)\right)^2 \sqrt{R(1 - R)}}, \quad \text{(A.29)}$$

which includes an additional factor of $R$ and $\varepsilon$ on the numerator multiplying the $\log 2 \log(32/\varepsilon)$ term on the numerator.

Integrating (A.28) with respect to $R$ from 0 to 1 yields the equivalent for the total evaporative flux,

$$\int_0^1 4\pi a\varepsilon W \, \mathrm{d}R = \frac{\pi^2 a \left[(2 + \varepsilon) \log \left(\frac{32}{\varepsilon}\right) - \varepsilon\right]}{\left(\log \left(\frac{32}{\varepsilon}\right)\right)^2} + o(\varepsilon). \quad \text{(A.30)}$$

Using (A.6) to change the variables of (A.28) yields the asymptotic expressions for $J$ and $F$ in the limit $k \to 1^-$,

$$J = b\frac{4(1 - k) \log 2 - \log \left(\frac{32k}{1-k}\right) \left[(1 - k) \log \left(\frac{32k}{1-k}\right) \log 2(r - kb) + 2 - 2 \log 2\right]}{16\pi \log 2 \log \left(\frac{32k}{1-k}\right) r\sqrt{(\frac{r}{b} - k)(1 - \frac{r}{b})}} + o(1 - k), \quad \text{(A.31)}$$

$$F = \frac{b\pi^2 \left[(1 + k) \log \left(\frac{32k}{1-k}\right) - 1 + k\right]}{\left(\log \left(\frac{32k}{1-k}\right)\right)^2} + o(1 - k), \quad \text{(A.32)}$$

which gives (4.16) and (4.17) in the main text.

# Appendix B

# Derivation of the governing equation for the advection of suspended particles

In this Appendix we derive the advection-diffusion equation (6.19) appearing in the main text. We first simplify the advection-diffusion equation and the associated boundary conditions using the kinematic condition and derive the leading-order expression, in the limit of a thin droplet, for the advection for the concentration of suspended particles in the bulk of the droplet.

The concentration of suspended particles within bulk of the droplet satisfies the (scaled) advection-diffusion equation

$$
\frac{\partial \phi}{\partial t} + \nabla \cdot (-\nabla \phi + \phi \mathbf{u}) =
$$
$$
\hat{\theta}_{b0}^2 Pe \left( \frac{\partial \phi}{\partial t} + u \frac{\partial \phi}{\partial r} + w \frac{\partial \phi}{\partial z} \right) - \left( \hat{\theta}_{b0}^2 \left( \frac{\partial^2 \phi}{\partial r^2} + \frac{1}{r} \frac{\partial \phi}{\partial r} \right) + \frac{\partial^2 \phi}{\partial z^2} \right) = 0, \quad \text{(B.1)}
$$

where $\phi = \phi(r, z, t)$ is the concentration of suspended particles in bulk of the droplet. There is no flux of suspended particles through the substrate

$$\frac{\partial \phi}{\partial z} = 0 \quad \text{on} \quad z = 0, \tag{B.2}$$

and no flux of suspended particles through the free surface (see, for example, Wray et al. [83, equation 10])

$$-\nabla \phi \cdot \mathbf{n} + \phi \left( \mathbf{u} - \mathbf{u}_s \right) \cdot \mathbf{n} = 0 \quad \text{on} \quad z = h, \tag{B.3}$$

where $\mathbf{u}_s = (0, -\partial h / \partial t)$ denotes the vertical velocity of the (evolving) free surface of the droplet, $\mathbf{n}$ is the unit outward normal to the free surface of the droplet given by

$$\mathbf{n} = \frac{1}{\sqrt{1 + \frac{\partial h}{\partial r}^2}} \left( -\frac{\partial h}{\partial r}, 1 \right), \tag{B.4}$$

Utilising the kinematic condition, $(\mathbf{u} - \mathbf{u}_s) \cdot \mathbf{n}$ can be written as

$$(\mathbf{u} - \mathbf{u}_s) \cdot \mathbf{n} = -\frac{w - \frac{\partial h}{\partial t} - u \frac{\partial h}{\partial r}}{\sqrt{1 + \left( \frac{\partial h}{\partial r} \right)^2}} = J \quad \text{on} \quad z = h, \tag{B.5}$$

so the boundary condition for zero flux of suspended particles on the free surface, (B.3), can be written as

$$\frac{1}{\sqrt{1 + \theta_{b0}^2 \frac{\partial h}{\partial r}^2}} \left( -\theta_{b0}^2 \frac{\partial h}{\partial r} \frac{\partial \phi}{\partial r} + \frac{\partial \phi}{\partial z} \right) = \theta_{b0}^2 Pe \phi J \quad \text{on} \quad z = h. \tag{B.6}$$

As in the main text, we look at the case where $\theta_{b0}^2 \ll \theta_{b0}^2 Pe \ll 1$. Then in the

limit $\theta_{b0} \to 0$, we seek a solution for $\phi$ in the form

$$\phi(r,t) = \phi_0(r,t) + \theta_{b0}^2 Pe\phi_2(r,z,t) + O(\theta_{b0}^4 Pe^2). \tag{B.7}$$

Substituting (B.7) into the governing equation (B.1) gives

$$\theta_{b0}^2 Pe\left(\frac{\partial\phi_0}{\partial t} + u\frac{\partial\phi_0}{\partial r}\right) = \theta_{b0}^2\left(\frac{\partial^2\phi_0}{\partial r^2} + \frac{1}{r}\frac{\partial\phi_0}{\partial r}\right) + \frac{\partial^2\phi_0}{\partial z^2} + \theta_{b0}^2 Pe\frac{\partial^2\phi_2}{\partial z^2} + O(\theta_{b0}^4 Pe^2),$$

$$\tag{B.8}$$

and the leading and first order solution for the boundary conditions (B.2) and (B.6) become

$$\frac{\partial\phi_0}{\partial z} = 0 \quad\text{and}\quad \frac{\partial\phi_2}{\partial z} = 0 \quad\text{on}\quad z = 0, \tag{B.9}$$

and

$$-\left(\frac{\partial h}{\partial r}\frac{\partial\phi_0}{\partial r}\right) + Pe\frac{\partial\phi_2}{\partial z} = Pe\phi_0 J + O(\theta_{b0}^2 Pe^2) \quad\text{on}\quad z = h. \tag{B.10}$$

The leading order equations for $\phi_0$, (B.9) show that $\phi_0$ is independent of $z$. By considering the first-order terms in the governing equation (B.8) and the boundary conditions (B.9) and (B.10), we obtain

$$\frac{\partial^2\phi_2}{\partial z^2} = \frac{\partial\phi_0}{\partial t} + u\frac{\partial\phi_0}{\partial r}, \tag{B.11}$$

subject to the boundary conditions

$$\frac{\partial\phi_2}{\partial z} = 0 \quad\text{on}\quad z = 0 \tag{B.12}$$

and

$$\frac{\partial\phi_2}{\partial z} = \phi_0 J \quad\text{on}\quad z = h. \tag{B.13}$$

Integrating (B.11) with respect to $z$ from $z = 0$ to $z = h$ and imposing (B.12)

yields,

$$\frac{\partial \phi_2}{\partial z} = \frac{\partial \phi_0}{\partial t} + \frac{\partial \phi_0}{\partial r}\bar{u}. \tag{B.14}$$

Finally, by substituting (B.13) into (B.14) and dropping subscripts, equation (B.14) becomes

$$\frac{\partial \phi}{\partial t} + \bar{u}\frac{\partial \phi}{\partial r} = \frac{\phi J}{h}, \tag{B.15}$$

which gives (6.19) in the main text.

# Bibliography

[1] A. Li. Leaf drop. `https://www.youtube.com/watch?v=EsXp_16yI2E`. [Accessed 22-Sep-2022].

[2] A. Aboubakri, Y. Akkus, A. K Sadaghiani, K. Sefiane, and A. Koşar. Computational and experimental investigations on the evaporation of single and multiple elongated droplets. *Chemical Engineering Journal Advances*, 10:100255, 2022.

[3] M. Ait Saada, S. Chikh, and L. Tadrist. Numerical investigation of heat and mass transfer of an evaporating sessile drop on a horizontal surface. *Physics of Fluids*, 22(11):112115, 2010.

[4] Y.A Antipov. Analytic solution of mixed problems of Mathematical Physics with a change of boundary conditions over a ring. *Mechanics of Solids*, 24(3):49–56, 1989.

[5] S. Armstrong, G. McHale, R. Ledesma-Aguilar, and G. G. Wells. Pinning-free evaporation of sessile droplets of water from solid surfaces. *Langmuir*, 35(8):2989–2996, 2019.

[6] S. Armstrong, G. McHale, R. Ledesma-Aguilar, and G. G. Wells. Evaporation and electrowetting of sessile droplets on slippery liquid-like surfaces and slippery liquid-infused porous surfaces (SLIPS). *Langmuir*, 36(38):11332–11340, 2020.

[7] D. Attinger, C. Moore, A. Donaldson, A. Jafari, and H. A. Stone. Fluid dynamics topics in bloodstain pattern analysis: Comparative review and research opportunities. *Forensic Science International*, 231(1):375–396, 2013.

[8] M. R. Barmi and C. D. Meinhart. Convective flows in evaporating sessile droplets. *J, Phys. Chem. B*, 118(9):2414–2421, 2014.

[9] R. Bhardwaj, X. Fang, and D. Attinger. Pattern formation during the evaporation of a colloidal nanoliter drop: a numerical and experimental study. *New Journal of Physics*, 11(7):075020, 2009.

[10] K. S. Birdi, D. T. Vu, and A. Winter. A study of the evaporation rates of small water drops placed on a solid surface. *J. Phys. Chem.*, 93:3702–3703, 1989.

[11] K. S. Birdi and D.T. Vu. Wettability and the evaporation rates of fluids from solid surfaces. *Journal of Adhesion Science and Technology*, 7(6):485–493, 1993.

[12] F. Boulogne, F. Ingremeau, and H. A. Stone. Coffee-stain growth dynamics on dry and wet surfaces. *J. Phys.: Condens. Matter*, 29(7):074001, 2017.

[13] B. C. Carlson and J. L. Gustafson. Asymptotic expansion of the first elliptic integral. *SIAM J. Math. Anal.*, 16(5):1072–1077, 1972.

[14] O. Castro-Orgaz and W. H. Hager. Shallow Water Hydraulics. Chapter 8: The Riemann Problem. *Springer International Publishing*, pages 313–346, 2019.

[15] C.-T. Chen and T.-Y. Hung. Morphology and deposit of picoliter droplet tracks generated by inkjet printing. *J. Micromech. Microeng.*, 26(11):115005, 2016.

[16] S. W. Churchill and R. Usagi. A general expression for the correlation of rates of transfer and other phenomena. *AIChE J.*, 18:1121–1128, 1972.

[17] D. L. Clements and E. R. Love. Potential problems involving an annulus. *Math. Proc. Camb. Phil. Soc.*, 76(1):313–325, 1974.

[18] W. Collins. On the solution of some axisymmetric boundary value problems by means of integral equations: VIII, Potential problems for a circular annulus. *Proc. Edinburgh Math. Soc.*, 13(3):235–246, 1963.

[19] COMSOL Inc. COMSOL Multiphysics v. 5.6. `www.comsol.com`.

[20] J. C. Cooke. Triple integral equations. *Quart. J. Mech. Appl. Math.*, 16(2):193–203, 1963.

[21] J. C. Cooke. The solution of some integral equations and their connection with dual integral equations and series. *Glasgow Math. J.*, 11(1):9–20, 1970.

[22] H.-M. D'Ambrosio, T. Colosimo, B. R. Duffy, S. K. Wilson, L. Yang, C. D. Bain, and D. E. Walker. Evaporation of a thin droplet in a shallow well: theory and experiment. *J. Fluid Mech.*, 927:A43, 2021.

[23] S. Dash and S. V. Garimella. Droplet evaporation on heated hydrophobic and superhydrophobic surfaces. *Phys. Rev. E*, 89:042402, 2014.

[24] S. David, K. Sefiane, and L. Tadrist. Experimental investigation of the effect of thermal properties of the substrate in the wetting and evaporation of sessile drops. *Colloids Surf. A Physicochem. Eng. Asp.*, 298(1):108–114, 2007.

[25] R. D. Deegan. Pattern formation in drying drops. *Phys. Rev. E*, 61:475–485, 2000.

[26] R. D. Deegan, O. Bakajin, T. F. Dupont, G. Huber, S. R. Nagel, and T. A. Witten. Capillary flow as the cause of ring stains from dried liquid drops. *Nature*, 389:827–829, 1997.

[27] R. D. Deegan, O. Bakajin, T. F. Dupont, G. Huber, S. R. Nagel, and T. A. Witten. Contact line deposits in an evaporating drop. *Phys. Rev. E*, 62(1):756–765, 2000.

[28] G. J. Dunn, S. K. Wilson, B. R. Duffy, S. David, and K. Sefiane. A mathematical model for the evaporation of a thin sessile liquid droplet: Comparison between experiment and theory. *Colloids Surf. A Physicochem. Eng. Asp.*, 323(1–3):50–55, 2008.

[29] G. J. Dunn, S. K. Wilson, B. R. Duffy, S. David, and K. Sefiane. The strong influence of substrate conductivity on droplet evaporation. *J. Fluid Mech.*, 623:329–351, 2009.

[30] A. M. J. Edwards, E. Ruiz-Gutierrez, M. I. Newton, G. McHale, G. G. Wells, R. Ledesma-Aguilar, and C. V. Brown. Controlling the breakup of toroidal liquid films on solid surfaces. *Sci. Rep.*, 11:8120, 2021.

[31] H. Y. Erbil, G. McHale, and M. I. Newton. Drop evaporation on solid surfaces: Constant contact angle mode. *Langmuir*, 18(7):2636–2641, 2002.

[32] H. Y. Erbil, G. McHale, S. M. Rowan, and M. I. Newton. Determination of the receding contact angle of sessile drops on polymer surfaces by evaporation. *Langmuir*, 15(21):7378–7385, 1999.

[33] F. Vincentz. Rain drops on a window. `https://en.wikipedia.org/wiki/Contact_angle#/media/File:File-Water_droplet_at_DWR-coated_surface1.jpg`. [Accessed 22-Sep-2022].

[34] V. I. Fabrikant. On the potential flow through membranes. *J. Appl. Math. Phys.*, 36:616–623, 1985.

[35] F. Giorgiutti-Dauphiné and L. Pauchard. Drying drops. *The European Physical Journal E*, 41(3):32, 2018.

[36] G. M. L. Gladwell and O. P. Gupta. On the approximate solution of elastic contact problems for a circular annulus. *J. Elasticity*, 9(4):335–348, 1979.

[37] J. Gube. Coffee stains texture. `https://en.wikipedia.org/wiki/Coffee_ring_effect#/media/File:Coffee_Stains_Texture_08_(3731108469).jpg`. [Accessed 22-Sep-2022].

[38] H. Hu and R. G. Larson. Evaporation of a sessile droplet on a substrate. *J. Phys. Chem. B*, 106(6):1334–1344, 2002.

[39] B. Inaglory. Cloth, treated to be hydrophobic, shows high contact angle. `https://en.wikipedia.org/wiki/Contact_angle#/media/File:File-Water_droplet_at_DWR-coated_surface1.jpg`. [Accessed 22-Sep-2022].

[40] J. D. Jackson. Classical electrodynamics, 3rd ed. *Am. J. Phys*, 67(9):841–842, 1999.

[41] V. Jokinen, L. Sainiemi, and S. Franssila. Complex droplets on chemically modified silicon nanograss. *Adv. Mater.*, 20(18):3453–3456, 2008.

[42] D. Khilifi, W. Foudhil, K. Fahem, S. Harmand, and S. Ben Jaballah. Study of the phenomenon of the interaction between sessile drops during evaporation. *Therm. Sci.*, 23(2B):1105–1114.

[43] N. Laraqi. Scale analysis and accurate correlations for some Dirichlet problems involving annular disc. *Int. J. Therm. Sci.*, 50(10):1832–1837, 2011.

[44] R. G. Larson. Transport and deposition patterns in drying sessile droplets. *AIChE Journal*, 60(5):1538–1571, 2014.

[45] N. N. Lebedev and R. A. Silverman. Special functions and their applications. *Dover Publications*, 1972.

[46] P. Lenz, W. Fenzl, and R. Lipowsky. Wetting of ring-shaped surface domains. *Europhys. Lett.*, 53(5):618–624, 2001.

[47] F. G. Leppington and H. Levine. Some axially symmetric potential problems. *Proc. Edinburgh Math. Soc.*, 18(1):55–76, 1972.

[48] D. Lohse and X Zhang. Physicochemical hydrodynamics of droplets out of equilibrium. *Nat. Rev. Phys.*, 2(8):426–443, 2020.

[49] Maplesoft, a division of Waterloo Maple Inc.. Maple 2022. `https://www.maplesoft.com`.

[50] R. S. Markadeh, A. Arabkhalaj, H. Ghassemi, and A. Azimi. Droplet evaporation under spray-like conditions. *Int. J. Heat Mass Transf.*, 148:119049, 2020.

[51] H. Masoud, P. D. Howell, and H. A. Stone. Evaporation of multiple droplets. *J. Fluid Mech.*, 927:R4, 2021.

[52] G. McHale, S. Aqil, N. J. Shirtcliffe, M. I. Newton, and H. Y. Erbil. Analysis of droplet evaporation on a superhydrophobic surface. *Langmuir*, 21(24):11053–11060, 2005.

[53] G. McHale, N. J. Shirtcliffe, and M. I. Newton. Contact-angle hysteresis on super-hydrophobic surfaces. *Langmuir*, 20(23):10146–10149, 2004.

[54] I. S. McKinley and S. K. Wilson. The linear stability of a ridge of fluid subject to a jet of air. *Phys. Fluids*, 13(4):872–883, 2001.

[55] I. S. McKinley and S. K. Wilson. The linear stability of a drop of fluid during spin coating or subject to a jet of air. *Phys. Fluids*, 14(1):133–142, 2002.

[56] I. S. McKinley, S. K. Wilson, and B. R. Duffy. Spin coating and air-jet blowing of thin viscous drops. *Phys. Fluids*, 11(1):30–47, 1999.

[57] M. R. Moore, D. Vella, and J. M. Oliver. The nascent coffee ring: how solute diffusion counters advection. *J. Fluid Mech.*, 920:A54, 2021.

[58] M. R. Moore, D. Vella, and J. M. Oliver. The nascent coffee ring with arbitrary droplet contact set: an asymptotic analysis. *J. Fluid Mech.*, 940:A38, 2022.

[59] M. Murisic and L. Kondic. On the evaporation of sessile drops with moving contact lines. *J. Fluid Mech*, 679:219–246, 2011.

[60] B. Noble. Certain dual integral equations. *J. Math. Phy.*, 37(1–4):128–136, 1958.

[61] T. Okuzono, M. Kobayashi, and M. Doi. Final shape of a drying thin film. *Phys. Rev. E*, 80:021603, 2009.

[62] R. G. Picknett and R. Bexon. The evaporation of sessile or pendant drops in still air. *J. Colloid Interface Sci.*, 61(2):336–350, 1977.

[63] P. G. Pittoni, C.-H. Lin, T.-S. Yu, and S.-Y. Lin. On the uniqueness of the receding contact angle: Effects of substrate roughness and humidity on evaporation of water drops. *Langmuir*, 30(31):9346–9354, 2014.

[64] V. L. Popov, M. Heß, and E. Willert. Handbook of contact mechanics: Exact solutions of axisymmetric contact problems. Chapter 10: Annular contacts.

*Springer Berlin Heidelberg*, pages 295–318, 2019.

[65] Y. O. Popov. Evaporative deposition patterns: Spatial dimensions of the deposit. *Phys. Rev. E*, 71(3):036313, 2005.

[66] T. K. Pradhan and P. K. Panigrahi. Deposition pattern of interacting droplets. *Colloids Surf. A Physicochem. Eng. Asp.*, 482:562–567, 2015.

[67] A. F. Routh. Drying of thin collodial films. *Rep. Prog. Phys.*, 76,:046603, 2013.

[68] F. G. H. Schofield, A. W. Wray, D. Pritchard, and S. K. Wilson. The shielding effect extends the lifetimes of two-dimensional sessile droplets. *J. Eng. Math.*, 120:89–110, 2020.

[69] C. Schäfle, M. Brinkmann, C. Bechinger, P. Leiderer, and R. Lipowsky. Morphological wetting transitions at ring-shaped surface domains. *Langmuir*, 26(14):11878–11885, 2010.

[70] K. Sefiane. Patterns from drying drops. *Advances in Colloid and Interface Science*, 206:372–381, 2014.

[71] M. E. R. Shanahan, K. Sefiane, and J. R. Moffat. Dependence of volatile droplet lifetime on the hydrophobicity of the substrate. *Langmuir*, 27(8):4572–4577, 2011.

[72] D. P. Siregar, J. G. M. Kuerten, and C. W. M. van der Geld. Numerical simulation of the drying of inkjet-printed droplets. *Journal of Colloid and Interface Science*, 392:388–395, 2013.

[73] B. Sobac and D. Brutin. Triple-line behavior and wettability controlled by nanocoated substrates: Influence on sessile drop evaporation. *Langmuir*, 27(24):14999–15007, 2011.

[74] J. M. Stauber, S. K. Wilson, B. R. Duffy, and K. Sefiane. Evaporation of droplets on strongly hydrophobic substrates. *Langmuir*, 31(12):3653–3660, 2015.

[75] P. J. Sáenz, A. W. Wray, Z. Che, O. K. Matar, P. Valluri, J. Kim, and K. Sefiane. Dynamics and universal scaling law in geometrically-controlled sessile drop evaporation. *Nat. Commun.*, 8:14783, 2017.

[76] V. K. Vlasko-Vlasov, M. Sulwer, E. V. Shevchenko, J. Parker, and W. K. Kwok. Ring patterns generated by an expanding colloidal meniscus. *Phys. Rev. E*, 102(5):052608, 2020.

[77] H. Wijshoff. Drop dynamics in the inkjet printing process. *Curr. Opin. Colloid Interf. Sci.*, 36:20–27, 2018.

[78] E. Willert, Q. Li, and V. L. Popov. The JKR-adhesive normal contact problem of axisymmetric rigid punches with a flat annular shape or concave profiles. *Facta Univ. Mech. Eng.*, 14(3):281, 2016.

[79] S. K. Wilson and H.-M. D'Ambrosio. Evaporation of sessile droplets. *Annual Review of Fluid Mechanics*, 55(1):481–509, 2023.

[80] S. K. Wilson and B. R. Duffy. "Mathematical Models for the Evaporation of Sessile Droplets", Chapter 4 in "Drying of Complex Fluid Drops: Fundamentals and Applications" (eds D. Brutin and K. Sefiane). Soft Matter Series. *Royal Society of Chemistry*, (14):47–67, 2022.

[81] A. W. Wray, B. R. Duffy, and S. K. Wilson. Competitive evaporation of multiple sessile droplets. *J. Fluid Mech.*, 884:A45, 2020.

[82] A. W. Wray and M. R. Moore. Evaporation of non-circular droplets. *Journal of Fluid Mechanics*, 961:A11, 2023.

[83] A. W. Wray, D. T. Papageorgiou, R. V. Craster, K. Sefiane, and O. K. Matar. Electrostatic suppression of the "coffee stain effect". *Langmuir*, 30(20):5849–5858, 2014.

[84] A. W. Wray, P. S. Wray, B. R. Duffy, and S. K. Wilson. Contact-line deposits from multiple evaporating droplets. *Phys. Rev. Fluids*, 6(7):073604, 2021.

[85] X. Yang, Z. Jiang, P. Lyu, Z. Ding, and X. Man. Deposition pattern of drying droplets. *Commun. Theor. Phys.*, 73(4):047601, 2021.

[86] Y. Yu, H. Zhu, J. M. Frantz, M. E. Reding, K. C. Chan, and H.E. Ozkan. Evaporation and coverage area of pesticide droplets on hairy and waxy leaves. *Biosystems Engineering*, 104(3):324–334, 2009.